

Growth and Electronic Properties of AlAs/GaAs Lateral Superlattices : from 2D to 1D.

Dissertation

submitted by
Petra Denk
from Düsseldorf



Munich, June 9th, 2000

Prof. Dr. J. P. Kotthaus
Chair of Experimental Semiconductor Physics
Physics Department

1. Examiner: Prof. J.P. Kotthaus
 2. Examiner: Prof. W. Zwerger
- Day of the oral exam: July, 26th, 2000

Summary

Lateral AlAs/GaAs superlattices on vicinal surfaces are grown and their electronic properties are investigated by transport measurements. Numerical calculations are developed to understand the experimental measurements comprehensively. For the first time, the existence of minigaps and minibands in these kind of structures are convincingly demonstrated by temperature and charge density dependent resistivity measurements.

Organized molecular beam epitaxy on vicinal surfaces allows to create two-dimensional electron systems, which are periodically modulated on a nanometric scale in one direction. Due to the periodical lateral potential modulation, which is generated by the alternate deposition of Al and Ga atoms (under low Arsenic background pressure) on vicinal surfaces, minigaps and minibands arise in one direction of the bandstructure of the lateral modulated electron system.

The minigaps and -bands are demonstrated by temperature dependent mobility measurements. For this purpose, the anisotropy ratio of the mobility $r(T) = \mu_{\parallel}/\mu_{\perp}$ is measured for different charge densities. Depending on the charge density, they exhibit pronounced maxima at finite temperature which arise from an anomaly in the mobility perpendicular to the lateral potential modulation.

This is shown by calculating the bandstructure in a self-consistent Hartree approximation. The resulting wave functions are used to solve the semiclassical linearized Boltzmann transport equation in a relaxation time approximation, considering ionized impurity, alloy and acoustic phonon scattering. Equally, the strong anisotropy of the collision time due to the anisotropy of the band structure is taken into account. The impact of the second Fourier coefficient of the lateral potential modulation as well as the effect of including higher subbands (up to three) in the dielectric function is studied systematically for a small angle scattering (remote ionized impurity) and a large angle scattering (alloy) potential. Due to this detailed analysis, it is possible to obtain a thorough explanation of the experimental data, and especially to understand the anomaly in the perpendicular direction which arises, if the Fermi energy is close to the second miniband.

Measuring the perpendicular and parallel mobility as a function of charge density at low temperature, seems to indicate an answer to the theoretical open question, which scattering angle ($\theta_{\vec{v}_k}$ or $\theta_{\vec{k}}$) has to be taken when solving the linearized Boltzmann transport equation in a relaxation time approximation for a modulated electron system: taking the angle $\theta_{\vec{k}}$, one finds better agreement between the experimental data and the calculations than when taking $\theta_{\vec{v}_k}$.

The importance of including higher subbands in the dielectric function at higher temperature or charge density is equally demonstrated for an unmodulated 2DEG. It is pointed out that the inclusion of higher subbands is more important if the average scattering vector is small.

Zusammenfassung

Es wurden mittels Molekularstrahlepitaxie laterale AlAs/GaAs Übergitter auf verkippten Oberflächen hergestellt und im Hinblick auf ihre elektronischen Eigenschaften durch Transportmessungen untersucht. Numerische Modellrechnungen wurden entwickelt, um die experimentellen Ergebnisse zu verstehen. Erstmals ist es gelungen, die Existenz von Minibändern und Minilücken in derartigen Systemen überzeugend anhand von temperatur- und ladungsträgerdichteabhängigen Messungen nachzuweisen.

Molekularstrahlepitaxie auf verkippten Oberflächen ermöglicht die Herstellung zweidimensionaler Elektronensysteme, welche periodisch in der Grössenordnung von Nanometern in einer Richtung moduliert sind. Aufgrund der periodischen lateralen Potenzialmodulation, welche durch die alternierende Abscheidung von Al und Ga - Atomen (unter geringem Arsendruck) auf der verkippten Oberfläche erzeugt wird, entstehen in der Bandstruktur eines solchen lateral modulierten Elektronensystems Minibänder und Minilücken. Diese Minibänder und Minilücken werden mittels temperaturabhängigen Beweglichkeitsmessungen nachgewiesen. Zu diesem Zweck wird das Anisotropieverhältnis $r(T) = \mu_{\parallel}/\mu_{\perp}$ für verschiedene Ladungsträgerdichten gemessen. Abhängig von der Ladungsträgerdichte existieren mehr oder weniger ausgeprägte Maxima bei endlicher Temperatur, welche auf einen anomalen Verlauf der Beweglichkeit senkrecht zur lateralen Potenzialmodulation als Funktion der Temperatur zurückgeführt werden können.

Dieses wird durch Bandstrukturechnungen in selfkonsistenter Hartree - Poisson Näherung gezeigt. Die daraus resultierenden Wellenfunktionen werden verwendet, um die linearisierte Boltzmann - Transportgleichung in Relaxationszeitnäherung unter Berücksichtigung von Verunreinigungs-, Legierungs- und akustischer Phononenstreuung zu lösen. Ebenso wird die starke Anisotropie der Kollisionszeit aufgrund der Anisotropie der Bandstruktur berücksichtigt. Der Einfluss des zweiten Fourierkoeffizienten als auch die Rolle energetisch höherer Subbänder in der dielektrischen Funktion (bis zu drei) wird systematisch für ein Kleinwinkelstreupotential (remote ionized impurity) und ein Großwinkelstreupotential (Legierungsstreuung) untersucht. Aufgrund dieser detaillierten Analyse ist es möglich, eine in sich konsistente Erklärung der experimentellen Daten zu erhalten und insbesondere die Anomalie, die in der Beweglichkeit senkrecht zur lateralen Potenzialmodulation auftritt, wenn die Fermienergie in der Nähe der zweiten Minilücke liegt, zu verstehen.

Die Messung der senkrechten und parallelen Beweglichkeit als Funktion der Ladungsträgerdichte bei tiefen Temperaturen gibt offenbar einen Hinweis zur Beantwortung der theoretisch offenen Frage, welcher Streuwinkel ($\theta_{\vec{v}_k}$ oder $\theta_{\vec{k}}$) verwendet werden sollte, wenn die linearisierte Boltzmann - Transportgleichung in Relaxationszeitnäherung für ein moduliertes zweidimensionales Elektronengas gelöst wird: verwendet man $\theta_{\vec{k}}$, so erhält man bessere Übereinstimmung zwischen den experimentellen Daten und Rechnungen gegenüber der Verwendung von $\theta_{\vec{v}_k}$.

Die Bedeutung der Berücksichtigung höherer Subbänder in der dielektrischen Funktion bei höheren Temperaturen oder Ladungsträgerdichten wird ebenfalls für ein nicht moduliertes Elektronengas gezeigt.

Contents

1	Introduction	7
2	Physical Fundamentals of Heterostructures	11
2.1	1D Modulated Heterostructures	11
2.1.1	Electronic Properties	16
2.1.2	1D Calculations	17
2.2	2D Modulated Heterostructures	19
2.2.1	General Effects of the Lateral Potential	19
2.2.2	Amplitude and Form of the Lateral Potential	21
2.2.3	Electronic Properties	27
3	The Boltzmann Transport Equation	35
3.1	Scattering Probability	37
3.2	Solution of the Boltzmann Equation	37
3.3	Relaxation Time τ	38
3.3.1	Relaxation Time τ for an Unmodulated 2DEG	38
3.3.2	Relaxation Time τ for a Modulated 2DEG	40
3.4	Calculation of the Macroscopic Quantities	42
3.5	Scattering Processes	43
3.6	Screening of an Electron Gas: Dielectric Constant $\epsilon(\vec{q})$	44
3.7	Types of Interactions	47
4	Technological Processing of a Lateral Superlattice	55
4.1	Doped Lateral Superlattices	58
4.2	Growth Conditions	60
4.3	Sample Fabrication	64
4.3.1	Experimental Detection of the zone $p = 1$	64
4.3.2	Sample Processing	65

5	Numerical Results	69
5.1	Screening	69
5.1.1	Multisubband Polarizability Matrix	71
5.1.2	Formfactor	76
5.2	Effective Interaction Potentials for Unmodulated 2DEG's	79
5.3	Effective Interaction Potentials for Modulated 2DEG's	87
5.4	Mobility as a Function of Fermi Energy	89
5.4.1	Small Angle Scattering Potential	90
5.4.2	Large Angle Scattering Potential	93
5.4.3	Scattering Angle $\theta_{\vec{q}_k}$ "against" $\theta_{\vec{k}}$	96
5.4.4	Impact of the Second Fourier Coefficient	99
5.5	Influence of the Temperature	103
5.5.1	Vanishing of the Bandstructure Effects	105
5.5.2	Mobility as a Function of Temperature	108
6	Experimental results	119
6.1	Unmodulated 2DEG: Effect of Enhanced Screening	121
6.2	Modulated 2DEG: Evidence of Minigaps	124
6.2.1	Parallel and Perpendicular Mobility as a Function of Temperature	128
6.2.2	Impact of the Second Fourier Coefficient	135
6.2.3	Effect of the Tilt of the Lateral Potential Modulation .	137
6.2.4	Which Scattering Angle: $\theta_{\vec{q}_k}$ against $\theta_{\vec{k}}$?	140
7	Conclusion	143
	Bibliography	147

Chapter 1

Introduction

A great success in physics in the last century was the explanation of electronic properties in atoms by quantum mechanics. The same principles were then applied to describe electronic effects in solids. This represents the starting point of modern solid state physics. An important difference between experiments with atoms and solids is the possibility in solids to tailor almost any artificial potential by combining metals, semiconductors, and insulators or by the application of external fields. Due to this, solid state physics offer an ideal playground for the investigation of quantum mechanic effects.

In order to explore quantum mechanic in its full range, one major goal until today is the reduction of the system's dimensionality. After the realization of a two dimensional electron gas (2DEG), also 1D and 0D systems could be demonstrated, i.e. quantum wires and quantum dots. Furthermore, systems of intermediate dimensionality are feasible (systems between 1D and 2D). The fabrication and exploration of such a system is the goal of this work. Specially, a 2DEG shall be modulated by a 1D periodic potential in the lateral plan, which can be described in the physical picture of an array of parallel quantum wires coupled by the tunneling effect. The consequence of this coupling are minigaps and minibands in the band structure, which result in special features of the conductivity in the longitudinal and transverse direction. Although many attempts have already been made to demonstrate these effects, clear evidence has not yet been achieved. The objective of this work is to prove the existence of minigaps in transport measurements.

In the following the attempt is made to convey to the reader the background of the subject so that the interest and significance of the subject can be understood.

The experimental investigation of the physics of low dimensional electron

systems, e.g. systems in which the motion is at least quantized in one direction, dates back to the 60's, when Metal - Oxide structures [Fowler 66] of Silicon were studied. At the same time, considerable progress in the growth technics like in MBE or MOCVD could have been achieved, allowing to realize heterostructures of the semiconductors III-V of high purity. Concerning the transport properties of low dimensional systems, the invention of modulation doped heterostructures [Dingle 78] was a mile stone: The idea of separating the electrons from their donors allows to produce two dimensional electron systems of high mobility. Due to these technological progresses, many new physical effects could have been observed. For example, the fractional quantum Hall effect [Tsui 82] or the Wigner cristallization of the electrons [Andrei 88] in doped structures, the confined Stark effect [Miller 85] or the Wannier - Stark effect [Voisin 88] in undoped structures could be demonstrated. These effects are equally interesting from a technological point of view and are already used commercially in micro and optoelectronic dispositifs like quantum well laser [Tsang 82] or Wannier Stark commutators [Bar - Joseph 89]. A direct consequence of the invention of the modulation doping is the fabrication of new field effect transistors (HEMT) [Delagebeaudeuf 80], which are today widely used in cellular phones.

Exploring such rich physics of 2D systems, it seems natural to reduce further the dimensionality of the system, e.g. trying to fabricate quantum wires (1D), quantum boxes (0D) or lateral superlattices (modulated 2D). Additionally, new effects which cannot be realized in multilayered superlattices of Esaki and Tsu [Esaki 70] are expected. For example, it has been predicted that carrier scattering probability by ionized impurities [Sakaki 80] and by polar optical phonons [Sakaki 89] can be suppressed in quantum wires. In a theoretical paper Sakaki [Sakaki 76] proposed 1976 a system of lateral quantum wires in order to obtain a differential negative resistance.

But how can one achieve such structures of reduced dimension? Experimentally, many of the methods, applied to obtain a lateral structuring, associate electronic lithography to an edge [Perez 90] or metallization process [Winkler 89] [Gerhardts 89]. Weiss et al. had the original idea to exploit the persistent photoconductivity in modulation doped heterostructures effect at low temperature in order to modulate laterally [Weiss 89]. In these systems, new oscillations in the conductivity (Weiss Oscillations) as a function of magnetic field have been detected. However, these lithographically techniques do not allow to obtain good electronic properties, if one tries to reduce the lateral dimensions beneath 100 nm.

Other approaches are essentially based on growth techniques [Petroff 84]

[Kapon 89][Pfeiffer 90]. One method to introduce a lateral structure is to use periodic atomic steps on vicinal substrates. The idee dates back in the 70's, when the first trial was made in a Si metal - oxide - semiconductor (MOS) inversion layer on the misoriented surface; however, although the existence of minigaps was demonstrated [Cole 77], it was found that the minigaps do not originate from lateral superlattice effects [Sham 78]. Petroff et al. [Petroff 84] proposed an alternative approach, in which the selective growth of GaAs and AlAs is achieved by the alternate deposition of submonolayer GaAs and AlAs on misoriented substrates tilted slightly by an angle α ($0.5^\circ - 2^\circ$). The period of such a lateral superlattice is determined by the average terrace width L_\perp and is given by $a \cdot \cot\alpha$, where a is the thickness of one monolayer ($a=0.283$ nm in GaAs). The lateral organization has first been demonstrated by transmission - electron microscopy [Gaines 88]. Recently, also convincing evidence of the minigaps has been reported by photoluminescence and photoluminescence - excitation measurements [Mélin 98]. However, the observation of minigaps in transport measurements has not been demonstrated yet.

In transport measurements, Sakaki et al. [Motohisa 89] were the first who measured an anisotropy of the mobilities in the parallel and perpendicular direction of a lateral structure grown on GaAs vicinal surfaces. The lateral structure was produced by the insertion of half an Aluminum monolayer in the channel region of a heterojunction grown on a vicinal surface. A plausible approach of interpretation was that the anisotropy is a sign of nonparabolicity in the miniband structure of a periodic lateral potential. However, a single anisotropy in the mobilities does not demonstrate the existence of a lateral organization, e.g. the formation of a periodic modulation. The anisotropy of the mobility can equally arise from the formation of anisotropic islands. For instance, J. Bloch demonstrated that the anisotropy in optical properties of lateral structures due to the fractional deposition of one monolayer is not due to the lateral periodic organization along the steps but to the formation of anisotropic islands [Bloch 94]. The optical properties were independent of the lateral period given by the terrace length of the vicinal surfaces. In contrast, in lateral super - lattices, which consist of at least 10 monolayers, the optical properties depend strongly on the terrace length, indicating the influence of the lateral potential modulation [Bloch 94].

In this work, with the aim of demonstrating the existence of minigaps in transport measurements, doped lateral superlattices AlAs/GaAs on GaAs vicinal surfaces, 0.5° misoriented with respect to the direction [001] are grown and their transport properties are studied. Calculations have been developed which predict effects which are due to the lateral potential. Due to the

comprehensive approach of combining detailed calculations with experiment, the evidence of minigaps can be demonstrated in transport measurements.

The introductory chapter presents the fundamental physics of lateral modulated 2D systems and explains the bandstructure calculations (chapter 2). The transport formalism (chapter 3) is essential to understand the numerical (chapter 5) and the experimental (chapter 6) results. The method of fabricating lateral superlattices is presented in chapter 4.

Chapter 2

Physical Fundamentals of Heterostructures

"Nanotechnology - the last industrial revolution" is the title of a book [Schulenburg 95], recently published. It shall not be discussed here, whether the nanotechnology is in fact a revolution. But for sure is that the progress achieved in the technology due to Molecular Beam Epitaxy allowed the advancing in a revolutionary manner. Using the Molecular Beam Epitaxy (MBE), one is nowadays able to create almost every potential one desires with the precision of one monolayer. This is often described by the expression "band gap engineering" [Capasso 87]. In this work different potentials, e.g. heterojunctions with lateral potential modulations are fabricated and measured. This is the reason why in the first part of this chapter the principle of the band gap engineering is explained. In the second part, one and two dimensional self - consistent Hartree - Schrödinger calculations are presented. They have been developed in the group and modified during this thesis.

2.1 1D Modulated Heterostructures

Growing a crystal and changing abruptly the composition of the material or the material of the semiconductor itself, causes a discontinuity in the band-structure of this crystal arises, leads to a so called heterostructure. The heterostructures are fabricated by molecular beam epitaxy (MBE) in this work. They are composed of the materials $\text{Al}_x\text{Ga}_{1-x}\text{As}/\text{GaAs}$ (where x describes the Aluminum fraction in the ternary alloy $\text{Al}_x\text{Ga}_{1-x}\text{As}$).

In order to obtain high quality heterostructures, two factors are fundamental: the material choice and the doping technique, as will be explained

in the following.

The combination of the materials $\text{Al}_x\text{Ga}_{1-x}\text{As}/\text{GaAs}$ is widely used, because Aluminiumarsenid (AlAs) and Galliumarsenid (GaAs) have almost perfect lattice match in any range of the Al concentration. Thus, during growth the Al-concentration can be changed without disturbing the crystal lattice. On the contrary, the band structure strongly depends on the Aluminum concentration: in GaAs the band gap is direct ($\Gamma \rightarrow \Gamma$, $E_g(T)_{T=4K} = 1.5192$ eV), whereas in AlAs the band gap is indirect ($\Gamma \rightarrow X$, $E_g = 2.4$ eV), for an alloy $\text{Al}_x\text{Ga}_{1-x}\text{As}$, the band gap depends on the average Al -concentration x . For $x < 0.35$, the band gap remains direct and increases linearly with x :

$$E_g = (1.5192 + 1.42 * x) \text{ eV} \quad (2.1)$$

Similarly, the effective mass of the electron is a function of the Al- concentration:

$$m^* = (0.067 + 0.084 * x) m_e \quad (2.2)$$

where m_e is the free electron mass.

The key feature of a heterostructure is the bandstructure discontinuity formed at the interface due to the different energy gaps of the used materials. With respect to the valence and conduction edge of an $\text{Al}_x\text{Ga}_{1-x}\text{As}/\text{GaAs}$ structure, the material $\text{Al}_x\text{Ga}_{1-x}\text{As}$ (high band gap material) acts for both the valence and conductance charge carriers as a barrier: they are confined in the narrow gap material (e.g. GaAs). The band offset discontinuity between the materials $\text{Al}_x\text{Ga}_{1-x}\text{As}$ and GaAs is distributed to 67 % to the conduction and to 33 % to the valence band [Danan 87]. This results - in a first order approximation - in a potential modulation of approximately 10 meV per Al - percent in the conduction band.

In order to obtain high charge densities, doping of the structure is necessary. The most appropriate technique is modulation doping [Wood 80, Ploog 87].¹ The mechanism which will take place due to the doping is shown in Fig. 2.1: a heterostructure (e.g. $\text{Al}_x\text{Ga}_{1-x}\text{As}/\text{GaAs}$) is grown and the high band gap material is doped. Until thermodynamical equilibrium is reached,

¹The doping type is determined by the way one introduces the dopant: it is called either volumic doping, if one incorporates the dopant *during* the growth of the high band gap material, or δ - doping, if one *interrupts* the growth process (As - flux continued), resulting in the deposition of the dopant into ideally one single monolayer. It is the latter type of doping with the n - dopant Si, which is used for all structures fabricated in this work. Additionally, one can introduce a second δ - doping plane closer to the surface. It saturates the surface states and one can then assume that all electrons, steeming from the doneurs, located in the δ - plane close to the channel, will transfer in the channel.

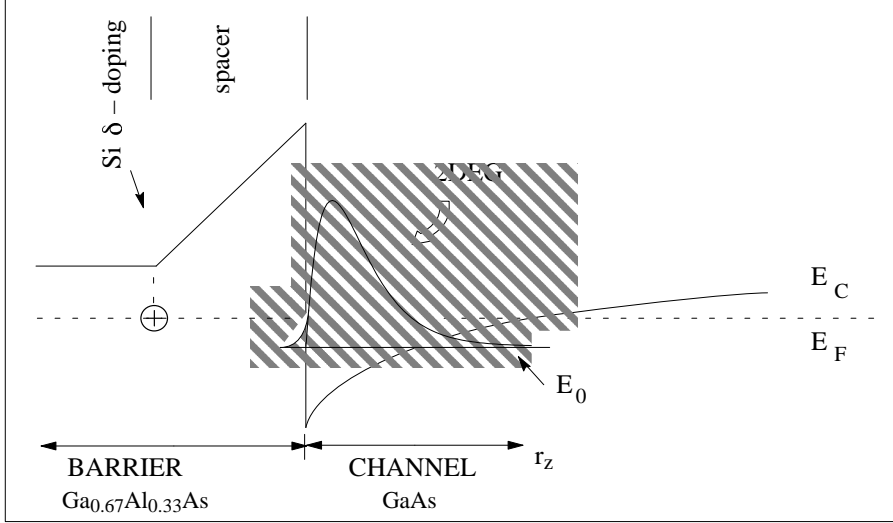


Figure 2.1: *Conduction band of a heterostructure as a function of the growth direction r_z . Due to the doping, band bending at the interface takes place, which leads to a triangular confinement potential for electrons.*

the electrons associated with the donors will transfer to the lower lying energy states in the narrow bandgap material, also called channel. The spatial separation of the positive-ly charged donors and negatively charged electrons has two effects: It firstly produces an additional electric field² ($\text{Si}^+ \rightarrow e^-$) governed by the Poisson equation (discussed in more detail in section 2.1.1), which creates the confining potential for electrons in the channel, as shown in Fig. 2.1. Secondly, due to the physical separation of ionized scattering centers and electrons, the mobility of the electrons is increased. This effect is in general intended to be enhanced: one places the dopants some distance away from the heterointerface by including an intermediate undoped "spacer" region.

Due to the strong band bending, which takes place on a small scale (~ 5 nm), the transferred electrons are confined in a quasi triangular potential near the interface. This confinement is defined by the conduction band discontinuity on one side and by the r_z - dependent electrostatic potential on the other side (see also Fig. 2.1). As the potential extension is of the same order as the de Broglie wavelength of an electron, bound states are formed for the r_z - motion. If the energy spacing $E_\alpha - E_{\alpha'}$ between levels α (typically 25 meV in samples used here) is much larger than the thermal broadening of the elec-

²In samples used here, it is typically 100kV/cm.

tron distribution function, a quasi - twodimensional electron gas (Q2DEG) is formed: confined in the growth direction (e.g. r_z -direction) and free in the interface plane (e.g. in the $r_{||}$ - r_{\perp} plane). The term "quasi-twodimensional" refers to the fact that the electron gas has a finite spatial extension in the r_z - direction, i.e. the wavefunctions $\xi_{\alpha}(r_z)$ are not $\delta(r_z)$ functions. The envelope wavefunction [Bastard 88] of an electron is thus given in the effective mass approximation by (A corresponds to the surface area of the sample)

$$\Psi_{\alpha}(r_{||}, r_{\perp}, r_z) = \frac{1}{\sqrt{A}} \xi_{\alpha}(r_z) e^{i(k_{||}r_{||} + k_{\perp}r_{\perp})}. \quad (2.3)$$

with total energy

$$E_{\alpha}(k_{||}, k_{\perp}) = E_{\alpha} + \frac{\hbar^2}{2m^*}(k_{||}^2 + k_{\perp}^2). \quad (2.4)$$

E_{α} is the eigenvalue associated to the subband wavefunction $\xi_{\alpha}(r_z)$ which is obtained by solving the one - dimensional Schrödinger equation. It corresponds to the energy of the quantum level α which depends on the confinement potential. The second term describes the free energy dispersion parallel to the heterostructure. The term subband refers to an energy level E_{α} in the r_z - direction with a continuous energy spectrum in the $r_{||}$, r_{\perp} plan. In Fig. 2.2 subbands in the \vec{k} - space are shown: To each subband corresponds a two - dimensional energy - parabola. As a two - dimensional system (and neglecting non parabolic effects (see below), the density of states is constant in each subband :

$$D(E) = g_s g_v \frac{m^*}{\pi \hbar^2} \quad (2.5)$$

Since in GaAs there is no valley degeneracy (valley degeneracy factor $g_v=1$) the spin degeneracy factor g_s equals 2.

The effective mass m^* of electrons at the minimum of the GaAs conduction band is 0.0672. Using the $\vec{k}\vec{p}$ approximation, the energy dispersion $E(\vec{k})$ for an electron in the vicinity of the Brillouin zone can be written as (an anisotropy of the band - structure and the spin splitting is negligible) [Bastard 88]:

$$E(\vec{k}) = E_0 + \frac{\hbar^2 \vec{k}^2}{2m^*} - \gamma \left(\frac{\hbar^2 \vec{k}^2}{2m^*} \right)^2 \quad (2.6)$$

with γ being the non - parabolicity coefficient. We can also neglect non - parabolic effects (e.g $\gamma = 0$), because they proved to be very small. In Fig. 2.3 the Fermi energy E_F^0 , which corresponds to the energetical highest occupied state at $T = 0$ K, is shown as a function of charge density for an

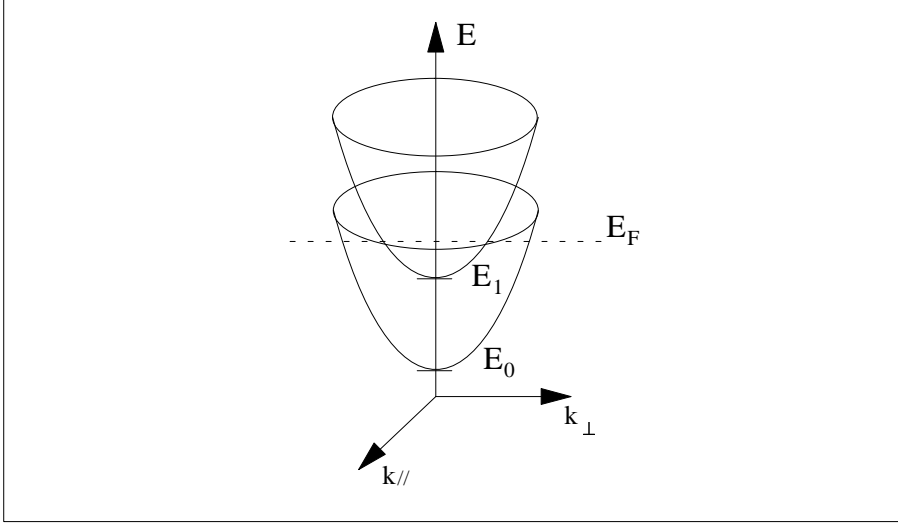


Figure 2.2: *Energie dispersion of a 2DEG in the first two subbands: The energy is quantized in the r_z - direction and free in the $r_{||}$, r_{\perp} direction.*

$\text{Al}_{0.33}\text{Ga}_{0.67}\text{As}/\text{Al}_{0.05}\text{GaAs}$ heterostructure. Taking the bandstructure parabolic, the slope represents the constant density of states $D(E) = m^*/\pi\hbar^2$ of the first subband. Non - parabolic effects of the bandstructure results in deviations from the slope of less than 2%, corresponding to a $\Delta E_F^0 \sim 0.3$ meV. This is negligible in comparison to the distance between the first two subbands, which is typically between 25 and 30 meV in the investigated structures. The range of the achievable electron density N_s in a heterojunction AlAs/GaAs depends on the quality of the sample (e.g. residual impurities) and of the width of the spacer. N_s varies typically between some 10^{10} and 10^{12} cm^{-2} . If there is only one subband filled³, the Fermi energy is given by

$$E_F^0 = \frac{\pi\hbar^2}{m^*} N_s \quad (2.7)$$

$$\sim 3.56 \frac{\text{meV}}{10^{11} \text{ cm}^{-2}} \cdot N_s. \quad (2.8)$$

Fig. 2.1 gives only a qualitative idea of the electrostatical potential of a heterostructure. How it can exactly be calculated, will be explained in the next section.

³This situation called electrical quantum limit is at low temperature the most often case in $\text{AlGaAs}/\text{GaAs}$ - heterostructures: it corresponds to electron densities up to $N_s = 7 - 8 \cdot 10^{11} \text{ cm}^{-2}$.

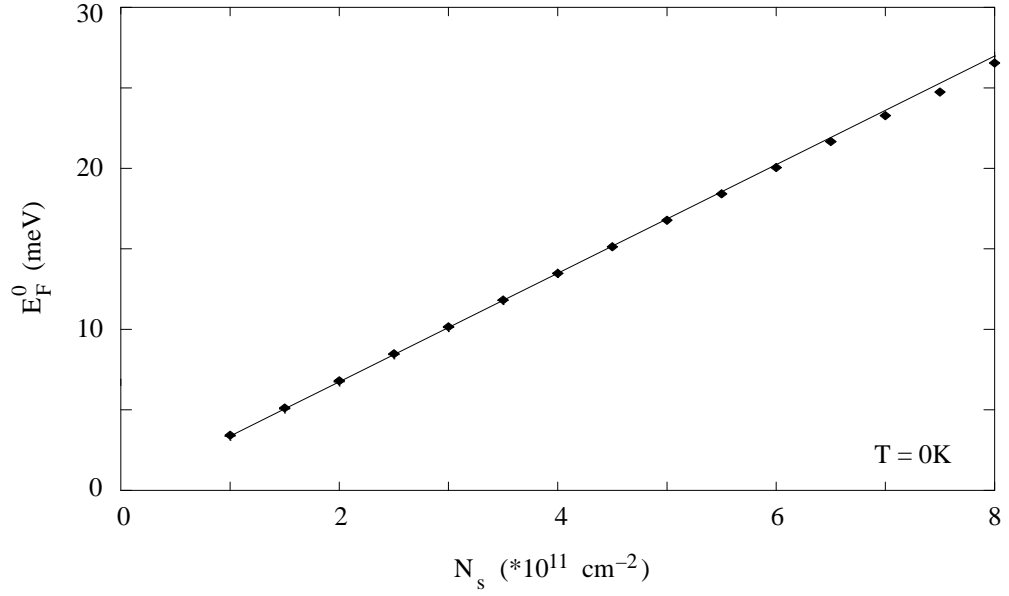


Figure 2.3: *Calculated Fermi energy E_F^0 as a function of charge density for an $\text{Al}_{0.33}\text{Ga}_{0.67}\text{As}/\text{Al}_{0.05}\text{GaAs}$ structure, obtained by a 1D Hartree - Schrödinger calculation (section 2.1.2): Deviation from the constant density of state (parabolic case, straight line) due to non - parabolic effects of the band - structure (straight line with points) are shown to be small. The points represent the charge densities for which the relation is calculated. Only the first subband is occupied.*

2.1.1 Electronic Properties

The qualitative and quantitative understanding of the mechanism of charge transfer and its amount is of importance for two reasons: It provides insight in the electronic structure of the system (e.g. heterostructure) and consequently allows the optimization of the structure for any desired behavior. Given the exact structure, one can calculate the electron distribution straight forward. Hence one has access to the electron wave functions which are required to determine transport properties.

The charge transfer depends on the confining potential and the confining potential depends on the electron distribution again. This condition of self consistency makes the problem a bit more complicated. In the following the 1D - calculations (e.g. the Hamiltonian depends only on one direction) to determine the electrostatic potential in the Hartree approximation are described in detail. They are a prerequisite to understand the later detailed

bandstructure calculations for a modulated 2DEG. Since in this work one is only dealing with doped structures, the electronic properties of the structure will be dominated by the electrons in the conduction band. One thus can neglect the existence of valence bands in the calculations.

2.1.2 1D Calculations

Electrons are described in the simplest form by the one - particle Schrödinger equation

$$H(r_z)|\xi_\alpha(r_z)\rangle = E_\alpha|\xi_\alpha(r_z)\rangle \quad (2.9)$$

The Hamiltonian $H(r_z)$ is given by

$$H(r_z) = \frac{p_{r_z}^2}{2m^*} + V_{cryst.}(r_z) + V_{electrost.}(r_z) \quad (2.10)$$

with

- $V_{cryst.}(r_z)$ representing the conduction band discontinuity at the interface (see previous section). In our structures the barrier acting material is AlGaAs, with a typical Aluminum content of 33%. The channel acting material is equally AlGaAs, but with an average of only 5% Aluminum.
- the effective mass m^* being considered as the mass of the alloy $\text{Al}_x\text{Ga}_{1-x}\text{As}$ at the minimum of the conduction band. Since in the structures, which are studied here, the average Aluminum content in the channel is equal to 5%, $m^* = 0.071 m_e$ (see also equation 2.2).
- $V_{electrost.}(r_z)$ is an averaged electrostatic potential (Hartree potential): it describes the potential which an electron at point r_z "feels" due to both the other electrons and the fixed charges.

Equation 2.9 is coupled with the Poisson equation

$$\nabla^2 V_{electrost.}(r_z) = \frac{4\pi e}{\epsilon_0 \epsilon_r} \left[\sum_{\alpha} N_{\alpha} |\xi_{\alpha}(r_z)|^2 - N_D^+(r_z) + N_A^-(r_z) \right] \quad (2.11)$$

where $N_D^+(r_z)$ corresponds to the donor concentration and $N_A^-(r_z)$ represents the concentration of ionized acceptors due to residual doping in the channel. This small acceptor concentration (in our structures: $N_A \sim 5 \cdot 10^{13} - 5 \cdot 10^{14} \text{ cm}^{-3}$) stems from carbon atoms (of the MBE - Chamber), which

substitute As-atoms in the structures. ϵ_0 refers to the dielectric permittivity in vacuum, ϵ_r to the relative permittivity (for GaAs = 13.1). n_α is the areal concentration of the α -th subband. It is related to the chemical potential E_F^4 and the temperature T by

$$N_\alpha(E_F, T) = m^* \frac{k_B T}{\pi \hbar^2} \ln[1 + e^{\frac{E_F - E_\alpha}{k_B T}}]. \quad (2.12)$$

(The effective mass m^* is assumed to be constant for each subband.)

The boundary conditions necessary for the solution of these two coupled equations are given by the requirement of electrical and thermodynamic equilibrium of the heterostructure.

Electrical equilibrium means charge neutrality

$$\sum_{\alpha} N_{\alpha}(E_F, T) + \int_{-\infty}^{\infty} dr_z [N_A^-(r_z) - N_D^+(r_z)] = 0 \quad (2.13)$$

and thermodynamic equilibrium implies

$$\frac{dE_F}{dr_z} = 0. \quad -\infty < r_z < \infty \quad (2.14)$$

From these equations follows that the Fermi energy E_F^0 ($T = 0K$) coincides in the neutral zone of the doped layer of the structure with the energy level of the donors, near the substrate with the energy level of the acceptors. By raising the temperature, the concentration of ionized donors changes and the chemical potential E_F does no longer coincide with the energy level of the donors. It will now be determined by the requirement of local charge neutrality in the plane of the donors as well as far away from the channel on the substrate side.

The Schrödinger equation is solved by the transfer matrix method: The potential is split into different sections of constant potential, where the Schrödinger equation is solved. The boundary conditions of each potential section are given by requiring the continuity of the wavefunctions and the partial current, e.g. the first derivative, divided by the effective mass. So, once having calculated the Poisson equation 2.11 with a guess of the electron distribution, one can solve the Schrödinger equation with the potential $V_{electrost.}(r_z)$ obtained from the Poisson equation. As a result, one now obtains the electron distribution, which again will be partially (to facilitate the convergence [Ando 82]) introduced in the Poisson equation. This iterative calculation will

⁴ E_F refers to the chemical potential, whereas E_F^0 refers to the Fermi energy.

proceed until there is no more significant change of the electrostatic potential (e.g. Hartree term).

These calculations, executed at a given temperature, give thus access to the eigenstates $\xi_\alpha(r_z)$ and the eigenvalues (= eigenenergies) E_α of a heterostructure as well as it determines the chemical potential E_F and charge density N_α of each subband E_α .

2.2 2D Modulated Heterostructures

In this thesis a one - dimensional periodic potential with the periodicity L_\perp is inserted in a heterostructure. The periodicity L_\perp is hereby much greater than the periodicity a which is due to the crystal structure of the material, e.g. a represents in our case the GaAs unit cell. Due to this one dimensional lateral potential modulation, the bandstructure of a free two - dimensional electron gas is modified. The way the bandstructure is modified and how this can be calculated, is discussed in this section.

2.2.1 General Effects of the Lateral Potential

In the case of **no** lateral potential modulation, the solution to the Schrödinger equation

$$H(r_\perp)|\phi\rangle = E|\phi\rangle$$

are plane waves with eigenvalues $E = \frac{\hbar^2 k_\perp^2}{2m^*}$ with $-\infty < k_\perp < \infty$.

Assuming the lateral potential modulation $V_{mod}(r_\perp)$ of periodicity L_\perp ⁵, the Fourier series of $V_{mod}(r_\perp)$ will only contain plane waves with the periodicity L_\perp and therefore with wavevectors that are vectors of the reciprocal lattice $2\pi/L_\perp$:

$$V_{mod}(r_\perp) = 2 \sum_{\vec{G}=p*2\pi/L_\perp} V_{mod}^{(G)} \cos(\vec{G}r_\perp) = 2 \sum_p V_{mod}^{(p)} \cos\left(\frac{p*2\pi r_\perp}{L_\perp}\right) \quad (2.15)$$

where $V_{mod}^{(p)}$ is the p - th Fourier component of the Fourier series. A way to determine each Fourier component is discussed in the next section.

Due to this property, the perturbation will only couple states k_\perp and k'_\perp with $\Delta k_\perp = k'_\perp - k_\perp = \pm \frac{2\pi p}{L_\perp}$, $p \in \mathbb{N}$, e.g. states which differ by a p -th multiple

⁵The periodicity corresponds in the case of lateral superlattices to the terrace length L_\perp .

reciprocal lattice vector will be coupled by the p -th Fourier component of the lateral potential modulation:

$$\langle k_{\perp} | V_{mod}^{(p)} \cos(\frac{p * 2\pi r_{\perp}}{L_{\perp}}) | k'_{\perp} \rangle = \frac{V_{mod}^{(p)}}{2} \delta(k'_{\perp} = k_{\perp} \pm \frac{p2\pi}{L_{\perp}})$$

Additionally, due to the periodic potential, the introduction of the concept of the Brillouin zone in the r_{\perp} - direction becomes meaningful. Instead of having plane waves (as in the unperturbed case) one now has functions of the form

$$\phi_{k_{\perp}}(r_{\perp}) = \sum_p a_{(k_{\perp} + p \frac{2\pi}{L_{\perp}})} e^{i(\frac{p2\pi}{L_{\perp}}) * r_{\perp}} * e^{ik_{\perp} r_{\perp}} \quad (2.16)$$

with k_{\perp} restricted to $[-\frac{\pi}{L_{\perp}}, \frac{\pi}{L_{\perp}}]$. The wave functions are expanded on plane waves but with an amplitude, which has the same periodicity as the lateral potential modulation (Bloch part).

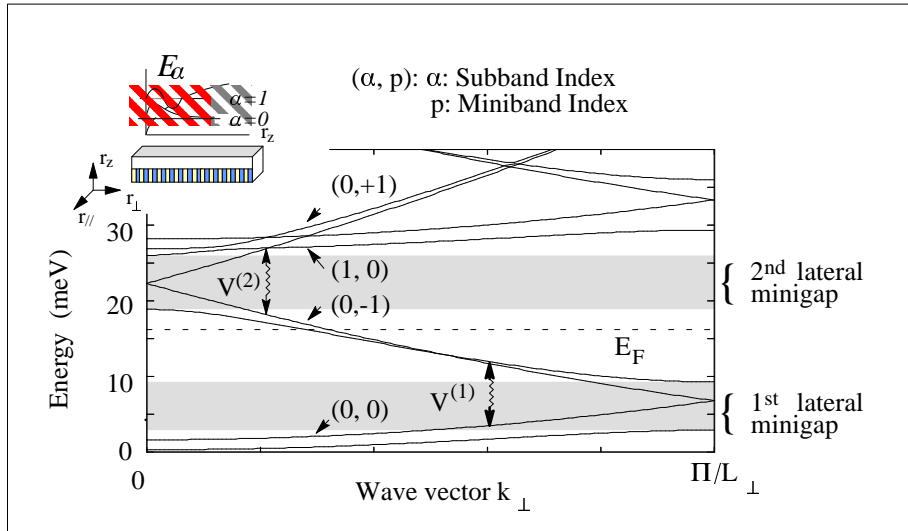


Figure 2.4: *Energy vs k_{\perp} in reduced BZ: due to the lateral potential modulation minibands and minigaps emerge in the bandstructure at $k_{\perp} = 0$ and $k_{\perp} = \pi/L_{\perp}$. In thin lines the bandstructure of an unmodulated 2DEG is shown as reference.*

In Fig. 2.4 a typical band structure calculation for a modulated two - dimensional electron gas is shown in reduced Brillouin zone schema. Due to the coupling of states differing by $\Delta k_{\perp} = \pm p * 2\pi / L_{\perp}$ minigaps at the Brillouin zone edge and at the center of the Brillouin zone arise. They are in

first order proportional to one single Fourier coefficient $V^{(p)}$ of the effective modulation (atomic potential and electron screening). Each miniband in Fig. 2.4 is labeled by two indices: The first one refers to the subband index (one still has the quantization in r_z - direction!), the second index refers to the plane wave index, corresponding to the eigenstate in the unmodulated system, e.g. to the number of the B.Z. in extended zone schema. Equally shown as a reference is the band structure of an unmodulated electron gas (thin lines).

One now has an idea how the bandstructure of a modulated 2DEG (e.g. free motion in one direction and modulated in the other one) looks like. But of course the exact band structure depends on the lateral potential modulation one inserts in the calculations. In the next section a model which describes the lateral potential modulation, produced by the growth of a lateral superlattice on a vicinal surface, will be presented. This model was developed by F. Lelarge [Lelarge 97] and is close to the growth model proposed by A. Lorke [Krishnamurthy 94]. It allows to explain the origin of the amplitude of the lateral modulation, which is measured experimentally and which is approximately reduced by a factor 10 with respect to an ideal lateral modulation.

2.2.2 Amplitude and Form of the Lateral Potential

It shall first briefly be described by which means the lateral potential modulation in this work is generated (Fig. 2.5, a more complete description is found in chapter 4): vicinal surfaces are used as templates (Fig. 2.5 a)), on which alternatively Al and Ga atoms are deposited in a monolayer by monolayer growth. Each of them incorporates itself preferably at the step sides, so that a regular sequence of the materials AlAs/GaAs results. In an ideal picture, one obtains stripes of pure AlAs and stripes of pure GaAs (Fig. 2.6.a, left). Due to the different conduction band offsets of AlAs and GaAs, these stripes introduce a lateral potential modulation of amplitude of 190 meV (taking an average of Aluminum concentration $x_{Al} = 5\%$, Fig. 2.6.a, right). In this idealized picture, the AlAs barriers have a width of $L_{\perp} \cdot x_{Al}$ and the lateral GaAs "quantum wells" a width of $(1 - L_{\perp}) \cdot x_{Al}$. This ideal periodic lateral potential can be equally described by its Fourier development:

$$V_{mod}(r_{\perp}) = \Delta E_c x_{Al} (1 + 2 \sum_{p \neq 0} V_{mod}^{(p)} * \cos(\frac{p * 2\pi r_{\perp}}{L_{\perp}})), \quad (2.17)$$

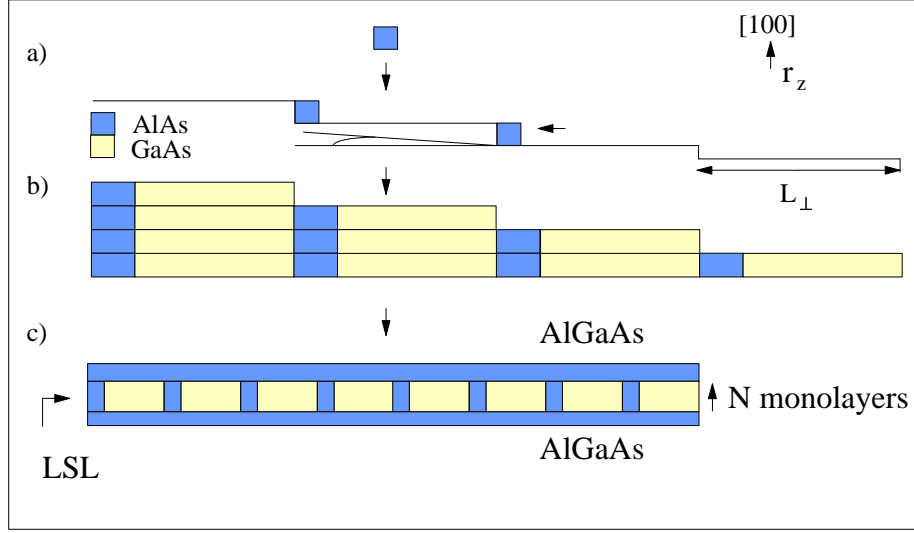


Figure 2.5: *Schema of the fabrication of the lateral potential modulation used in this work: a) Al and Ga - atoms are alternatively deposited on a vicinal surface. b) Due to their preferred incorporation at the step edges and the monolayer by monolayer growth, a lateral superlattice of N - monolayers is grown (c).*

($\Delta E_c \sim 0.95$ eV is the AlAs/GaAs conduction band offset) In reality, however, there are two major effects which reduce the lateral potential modulation: the **segregation effect** [Etienne 95] and the **effect of step disorder** [Lelarge 97] of the GaAs step arrays. These two effects shall be discussed in the following. The **segregation effect** is due to the vertical atomic exchange of Al-atoms pinging on the surface. Instead of migrating to the step edges (Fig. 2.7.a), they exchange with underlying Ga-atoms Fig. 2.7.b), incorporated in the surface, in order to minimize the dangling - bond energy. Thus, in contrast to the ideal picture, one finds barriers of ternary alloy $\text{Al}_{x_B}\text{Ga}_{1-x_B}\text{As}$ (with $x_B < x_{Al}$) and equally wells of ternary alloy $\text{Al}_{x_w}\text{Ga}_{1-x_w}\text{As}$ (Fig. 2.6.b, left). Hereby it is assumed, that the lateral potential modulation is reduced, but preserves its form, e.g. barriers (wells, respectively) of width $L_\perp \cdot x_{Al}$ ($(1 - L_\perp) \cdot x_{Al}$, respectively). Under this assumption, one determines the concentrations to be $x_w = 0.037$ and $x_B = 0.303$, assuming the average Aluminum concentration $x_{aver} = 5\%$. By this segregation mechanism the lateral amplitude is reduced by a factor 3.8, thus obtaining a reduced amplitude of the lateral potential modulation of about 29 meV (Fig. 2.6.b (right)). Due to the assumption, that the form of the lateral potential modulation remains unchanged, the Fourier transform of the lateral potential modulation should

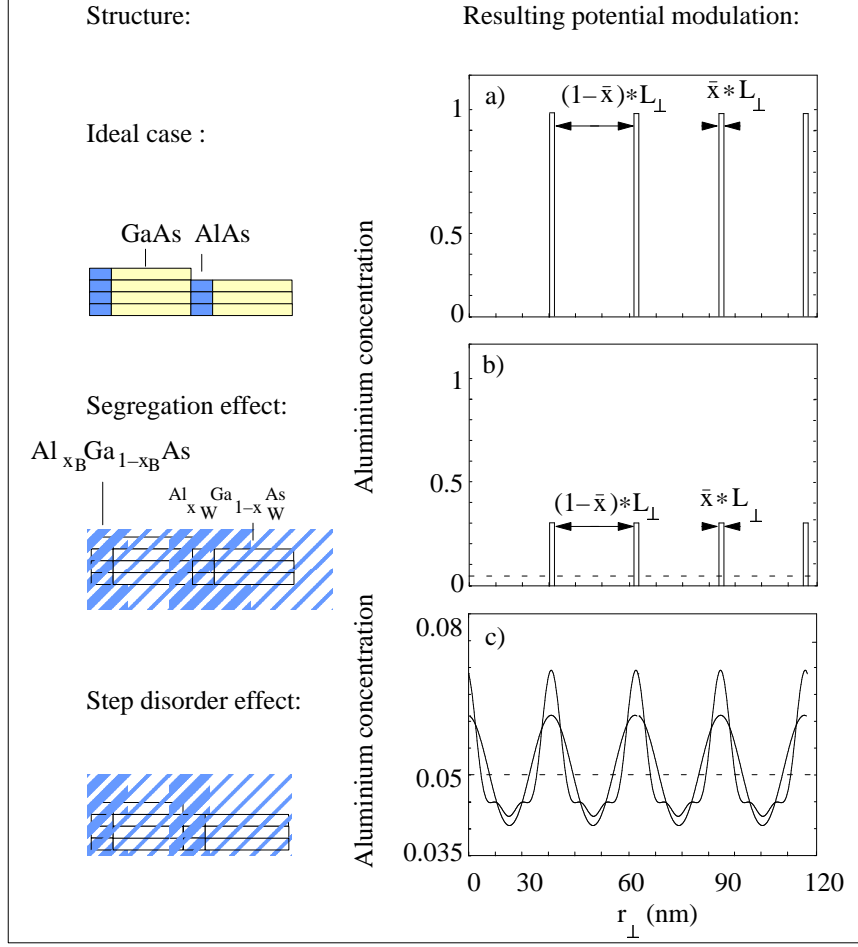


Figure 2.6: Sketch of the grown lateral superlattice (left) and corresponding lateral potential modulation (right). Due to segregation and disorder effects the lateral potential modulation is reduced by a factor 10 with respect to the ideal one. The thick line in Fig. c) corresponds to the lateral potential form, when taking two Fourier component into account, whereas the thin line corresponds to a sinusoidal lateral potential modulation.

display many components of order p given by

$$V_{at}^{(p)} = (x_B - x_w) \frac{\sin(p * \pi r_{\perp})}{p * \pi} \quad (2.18)$$

Equation 2.18 describes the atomic potential modulation V_{at} , resulting by taking only the segregation effect, but no other "damping effects", into account. The first term of the product on the right side of equation 2.18 is

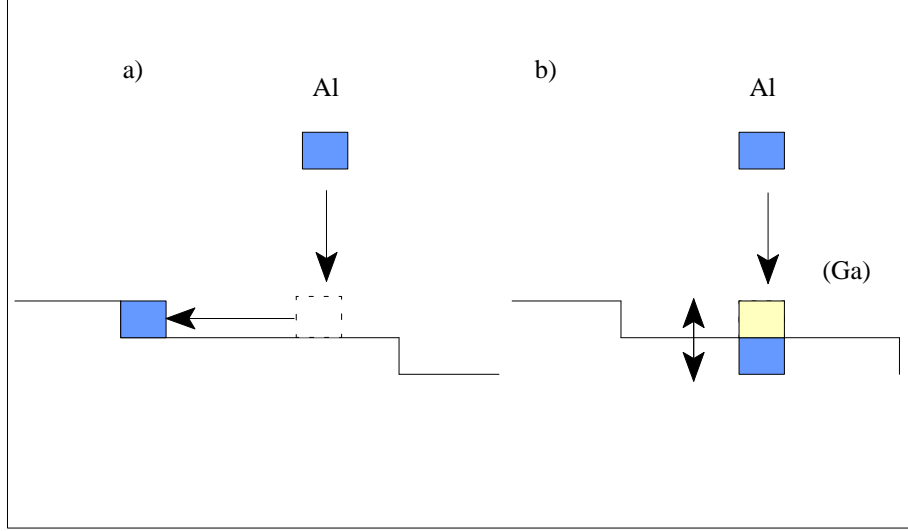


Figure 2.7: *Sketch of the segregation effect. Instead of migrating to the step (a), the on the surface impinging Al - atom exchanges with the underlying Ga - atom (b) for energetical and entropical reasons.*

due to the segregation effect and the second term describes the (standard) Fourier transformation of a rectangular function. As it is seen easily, the function decays slowly with p for small average Al - concentrations. In order to estimate the number of Fourier components to be taken into account, one is led to examine the second limiting factor: it is **the step disorder** of the GaAs step arrays. AFM - measurements ex - situ have allowed to visualize the vicinal surface [Lelarge 96]. Although showing a well defined periodicity at long distance (see Fig. 2.8.a), they exhibit step array fluctuations, which reduce each Fourier coefficient of the lateral potential modulation. The strength of the reduction is depending on the order of the considered Fourier component of the lateral potential modulation. Performing a 2 D - Fourier transformation of the ledge positions, three peaks centered at $k_{\parallel} = 0$, $k_{\perp} = \frac{2\pi p}{L_{\perp}}$ ($p = 1,2,3$) can be localized, giving directly access to each attenuation factor [Laruelle 99]. On a test sample (e.g. only a GaAs layer is grown, no Al is involved), it is found $V_{sd}^{(1)} = 0.4$, $V_{sd}^{(2)} = 0.2$ and $V_{sd}^{(i>2)} < 0.1$. Hence, taking more than three Fourier components into account in order to simulate the lateral potential modulation would not be justified. Consequently, the lateral potential will be smoothed and broadened (Fig. 2.6.c, left, thick line). However, it shall be emphasized that a simple sinusoidal lateral potential (e.g. considering only one Fourier component, as previously done, thin

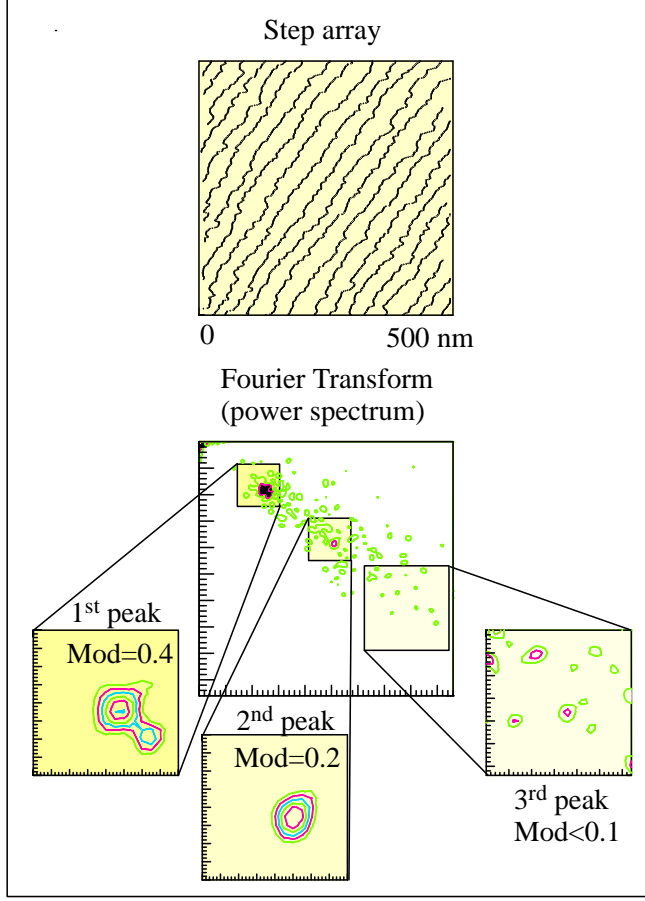


Figure 2.8: *AFM - image and its Fourier Transformed: Two Fourier peaks can be clearly identified, corresponding to $V_{sd}^{(1)} = 0.4$ and $V_{sd}^{(2)} = 0.2$, reducing the first Fourier component $V_{at}^{(1)}$ by 60% and the second one $V_{at}^{(2)}$ by 80%.*

line in Fig. 2.6.c) is not sufficient to understand the experimental results.

In summary, each Fourier component of the lateral potential modulation will accordingly be the product of a factor⁶ $V_{at}^{(p)}$, obtained by a growth model and a damping factor⁷ $V_{sd}^{(p)}$ determined on a GaAs template by AFM measurements. Since in real space the total lateral potential modulation $V_{mod}(r_{\perp})$ results from the convolution of these two effects, each Fourier component $V_{mod}^{(p)}$ of the lateral superlattice is just given as the product of the

⁶at = atomic, the atomic potential, having taken the segregation effect into account.

⁷sd = step - disorder, reduction factor due to step disorder.

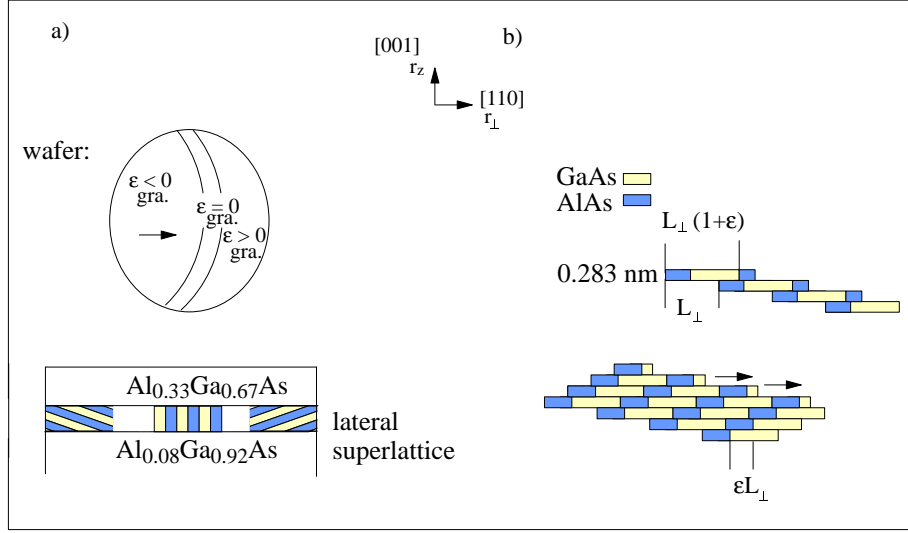


Figure 2.9: *Scheme of a tilted lateral superlattice: a) on each wafer there are zones, where there is an excess or reduction of group III - atoms with respect to one monolayer deposition. This leads to a tilted lateral superlattice (b).*

Fourier coefficients of each effect:

$$V_{mod}^{(p)} = V_{at}^{(p)} * V_{sd}^{(p)} \quad (2.19)$$

The number of Fourier components which can be taken into account is limited by the step disorder and is determined to be three. In the calculations, only the first two Fourier coefficients, which are clearly distinguishable, are taken into account.

An additional numerical difficulty, but experimental advantage, is the fact that each grown sample will have zones, where the lateral superlattice is tilted (see fig 2.9.a). This effect steams from the spatial variation of the flux of the elements of group III during MBE - growth. Due to this variation there are regions where the GaAs and AlAs coverage ratio $r = 1 + \epsilon$, defining the real amount of matter deposited per nominal monolayer (with ϵ being the coverage error) is not exactly equal to one: the lateral superlattice is tilted with respect to the growth axis in this region. Hence, the lateral potential modulation also depends on the r_z - direction [Mélin 98]:

$$V_{mod}(r_{\perp}, r_z) = \sum_p V_{mod}^{(p)} \cos[2p\pi(\frac{r_{\perp}}{L_{\perp}} + \epsilon \frac{r_z}{a})], \quad (2.20)$$

where a is the monolayer thickness.

The states $|\alpha, \vec{k}\rangle$ and $|\alpha', \vec{k}'\rangle$ are now coupled ($\alpha = \alpha'$: intrasubband coupling, $\alpha \neq \alpha'$: intersubband coupling). To obtain the expression for the inter - and intrasubband - coupling, one has to evaluate:

$$V^{(p)}(\alpha, \alpha', r_{\perp}) = \int_{r_z=0}^{r_z=Na} dr_z \xi_{\alpha}(r_z) V^{(p)}(r_{\perp}, r_z) \xi_{\alpha'}(r_z), \quad (2.21)$$

(N being the number of monolayers of the lateral superlattice) for each Fourier component p. The obtained lateral potential modulation $V_{mod}(r_{\perp})$ is weakened with respect to the untilted one (given in equat. 2.17) due to the cosines - integration along r_z . Physically, the weakening can be understood as the effect that the electrons "feel" simultaneously the periodic potential dephased in the r_z - direction.

The tilt of a lateral potential modulation can also be advantageously exploited by doing transport measurements on this wafer zone. One thus has access to two zones of different magnitude of the lateral potential on the same wafer, as will be seen in 6.2.3.

This is the lateral potential modulation, which will be inserted in the numerical calculations (detailed in the next chapter) to obtain the band-structure of a lateral modulated electron gas. It will or will not be a function of r_z , depending on the zone of the wafer which is studied.

2.2.3 Electronic Properties

If the periodicity of the lateral potential modulation is comparable to the Fermi wavelength (as it is the case in the structures studied in this work), the application of first order perturbation theory is no longer justified. Furthermore, the Thomas - Fermi method would not be very accurate and a two - dimensional calculation of the band structure in the self - consistent Hartree approximation is necessary. It takes into account the temperature dependent in-plane screening of the atomic modulation by the charge modulation along r_{\perp} [Etienne 96.1].

The principal difficulty to overcome is that one now has to solve the coupled Poisson and Schrödinger equations for a Hamiltonian, which is no longer to be separated in the r_{\perp} - and r_z - direction.

The Hamiltonian is written in the following manner:

$$H(r_z) = \frac{p_{r_z}^2}{2m^*} + V_{cryst.}(r_z) + V_{mod}(r_{\perp}, r_z) + V_{electrost.}(r_{\perp}, r_z) \quad (2.22)$$

The two first terms are identical to the one in the one - dimensional case.

$V_{mod}(r_{\perp}, r_z)$ describes the lateral potential modulation. Its average is taken to be zero, since the average is already included in $V_{cryst.}(r_z)$.

The Hartree term does not remain one - dimensional. It now couples the r_{\perp} and r_z direction due to the non-separability of the Coulomb potential. Hence, one is obliged to perform a fully 2D self - consistent Hartree calculation. The key ideas of the 2D - calculations will be presented in the following (a more detailed description can be found in [Etienne 96.2]), before discussing the results obtained by these calculations. These results show that the coupling between the r_{\perp} and r_z - direction is rather weak and one can assume the resulting wave functions to be proportional to only one subband - wavefunction. Consequently, one can neglect the coupling between the r_{\perp} - and r_z - direction if the lateral superlattice is not tilted for the transport calculations, which will be presented in chapter 3.

The Hartree potential and the charge distribution, which both have the same periodicity as the lateral potential modulation are developed in a Fourier series with $V_{electrost.}^m(r_z)$ ($\rho^m(r_z)$ respectively) being the m-th Fourier component of the Hartree potential (charge distribution).

The Poisson equation can then be written for each Fourier coefficient:

$$\frac{\partial^2 V_{electrost.}^m(r_z)}{\partial r_z^2} - \left(\frac{2\pi m}{L_{\perp}}\right)^2 V_{electrost.}^m(r_z) = -\frac{4\pi \rho^m(r_z)}{\epsilon_0 \epsilon_r} \quad (2.23)$$

with the following two boundary conditions:

- $V_{electrost.}(r_{\perp}, r_z = r_{z_{dop}}) = 0$. The underlying assumption is that the doped layer represents an equipotential surface (and hence the potential can be defined as 0). This is justified by the fact that the potential modulation diminishes exponentially as a function of r_z ($\sim e^{-\frac{n2\pi r_z}{L_{\perp}}}$, $n \in \mathbb{Z}$). Consequently, at the doping layer, the potential can be regarded as constant.
- The second hypothesis consists in the requirement, that away from the accumulation region, there does not exist any electric field: $\frac{\partial V_{electrost.}}{\partial r_z}(r_{\perp}, r_z \geq r_{z_{dep}}) \equiv 0$.

The Hamiltonian of equation 2.22 can be split into two parts:

$$H^0(r_z) = \frac{-\hbar^2}{2m^*} \frac{\partial^2}{\partial r_z^2} + V_{cryst.}(r_z) + V_{electrost.}^0(r_z) \quad (2.24)$$

$$\tilde{H}(r_z) = \frac{-\hbar^2}{2m^*} \frac{\partial^2}{\partial r_{\perp}^2} + V_{mod}(r_{\perp}, r_z) + V_{electrost.}(r_{\perp}, r_z) \quad (2.25)$$

As easily seen, $H^0(r_z)$ is equal to the one - dimensional, not on r_\perp depending, Hamiltonian in equation 2.10. The Hamiltonian $H^0(r_z)$ represents the one of a heterostructure which has no lateral modulation, but the same average of Aluminum concentration in the channel. Consequently, the eigenstates and eigenvalues of the heterostructures are known by the calculation discussed in the previous section.

The wave functions one is looking for are Bloch functions in the perpendicular direction, possessing the periodicity of the lateral potential modulation.

A reasonable Ansatz to take into account the variations of the lateral potential in the r_z - direction is thus to develop the r_z - dependent part on the set of eigenfunctions ξ_α , given by the 1D bandstructure calculations.

Hence, the wavefunction can be written as (A is the surface sample)

$$\Phi_{\alpha,p,k_\perp}(r_\perp, r_z) = \frac{1}{\sqrt[4]{A}} \left[\sum_\alpha \xi_\alpha(r_z) \phi_{p(\alpha),k_\perp} \right] \quad (2.26)$$

The periodic part of the Bloch function⁸ is developed in a Fourier series:

$$\Phi_{\alpha,p,k_\perp}(r_\perp, r_z) = \frac{1}{\sqrt[4]{A}} \left[\sum_\alpha \xi_\alpha(r_z) \sum_p a_{p(\alpha),k_\perp} e^{i \frac{2\pi p}{L_\perp}} \right] e^{i k_\perp r_\perp} \quad (2.27)$$

As it is seen from equation 2.27, the modulated wave function is developed on the base of the wave - functions of a non - modulated electron gas with vector $k_\perp + p \cdot 2\pi/L_\perp$. The Hamiltonian is diagonalized in that base for each value of k_\perp . The charge distribution is calculated by starting with these wave functions and their subband occupation (given by the 1 D calculation of the previous chapter), including also Fermi Dirac statistics at finite temperature. This charge distribution is then introduced in the Poisson equation, which is solved by a Green resolved function. This cycle continues until the convergence limit is obtained, e.g. just until the Hartree term $V_{electrost.}(r_\perp, r_\perp)$ and the charge distribution $\rho(r_\perp, r_z)$ are coherent.

Fig. 2.10 shows an example of a typical (screened) potential in the r_\perp -, r_z - direction (r_\parallel direction is omitted). The amplitude of the lateral potential modulation $V_{peaktopeak}$ is assumed to be 23 meV. One clearly recognizes (from the left to the right): The barrier, the channel in which the lateral potential is seen in r_\perp direction, and the vertical superlattices to avoid the charge transfer far from the interface.

⁸It shall be again reminded that the Bloch part of the wave function is due to the lateral potential modulation

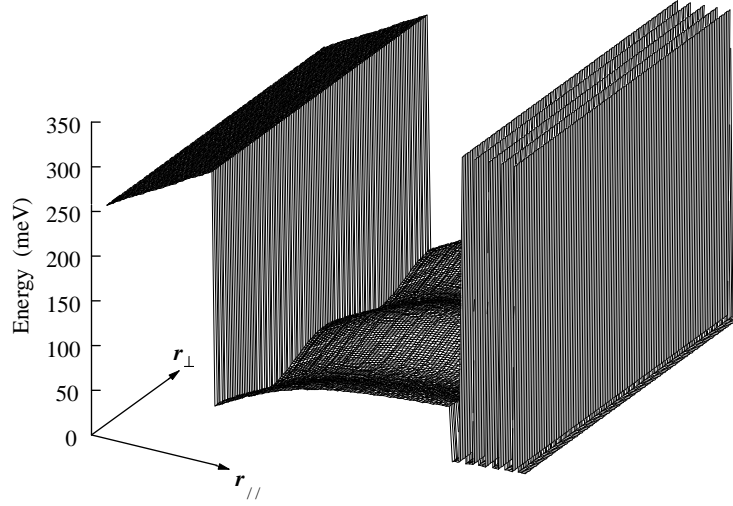


Figure 2.10: *Lateral screened potential modulation in real space. From left to right: The barrier, the channel in which the lateral potential is seen in r_{\perp} direction, and the vertical superlattice to avoid the charge transfer far from the interface.*

Fig. 2.11 shows the corresponding energy dispersion as a function of k_{\perp} in reduced Brillouin zone. The result of taking the first two Fourier components of the lateral modulation (as discussed in the previous section) into account is shown in thick lines in Fig. 2.11. For comparison reasons, the resulting bandstructure, while taking only the first Fourier component into account, is equally shown.⁹ It shall be reminded that the first index refers to the subband, the second to the miniband index. For the samples studied in this work the Fermi energy lies in the middle of the second miniband, when no electrical field is applied. Emphasis shall be drawn to the fact that, by taking the first two Fourier components into account, the size of the second minigap is comparable to the first minigap. In contrast, by taking only the first Fourier component into account, the second minigap is very small. This is now understandable: The states $k_{\perp} = \pm 2\pi/L_{\perp}$ are coupled by the **second** Fourier component, resulting in the opening of the second minigap. Additionally, the second minigap is not screened since in the structures, studied in this work, one has $2\pi/L < 2k_F < 4\pi/L$. Also observable in

⁹The first minigap is slightly smaller, when taking V^2 into account. This stems from the second order energy shift, which is of opposite sign.

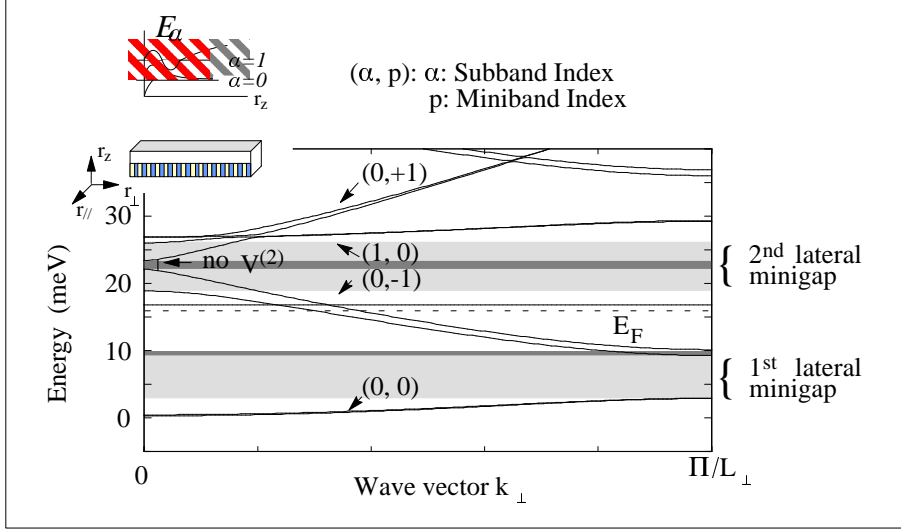


Figure 2.11: *Energy vs k_{\perp} in reduced Brillouin zone: thick lines: resulting potential modulation, while taking the first two Fourier components into account, thin line: only the first Fourier components is taken into account. Taking the first two Fourier components into account, the second minigap is of comparable size to the first one.*

Fig. 2.11 is the weak coupling between subbands (~ 0.05 meV). This allows to separate the wave functions in r_{\perp} - and r_z - direction of the modulated system:

$$\Phi_{\alpha,p,k_{\perp}}(r_{\perp}, r_z) = \frac{1}{\sqrt[4]{A}} \xi_{\alpha}(r_z) \sum_p a_{p(\alpha),k_{\perp}} e^{i \frac{2\pi p}{L_{\perp}} r_{\perp}} e^{i k_{\perp} r_{\perp}} \quad (2.28)$$

Physically, it is possible to separate the r_{\perp} - dependent part of the wave function from the r_z - dependent one, because it is only the screening potential $V_{electrost.}(r_{\perp}, r_z)$ (in the case of the untilted LSL), which couples both directions. However, $V_{electrost.}(r_z)$ ($\rho^m(r_z)$) varies very little on the size of the extension of the subband wavefunction $\xi_{\alpha}(r_z)$ in comparison to the energetical distance between two subbands. This separability in the wave functions is exploited in the calculations of the transport properties.

Summarizing this paragraph, the energy dispersion obtained by the band structure of an electron in a subband α will have the form

$$E_{\alpha}(k_{\parallel}, k_{\perp}) = \frac{\hbar^2 k_{\parallel}^2}{2m^*} + E_{\alpha}(k_{\perp}), \quad (2.29)$$

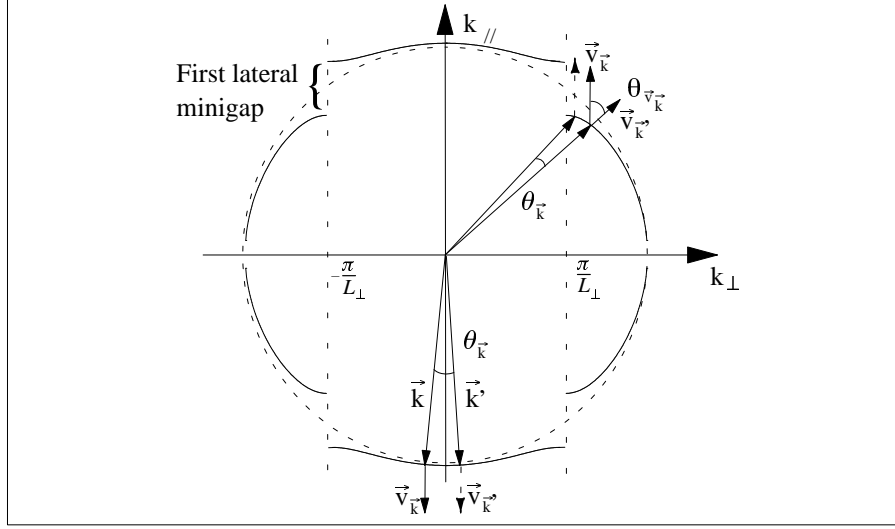


Figure 2.12: *The Fermi energy surface of an modulated 2DEG. For comparison, the Fermi energy surface of an unmodulated 2DEG is shown (dashed line). The discontinuity at the BZ edges due to the minigaps are clearly observable.*

having the free energy dispersion in $r_{||}$ - direction and the one above discussed in r_z - direction for each subband. From this energy dispersion it is straightforward to obtain the Fermi surface¹⁰, shown in Fig. 2.12. The Fermi surface of an unmodulated 2DEG is given as reference in dashed line. It is important to realize that the Fermi surface of the modulated electron system remains basically a circle. The difference with respect to the unmodulated 2DEG manifests itself mostly at the zone edges of the Brillouin zone, where the minigaps lead to a discontinuity of the Fermi surface. This form of the Fermi surface indicates that the electron properties are not simply described by a direction dependent effective mass as done in the work of [Hirakawa 86]. Rather, the transport properties emerge to a great extent from the modification of the group velocity $\vec{v}_{\vec{k}}$ of each state \vec{k} ($\vec{v}_{\vec{k}} \sim \frac{\partial E}{\partial \vec{k}}$). One is thus led to calculate a $\frac{\vec{k}}{|\vec{k}|}$ - dependent collision time. Due to the relation

$$D(E) = \oint_{\Sigma_E} \frac{d\vec{k}}{v_{\vec{k}}} \quad (2.30)$$

one immediately obtains the density of state $D(E)$ as a function of energy.

¹⁰The term "Fermi surface" is kept in analogy to the three dimensional case, though it would be more correct to speak of a "Fermi line".

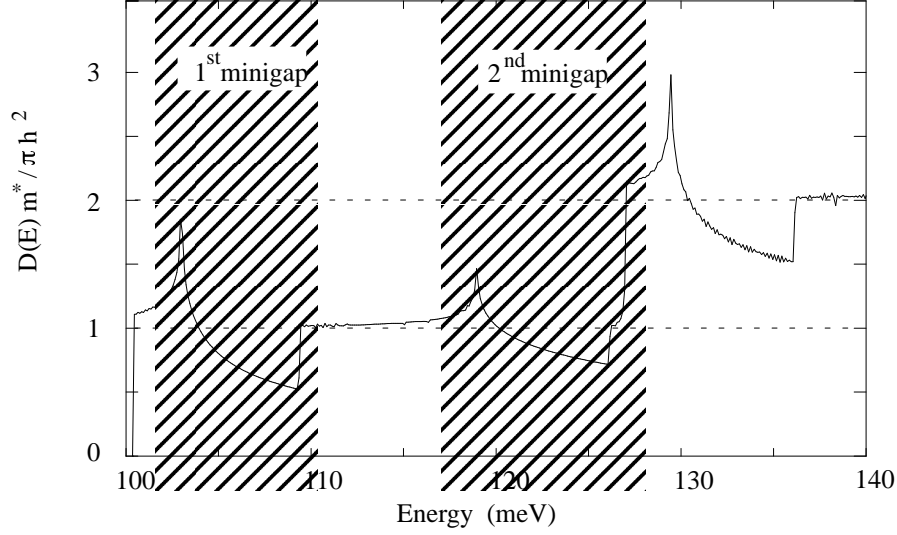


Figure 2.13: *Density of state as a function of energy at $T = 0K$: The two minigaps in the first subband manifest themselves by the 1D density of state behavior. For comparison, in dashed line the constant two dimensional density of state is equally shown.*

Σ_E designs constant energy surfaces over which will be integrated. Once again, as a reference, the constant state density $\frac{m^*}{\pi\hbar^2}$ of a two dimensional unmodulated electron gas is indicated in dashed line. One identifies clearly the on - set of the first (at 100.4 meV) and second electrical subband (at 127.8 meV). More important, one finds the signature of the two first minigaps in the first subband, having the typically one -dimensional behavior ($\sim \frac{1}{\sqrt{E}}$) of the density of states. The density of states remains one - dimensional, because the minigaps exist only in the perpendicular direction, whereas in the parallel direction the free electron motion continues. All these figures were obtained by executing the band - structure calculation at $T = 0K$.

Influence of the temperature While the atomic potential of the lateral modulation does not depend on the temperature, the electron distribution does. And consequently does the charge distribution $\rho(r_{\perp}, z)$. Thus, the temperature has an influence of the screening potential and hence on the resulting total modulation. This is the reason, why one has to recalculate the bandstructure for each temperature.

Chapter 3

The Boltzmann Transport Equation

The aim of this thesis is to understand the transport properties of modulated 2DEG's. To support and understand the experimental data, a theoretical analysis of the transport properties (without magnetic field) will be later presented. The results of this analysis are obtained by solving the linearized, semi - classical Boltzmann transport equation [Calecki 69] in a relaxation time approximation. The solution obtained by this method is exact if the system is isotrop and if only elastic collisions take place [Ashcroft 76]. In the anisotropic case (e.g. for the modulated 2DEG) we follow Ziman [Ziman 61] and define a $\frac{\vec{k}}{|\vec{k}|}$ - dependent relaxation time. A similar approach has been chosen by Gerhardtts and Menne [Menne 98] to calculate the magnetic field dependent conductivity.

After having introduced the Boltzmann equation, special emphasize is given to the screening mechanisms. One of the results of this work will be the demonstration of the necessity of including higher subbands in the dielectric function calculations at higher charge density or higher temperature. This is equal to say that one does no longer consider the dielectric function as a scalar. Consequently, as will be shown in the end of this chapter, the transition probabilities have to be calculated differently.

Starting point for the numerical calculations is the linearized semi-classical Boltzmann equation, given by

$$\vec{F}^{ext} \frac{1}{\hbar} \frac{\partial g(\vec{k})}{\partial \vec{k}} = \frac{\partial g(\vec{k})}{\partial t} |_{coll}, \quad (3.1)$$

where

- $g_\alpha(\vec{r}, \vec{k}, t)$ is the non equilibrium function defined so that $g_\alpha(\vec{r}, \vec{k}, t) d\vec{r} d\vec{k} / 4\pi^3$ is the number of electrons in the α - th band at time t in the semi - classical phase space volume $d\vec{r} d\vec{k}$ about the point \vec{r}, \vec{k} . In equilibrium $g_\alpha(\vec{r}, \vec{k}, t)$ reduces to the Fermi Dirac Function

$$g_\alpha(\vec{r}, \vec{k}, t) = g_\alpha^0(\vec{r}, \vec{k}, t) \equiv f(\epsilon_\alpha(\vec{k}))$$

with

$$f(\epsilon_\alpha(\vec{k})) = \frac{1}{\exp\left(\frac{\epsilon_\alpha(\vec{k}) - E_F}{k_B T}\right) + 1},$$

but in the presence of applied fields (as it is usually the case) and / or temperature gradients it will differ from its equilibrium distribution. It can be written as $g_\alpha(\vec{r}, \vec{k}, t) = g_\alpha^0(\vec{r}, \vec{k}, t) + g_\alpha^1(\vec{r}, \vec{k}, t)$, where $g_\alpha^1(\vec{r}, \vec{k}, t)$ refers to the perturbation term, e.g. describes the deviation from equilibrium function.

- \vec{F}^{ext} is the sum of all external forces, e.g.

$$\vec{F}^{ext}(\vec{r}, \vec{k}) = -e\vec{E} + \frac{1}{c}\vec{v} \times \vec{H}$$

where \vec{E} is the electrical field and \vec{H} the magnetic field.

Equation 3.1 describes the "equilibrium" between the "accelerating" action of the external fields (e.g. electric, magnetic field) and the "slowing down" actions of the internal forces (e.g. collisions).

The complexity of this equation comes from the collision term $\frac{\partial g}{\partial t}|_{coll}$ and will be treated in the next section.

3.1 Scattering Probability

Making the assumptions that

- there is a calculable probability per unit time (determined by suitable microscopic calculations) that an electron in band α with wave vector $\vec{k} = (k_{\parallel}, k_{\perp})$ will, as a result of a collision, be scattered into band α' with wave vector \vec{k}' (assuming spin conversation).
- Collisions can be well localized in space and time, so that the collision occurring at \vec{r} , t are determined by properties of the solid in the immediate vicinity of \vec{r} and by the time interval $(t - \delta t)$.

one can define a scattering probability which is given by the quantity $P_{\alpha'\alpha}(\vec{k}'\vec{k})$. The quantity

$$\frac{P_{\alpha'\alpha}(\vec{k}'\vec{k})dt d\vec{k}'}{(2\pi)^2},$$

expresses the probability that an electron with wave vector \vec{k} of subband α will be scattered into any one of the group of levels (with the same spin) contained in the infinitesimal k-space volume element $d\vec{k}'$ about \vec{k}' in the subband α' (assuming that these levels are all unoccupied and therefore not forbidden by the exclusion principle) in an infinitesimal time interval dt .

The particular form taken by $P_{\alpha'\alpha}(\vec{k}'\vec{k})$ depends on the particular scattering mechanism and will be discussed in more detail in section 3.7.

Having defined this transition probability, the collision term can be expressed by

$$-\frac{\partial g_{\alpha}^0}{\partial t}|_{coll} = -e\vec{E}\vec{\nabla}(\vec{k})\left(\frac{\partial g_{\alpha}^0}{\partial E}\right) = \sum_{\alpha'=1}^N P_{\alpha'\alpha}(\vec{k}'\vec{k})[g_{\alpha}^1(\vec{k}) - g_{\alpha'}^1(\vec{k}')]. \quad (3.2)$$

This is remarkable in that sense that it is only the deviation $g_{\alpha}^1(\vec{k})$ from the equilibrium function who determines the collision term.

3.2 Solution of the Boltzmann Equation

Once again, the difficulty in finding a solution arises from the complexity of the collision term. Only for very special cases this equation is analytically solvable. In the following a solution of the Boltzmann Transport equation will be derived, having made the following assumptions:

- the effective mass m^* is direction independent.
- the transition probability does not depend on the distribution function $g_\alpha(\vec{k})$.
- all scattering events are elastic or quasi - elastic, i.e. $E_\alpha(\vec{k}) = E_{\alpha'}(\vec{k}')$.

Under these assumptions one readily finds[Siggia 70] :

$$g_\alpha^1(\vec{k}) = -e\tau_\alpha(E_\alpha(\vec{k}))\left[\frac{\hbar}{m^*}\vec{k} \cdot \vec{E}\right]\frac{\partial g_\alpha^0(\vec{k})}{\partial E} \quad (3.3)$$

where τ_α is the relaxation time discussed in the next section.

3.3 Relaxation Time τ

3.3.1 Relaxation Time τ for an Unmodulated 2DEG

In an unmodulated 2DEG the relaxation time τ is a function of energy, but does not depend explicitly on \vec{k} due to its isotropic Fermi energy surface. It is defined by [Mori 80]

$$-\frac{\partial g_\alpha(\vec{k})}{\partial t}\Big|_{coll} = \frac{g_\alpha^1(\vec{k})}{\tau_\alpha(E)} \quad (3.4)$$

i.e. it is inversely proportional to the collision term. This is intuitively understandable, if one considers what happens when the external forces have been removed instantaneously. In this case the perturbation in the distribution function will be changed due to collisions and decay exponentially:

$$g_\alpha^1(\vec{k}, t) = g_\alpha^1(\vec{k}, 0)e^{-\frac{t}{\tau(E)}} \quad (3.5)$$

The time $\tau(E)$ thus represents a system characteristic time constant for the relaxation of the perturbation, i.e. the time until the unperturbed system has reached its thermodynamic equilibrium.

$\tau(E)$ is determined by the coupled Boltzmann equations[Siggia 70]

$$\tau_\alpha(E)W_{\alpha\alpha}(\vec{k}, \vec{k}') - \sum_{\alpha \neq \alpha'} W_{\alpha\alpha'}(\vec{k}, \vec{k}')\tau_{\alpha'}(E) = 1. \quad (3.6)$$

with

$$\begin{aligned}
W_{\alpha\alpha}(\vec{k}, \vec{k}') &= \frac{2\pi}{\hbar} \int_{\Sigma_E} \frac{d^2k'}{(2\pi)^2} | \langle \alpha' \vec{k}' | V^{scatt.} | \alpha \vec{k} \rangle |^2 (1 - \cos\theta) \delta(E_\alpha(\vec{k}) - E_{\alpha'}(\vec{k}')) \\
&\quad + \sum_{\alpha' \neq \alpha} \frac{2\pi}{\hbar} \int \frac{d^2k'}{(2\pi)^2} | \langle \alpha' \vec{k}' | V_{diff} | \alpha \vec{k} \rangle |^2 \delta(E_\alpha(\vec{k}) - E_{\alpha'}(\vec{k}')) \\
W_{\alpha\alpha'}(\vec{k}, \vec{k}') &= W_{\alpha'\alpha}(\vec{k}', \vec{k}) = \frac{2\pi}{\hbar} \frac{k_{\alpha'}}{k_\alpha} \int \frac{d^2k'}{(2\pi)^2} | \langle \alpha' \vec{k}' | V_{diff} | \alpha \vec{k} \rangle |^2 * \\
&\quad \cos\theta \delta(E_\alpha(K) - E_{\alpha'}(K'))
\end{aligned}$$

with $\Sigma(E)$ being a constant energy surface and $d^2k = dk_x dk_y$. The matrix element $| \langle \alpha' \vec{k}' | V_{diff} | \alpha \vec{k} \rangle |^2$ describes the transition probability per unit time from the state $|\alpha, \vec{k}\rangle$ to the state $|\alpha', \vec{k}'\rangle$ due to a scattering potential. This will be discussed in more detail in the next section.

In the case of the electrical quantum limit equation 3.6 simplifies to

$$\frac{1}{\tau_\alpha(E)} = \int_{\Sigma_E} \frac{d^2k}{2\pi\hbar} | \langle \alpha' \vec{k}' | V^{diff} | \alpha \vec{k} \rangle |^2 (1 - \cos\theta) \delta(E_\alpha(\vec{k}) - E_{\alpha'}(\vec{k}')) \quad (3.7)$$

with θ being the angle between the state $|\vec{k}\rangle$ and $|\vec{k}'\rangle$. Hence, every scattering event is averaged over its projection of the outgoing wave vector on the incident direction. The relaxation time is thus inversely proportional to the (integrated) probabilities of transitions into and out of each state $|\vec{k}\rangle$, weighted by an angle dependent factor to allow for the big effect on the change of the distribution function of scattering through large angles. The averaged geometrical factor

$$\langle 1 - \cos\theta \rangle = \frac{\int_{\Sigma(E)} \frac{d^2k}{2\pi\hbar} | \langle \alpha \vec{k}' | V^{scatt.} | \alpha \vec{k} \rangle |^2 (1 - \cos\theta) \delta(E_\alpha(\vec{k}) - E_{\alpha'}(\vec{k}'))}{\int_{\Sigma(E)} \frac{d^2k}{2\pi\hbar} | \langle \alpha \vec{k}' | V^{diff} | \alpha \vec{k} \rangle |^2 \delta(E_\alpha(\vec{k}) - E_{\alpha'}(\vec{k}'))} \quad (3.8)$$

will strongly depend on the type of interaction potential V^{diff} , one is considering. If one considers a scattering potential, which depends on the scattering vector $\vec{q} = \vec{k} - \vec{k}'$ and hence on θ ($\vec{q} = 2\vec{k}_F \sin(\theta/2)$), one can have favored forward scattering, e.g. $\langle 1 - \cos\theta \rangle < 1$, $\theta < 90^\circ$ or backward scattering, i.e. $\theta > 90^\circ$ (see also Fig. 3.1). On the opposite, for a q -independent scattering potential the term $\langle 1 - \cos\theta \rangle$ will be equal to one, expressing the equal probability of having forward and backward scattering.

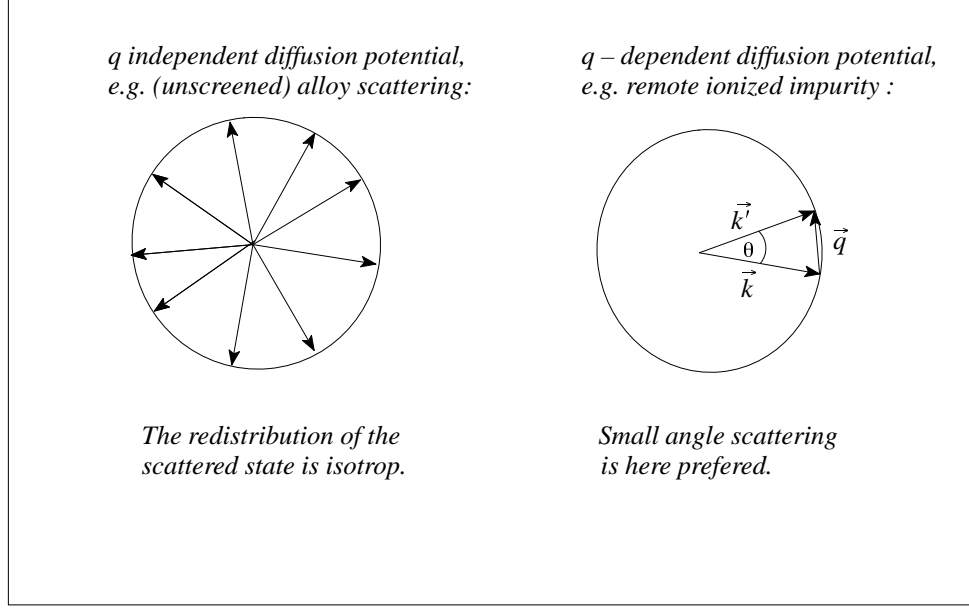


Figure 3.1: *Sketch of the q - dependence of different scattering potentials: while forward and backward scattering have equal probabilities in the case of an q - independent scattering potential, small (or large) angle scattering is strongly favored in the case of a q - dependent scattering potential.*

3.3.2 Relaxation Time τ for a Modulated 2DEG

In a modulated 2DEG the assumption of a $\frac{\vec{k}}{|\vec{k}|}$ - independent relaxation time is no longer valid due to the anisotropic Fermi energy surface. Nevertheless, one can try to find an approximated expression by defining a \vec{k} - dependent relaxation time $\tau(\vec{k})$ [Ziman 61]. $\tau(\vec{k})$ can be interpreted, in analogy to the isotropic case, as a characteristic time for the desexcitation of **one** state \vec{k} . In the following the notation $\vec{\kappa} = (\alpha, \vec{k})$ shall be used.

Starting again from equ. 3.4 (but with a $\vec{\kappa}$ - dependent relaxation time)

$$-\frac{\partial g(\vec{\kappa})}{\partial t}\bigg|_{coll} = \frac{g^1(\vec{\kappa})}{\tau(\vec{\kappa})}, \quad (3.9)$$

one obtains

$$\frac{1}{\tau_\alpha(\vec{\kappa})} = \sum_{\kappa'} W(\vec{\kappa}, \vec{\kappa}') \left[1 - \frac{g^1(\vec{\kappa}')}{g^1(\vec{\kappa})} \right]. \quad (3.10)$$

Inserting equat. 3.3 in equ. 3.10, one deduces:

$$\frac{1}{\tau(\vec{\kappa})} = \sum_{\kappa'} W(\vec{\kappa}, \vec{\kappa}') \left[1 - \frac{\tau(\vec{\kappa}')}{\tau(\vec{\kappa})} \frac{\vec{E} \cdot \mathbf{v}(\vec{\kappa}')}{\vec{E} \cdot \mathbf{v}(\vec{\kappa})} \right]. \quad (3.11)$$

One clearly realizes that now each relaxation time for one state $\vec{\kappa}$ depends on all the other $\vec{\kappa}$ - dependent relaxation times. Equation 3.11 can be simplified to

$$\frac{1}{\tau(\vec{\kappa})} = \sum_{\kappa'} W(\vec{\kappa}, \vec{\kappa}') \left[1 - \frac{\tau(\vec{\kappa}')}{\tau(\vec{\kappa})} \frac{\vec{v}(\vec{\kappa}')}{\vec{v}(\vec{\kappa})} \right] (\cos\theta - \tan\alpha \sin\theta), \quad (3.12)$$

where α is chosen as the angle between the electrical field \vec{E} and the vector \vec{k} . Since one is only looking for solutions linear in the electrical field, the transport time $\tau(\vec{\kappa})$ does not depend on the electrical field \vec{E} . Consequently, the α - dependent term is 0 and it remains:

$$\frac{1}{\tau(\vec{\kappa})} = \sum_{\kappa'} W(\vec{\kappa}, \vec{\kappa}') \left[1 - \frac{\tau(\vec{\kappa}')}{\tau(\vec{\kappa})} \frac{\vec{v}(\vec{\kappa}')}{\vec{v}(\vec{\kappa})} \right] \cos\theta, \quad (3.13)$$

The angle θ has not been defined yet: In an unmodulated 2DEG, the angle θ is chosen as the angle between the state $|\vec{k} >$ and $|\vec{k}' >$, which is identical to the angle between the group velocities of state $|\vec{k} >$ and $|\vec{k}' >$ (e.g. $\vec{v}(\vec{k}') \parallel |\vec{k} >$). Contrarily, in an modulated 2DEG, due to the anisotropic Fermi surface, the assumption that the angle between the states (\vec{k}, \vec{k}') is equal to the angle between the group velocities $\vec{v}(\vec{k}')$ is no longer justified. In the chapter and 5.4.3, comparison will be made between the calculated mobilities, taking θ as the angle between the wave vector states and taking θ as the angle between the group velocities of states \vec{k} and \vec{k}' . Intuitively, one can try to justify this choice by having in mind that the relaxation time $\tau(\vec{\kappa})$ of a system should not be affected by forward scattering, e.g. if $\vec{v}(\vec{k}') \parallel \vec{v}(\vec{k})$, and be strongly affected by backward scattering, e.g. $\vec{v}(\vec{k}') \parallel -\vec{v}(\vec{k})$. This is mathematically taken into account by choosing θ as the angle of the group velocities rather than taking the angle θ_k between the states $|\vec{k} >$ and $|\vec{k}' >$. But, as mentioned above, taking θ as the angle between the group velocities cannot be justified rigorously [Ziman 61].

For the numerical calculations, the auto - coherency of equation 3.13 will be ignored. Thus the transport time can be written formally identical to the transport time of an unmodulated electron gas,

$$\frac{1}{\tau_\alpha(\vec{k})} = \int_{\Sigma_E} \frac{d^2k}{2\pi\hbar} |\langle \alpha\vec{k}' | V^{diff} | \alpha\vec{k} \rangle|^2 (1 - \cos\theta) \delta(E_\alpha(\vec{k}) - E_{\alpha'}(\vec{k}')) \quad (3.14)$$

but this time with a \vec{k} - dependent relaxation time.

3.4 Calculation of the Macroscopic Quantities

Once having calculated the relaxation time $\tau_\alpha(\vec{k})$, the diagonal components of the conductivity tensor are obtained in the usual manner:

$$\begin{aligned} \sigma_{\beta\beta}(T=0) &= \sum_\alpha \int_{\Sigma_{E_F}} d^2k g^1(\vec{k}) \quad (\beta = r_\parallel, r_\perp) \\ &= \frac{e^2}{2\pi^2} \sum_\alpha \int_{\Sigma_{E_F}} d^2k \left(-\frac{\partial g^0(\vec{k})}{\partial E} \right) \tau(\vec{k}) \vec{v}_\beta^2(\vec{k}). \end{aligned} \quad (3.15)$$

The integral over $d^2\vec{k}$ signifies that one integrates over the constant energy surfaces Σ_{E_F} : $d^2k = dk_\parallel dk_\perp$ where dk_\parallel is the element of the surface of Σ_E and $dk_\perp = dE/\hbar v_{\vec{k}}$.

The temperature dependence of the conductivity is given by the statistical weight $\partial g^0(\vec{k})/\partial E$:

$$\sigma_{\beta\beta}(T) = \int dE \left(-\frac{\partial g^0(\vec{k})}{\partial E} \right) \sigma_{\beta\beta}(E) \quad \text{with} \quad (3.16)$$

$$\sigma_{\beta\beta}(E) = \frac{e^2}{2\pi\hbar} \sum_\alpha \oint_{\Sigma_E} \frac{dk}{v_K} \tau(\vec{k}) \vec{v}_\beta^2(\vec{k}), \quad (3.17)$$

where Σ_E corresponds to all constant energy surfaces lying in the energy range $\Delta E = E_F \pm 6k_B T^1$. Accordingly, at $T = 0K$ only states of the Fermi surface contribute to the conductivity, whereas at finite temperature states in between $E_F \pm 6k_B T$ contribute to the conductivity.

In the case of an unmodulated 2DEG, the integral of the energy surface is equal to $2\pi E/\hbar$ and one obtains (α corresponds to the α - th subband):

¹n = 6 is chosen throughout the whole work. It is chosen such that 99.8% of the population is included, when integrating over the Fermi - Dirac distribution function between $E_F - 6k_B T$ and $E_F + 6k_B T$.

$$\sigma_{\alpha\alpha}(E) = \frac{e^2}{\pi\hbar} \int_{\Sigma E} dE \frac{-\partial g_{\alpha}^0(E)}{\partial E} E \tau_{\alpha}(E) \quad (3.18)$$

Introducing explicitly the charge density of the α - th subband:

$$N_{\alpha} = \frac{m^*}{\pi\hbar^2} \int dE g_{\alpha}^0(E) = \frac{m^*}{\pi\hbar^2} \int dE \frac{-\partial g_{\alpha}^0(E)}{\partial E} E$$

one finds the habitual form (Drude form) of the conductivity of the α -th subband:

$$\sigma_{\alpha\alpha}(E) = \frac{N_{\alpha} e^2 \bar{\tau}_{\alpha}}{m^*} \quad (3.19)$$

with

$$\bar{\tau}_{\alpha} = \frac{\int dE \frac{-\partial g_{\alpha}^0}{\partial E} E \tau_{\alpha}(E)}{\int dE \frac{-\partial g_{\alpha}^0}{\partial E} E}.$$

$\tau_{\alpha}(E)$ has to be determined by the coupled equations of equat. 3.6.

3.5 Scattering Processes

According to the Bloch theorem [Ashcroft 76], an electron in a perfectly periodic array of atoms experiences no collisions at all. So, within the independent electron approximation, collisions can only arise from deviations from perfect periodicity.

These deviations fall into two broad categories:

1. Extrinsic deviations from periodicity in a perfect crystal.

Impurities of point defects (e.g. ions in the "wrong" place) provide a localized scattering center. In this work, the scattering due to ionized impurities in the barrier, impurities in the channel and scattering due to the alloy given in our structures (normally 5 % Aluminum in the channel) will be discussed.

2. Intrinsic deviations from periodicity in a perfect crystal.

Intrinsic deviations are due to thermal vibrations of the atoms. The ions do not remain rigidly fixed at the points of an ideal periodic array, since they possess some kinetic energy which increases with higher

temperature. At low temperature the kinetic energy enables the ions only to undergo small vibrations and the scattering mechanism is not important. Increasing the temperature, the scattering mechanism becomes more and more important. We take acoustic phonon scattering in our calculations into account, but neglect optical phonons. This is justified because we are only concerned with temperatures up to 70K, where scattering due to optical phonons plays a minor role.

All the scattering processes are considered as elastic scattering processes. This signifies that the state does not alter its energy, e.g. $E_{\alpha}^{before}(\mathbf{k}) = E_{\alpha'}^{after}(\mathbf{k})$. (As a consequence, changing the subband means, changing the kinetic energy of the charge, but not its total energy E.)

In all calculations the validity of the Born approximation is assumed. This is equal to say that one considers the (already screened, see next section) scattering potential sufficiently small to apply perturbation theory and to consider only the first term ("Fermi's Golden rule"). Thus the transition probability (e.g. the probability that an electron of the α - th subband with wave vector \vec{k} will be scattered in the α' - th subband into the state \vec{k}') is given by

$$W_{\alpha\alpha'}(\vec{k}, \vec{k}') = \frac{2\pi}{\hbar} |\langle \alpha' \vec{k}' | V^{scatt.} | \alpha \vec{k} \rangle|^2 \delta(E_{\alpha'}(\vec{k}') - E_{\alpha}(\vec{k})). \quad (3.20)$$

Before discussing each scattering process in detail, the response of the electrons towards an external potential (e.g. scattering potential) shall be explained.

3.6 Screening of an Electron Gas: Dielectric Constant $\epsilon(\vec{q})$

By calculating the screening of an electron gas, one has access to the screened scattering potential $V^{scatt.}$ which is introduced in the scattering matrix elements, discussed in the previous section. Naturally, the interaction between a scattering center and an electron is strongly modified by the presence of the other electrons. The scattering center induces in fact a perturbation potential, which acts on all electrons surrounding this center. The electrons "react" by rearranging themselves, leading to a spatially dependent charge density in the electron gas. This Coulomb potential created by the electrons

and opposed to the perturbation potential is called screening potential. The equilibrium, described by an auto - coherent solution, which includes these two (antagonist) potentials, leads to a reduced perturbation potential $V^{scatt.}$. It is the effect of screening which finally defines the strength of this scattering potential $V^{scatt.}$ by which the electrons are scattered. So it is very important to describe the screening adequately.

Describing the effect of screening, there are two physical involved quantities which are closely related:

- the polarizability function $\Pi(\vec{q}, T, E_F)$ of a system.
- the dielectric function $\epsilon(\vec{q}, T, E_F)$ of a system

Both physical quantities become important when different screening models are discussed in Chapter 5.1 and are introduced in the following.

Assuming the considered system homogeneous and translational invariant, the polarizability function $\Pi(\vec{Q}, T, E_F)^2$ relates the external applied potential with the induced charge density in Fourier space by [Ashcroft 76]

$$\rho^{ind}(\vec{Q}) = \Pi(\vec{Q}) V^{ext}(\vec{Q}). \quad (3.21)$$

with the polarizability $\Pi(\vec{Q})$ defined as

$$\Pi(\vec{Q}) := -e^2 \int^3 \frac{d\vec{K}}{4\pi^3} \frac{g^0(\vec{K} + \vec{Q}) - g^0(\vec{K})}{\frac{\hbar^2}{2m^*}((\vec{K} + \vec{Q})^2 - \vec{K}^2)}. \quad (3.22)$$

The dielectric function related the unscreened potential with the screened one by

$$V^{ext}(\vec{Q}) = \epsilon(\vec{Q}) V^{eff}(\vec{Q}) \quad (3.23)$$

Comparing equation 3.21 with equation 3.23, one remarks that the dielectric function $\epsilon(\vec{Q})$ and the polarizability $\Pi(\vec{Q})$ of a system (here shown for a 3D system) are directly proportional. Its explicit relation, however depends on the dimensionality of the system, one is regarding [Bastard 88].

In this work, one is considering unmodulated and modulated Q2DEG, e.g. systems, which are quantized in the z - direction. Since there are discrete energy subbands in the system, the dielectric function is not simply a function of momentum³ as in bulk materials.

² \vec{Q} is the \vec{Q} -th Fourier component of the three dimensional space vector $\vec{R} = (R_x, R_y, R_z)$.

³In this work one concentrates only on the static dielectric function.

It also depends on the electron distribution in each of the subbands. Therefore the treatment of the dielectric function is more complicated. For simplicity, in literature it is often assumed that there is only one single subband occupied, even at high charge density or higher temperature [Hirakawa 86]. This leads to an underestimation of the screening, as will be shown later. In the RPA - approximation the dielectric tensor takes the form

$$\epsilon_{Q2D}(\vec{q}, r_z, r_{z'}) = \delta(r_z - r_{z'}) + \frac{e^2}{2\epsilon} \sum_{\alpha', \alpha} \frac{\Pi_{\alpha', \alpha}(\vec{q})}{q} [\xi_{\alpha}(r_{z'}) \xi_{\alpha'}(r_{z'})] \int dz'' \xi_{\alpha}(r_{z''}) \xi_{\alpha'}(r_{z''}) \exp(-q|r_z - r_{z''}|)$$

with the polarizability

$$\Pi_{\alpha', \alpha}(\vec{q}) = \frac{1}{S} \sum_{\alpha', k} \frac{g^0(E_{\alpha'}(\vec{k} + \vec{q}), E_F) - g^0(E_{\alpha}(\vec{k}), E_F)}{E_{\alpha'}(\vec{k} + \vec{q}, E_F) - E_{\alpha}(\vec{k}, E_F)}$$

At low charge density and low temperature, only the fundamental subband is occupied by electrons. The dielectric function can be reduced to a function of that subband only, e.g. $\epsilon(\vec{q})$ reduces to a scalar, without committing a big error. However, at higher temperature and / or greater charge density, the spatial extents and the occupations of higher lying subbands must be considered: The evaluation of the dielectric function is no longer straightforward. Theoretically, one has to sum over all subbands of the system, in practice one will keep a finite number N of subbands. Accordingly, one deals with a linear equation system, consisting of N^2 integrals. To obtain these last terms, one thus has to invert the dielectric matrix ($N^2 \times N^2$) for every vector q, leading to

$$< \xi_{\alpha'}(r_z) | V_{scatt.}^{eff}(\vec{q}, r_z) | \xi_{\alpha}(r_z) > = \sum_{\beta, \beta'} [\epsilon(\vec{q})]_{\alpha' \alpha, \beta' \beta}^{-1} < \xi_{\beta'}(r_z) | V_{scatt.}^{eff}(\vec{q}, r_z) | \xi_{\beta}(r_z) >$$

with

$$[\epsilon(\vec{q})]_{\alpha' \alpha, \beta' \beta} = \delta_{\alpha' \alpha, \beta' \beta} + \frac{e^2}{2\epsilon} \frac{\Pi_{\beta' \beta}(q)}{q} F_{\alpha' \alpha, \beta' \beta}(\vec{q})$$

where the form factor $F_{\alpha' \alpha, \beta' \beta}(\vec{q})$ is given by

$$F_{\alpha' \alpha, \beta' \beta}(\vec{q}) = \int dr_z dr_{z'} \xi_{\beta'}(r_{z'}) \xi_{\alpha'}(r_{z'}) \xi_{\beta}(r_z) \xi_{\alpha}(r_z) e^{-q|r_z - r_{z'}|}$$

The subband indices α, β denotes the initial subbands occupied by the two interacting electrons, and the indices α', β' denote the final subbands.

These are the matrix elements, which enter directly in the transition probability to calculate the scattering probability. It is important to note that in these calculations the scattering matrix element intervene linearly, in contrast to the case, where the dielectric function is taken as a scalar. Lee et al. [Lee 97] calculated the transition probabilities in the case of ionized impurity scattering. In this work, the influence of taking higher subbands in the dielectric function into account is investigated as a function of charge density as well as a function of temperature, using the above described formalism, for remote ionized impurity, alloy and acoustic phonon scattering. This is the reason why the calculations to obtain the linear scattering matrix elements for the different scattering potentials are presented in the following section.

3.7 Types of Interactions

In this section the interactions taken into account in this work shall be discussed in detail:

1. Coupling by local perturbations of the crystal (e.g. ionized impurities)
2. Coupling by non - local perturbation of the crystal (e.g. alloy scattering)
3. Electron - Phonon coupling (e.g. acoustic phonons)

In the following each interaction, one by one, shall be first explained for a non - modulated two - dimensional electron gas, before then special attention to the modifications for a modulated electron gas is paid. The discussion is important, since the transition probabilities cannot be written any longer as the quotient of the square of the unscreened transition probability and the square of the dielectric function, e.g. as $|V^{scatt.}(\vec{q})|^2/|\epsilon(\vec{q})|^2$ due to the previous discussion: one has to sum over all terms $\sim \langle V^{scatt.} \rangle \epsilon^{-1}$, before taking the square.

1. Coupling by local perturbations of the crystal

The Coulomb potential between an impurity of charge Z_i (positive or negative) at point $\vec{R}_i = (r_{z_i}, \vec{r}_i)$ and an electron with charge $-e$ at point $\vec{R} = (r_z, \vec{r})$ is given by

$$V_{imp}^{ext}(\vec{R}) = \frac{-e^2 Z_i}{4\pi \epsilon_0 \epsilon_r} \frac{1}{|\vec{R} - \vec{R}_i|} \quad (3.24)$$

$$= \frac{-e^2 Z_i}{4\pi\epsilon_0\epsilon_r S} \sum_{\vec{q}(2D)} \frac{2\pi}{q} e^{-q|r_z-r_{z_i}|} e^{-i\vec{q}(\vec{r}-\vec{r}_i)} \quad (3.25)$$

where the last equation results from the two - dimensional Fourier expansion of the Coulomb potential. Writing the wave - functions of the 2 DEG as

$$\Psi_\alpha(\vec{R}) = \frac{1}{\sqrt{A}} \xi_\alpha(r_z) e^{i\vec{k}\vec{r}}, \quad (3.26)$$

and summing over all impurities (having the same charge Z), the matrix element for the (unscreened) potential $V^{ext}(\vec{R})$ is given by

$$\langle \alpha' \vec{k}' | V_{imp}^{ext}(\vec{R}) | \alpha \vec{k} \rangle = \sum_i \frac{-e^2 Z_i}{4\pi\epsilon S} \sum_{\vec{q}} \delta(\vec{k}' - \vec{k} - \vec{q}) e^{i\vec{q}\vec{r}_i} \frac{F_{\alpha'\alpha}(\vec{q}, r_{z_i})}{q} \quad (3.27)$$

with the form factor

$$F_{\alpha'\alpha}(\vec{q}, r_{z_i}) = \int dr_z \psi_{\alpha'}(r_z) \psi_\alpha(r_z) e^{-|\vec{q}||r_z-r_{z_i}|} \quad (3.28)$$

The screened matrix element can be written formally in the same form:

$$\langle \alpha' \vec{k}' | V_{imp}^{eff}(\vec{R}) | \alpha \vec{k} \rangle = \sum_i \frac{-e^2 Z_i}{4\pi\epsilon S} \sum_{\vec{q}} \delta(\vec{k}' - \vec{k} - \vec{q}) e^{i\vec{q}\vec{r}_i} \frac{F_{\alpha'\alpha}^{eff}(\vec{q}, r_{z_i})}{q} \quad (3.29)$$

with the (effective) form factor⁴

$$F_{\alpha'\alpha}^{eff}(\vec{q}, z_i) = \sum_{\beta'\beta} \epsilon_{\alpha'\alpha}^{-1}{}_{\beta'\beta}(\vec{q}) F_{\beta'\beta}(\vec{q}, z_i). \quad (3.30)$$

Neglecting all correlations between impurities and replacing the sum over i by an integral over the volume density of impurities⁵ $N(r_{z_i})$, the transition probability for the interaction between the remote ionized impurity doping in the barrier and an electron in state $|\alpha, \vec{k}\rangle$ becomes:

$$| \langle \alpha' \vec{k}' | V_{imp_{barrier}}^{eff} | \alpha \vec{k} \rangle |^2 = \left[\frac{e^2 Z}{2S\epsilon} \right]^2 \int dr_{z_i} N(z_i) \left[\frac{F_{\alpha'\alpha}^{eff}(\vec{q}, r_{z_i})}{q} \right]^2, \quad (3.31)$$

⁴If one neglects the intersubband transitions, the effective form factor becomes: $F_{\alpha'\alpha}^{eff}(\vec{q}, r_{z_i}) = \frac{F_{\alpha'\alpha}(\vec{q}, r_{z_i})}{\epsilon_{\alpha'\alpha}(\vec{q})}$

⁵ $SN(r_{z_i})$ is the density per unity of the spacer.

The homogeneous background doping is parameterized by the (three - dimensional) impurity density N_{B_i} ($i = 1, 2$): N_{B_1} for the $\text{Al}_x\text{Ga}_{1-x}\text{As}$ and N_{B_2} for the background doping of the GaAs. Hence, the potential is written

$$| \langle \alpha' \vec{k}' | V_{imp_{bar}}^{eff} | \alpha \vec{k} \rangle |^2 = \left[\frac{e^2 Z}{2S\epsilon} \right]^2 \int dr_{z_i} N_{B_{1,2}}(r_{z_i}) \left[\frac{F_{\alpha'\alpha}^{eff}(\vec{q}, r_{z_i})}{q} \right]^2. \quad (3.32)$$

2. Coupling by non - local perturbation of the crystal

In the $\text{Al}_x\text{Ga}_{1-x}\text{As}$ alloy, the Arsenic atoms occupy the sites of one of the face - centered cubic lattice of the zinc - blende crystal (e.g. they form the anionic sub - lattice). The other kind of atoms (Ga and Al) are randomly distributed on the sites of the second face - centered cubic lattice. Thus, although the underlying potential is periodic, the crystal potential is actually not. Hence, in principle, one can not define bloch waves, dispersion relations, etc. The simplest way to overcome this difficulty is to use the virtual crystal approximation [Brum 85]. In this approximation, the unscreened scattering potential is written as

$$| \langle \alpha' \vec{k}' | V_{all}^{ext}(\vec{r}) | \alpha \vec{k} \rangle |^2 = \frac{\Omega_0}{S} x(1-x) [\delta V]^2 \int_L dz [\xi_\alpha(r_z)] [\xi_{\alpha'}(r_z)]^2, \quad (3.33)$$

where Ω_0 is the volume of the unit cell and x the mean Aluminum content of the considered structure. The screened transition probability takes the form

$$| \langle \alpha' \vec{k}' | V_{all}^{eff}(\vec{r}) | \alpha \vec{k} \rangle |^2 = \frac{\Omega_0}{S} x(1-x) [\delta V]^2 \int_L dr_z \left[\sum_{\beta\beta'} \epsilon_{\alpha'\alpha\beta'\beta} [\xi_{\beta'}(r_z)] [\xi_\beta(r_z)] \right]^2 \quad (3.34)$$

As expected, equation 3.33 is \vec{q} - independent, reflecting the short range nature of the alloy scattering potential. However, equation 3.34 is \vec{q} - dependent, which is due to the \vec{q} - dependent dielectric function.

3. Electron - Phonon coupling

Under a thermic agitation, the atoms of the lattice can have two types of vibrations, which correspond to two types of branches (acoustic and optic) in the dispersion relation. If the atoms vibrate in phase, one is dealing with the acoustic branch, which has a linear dispersion relation at the center of the Brillouin zone. In opposite, if the atoms move in opposite phase, one is dealing with the optical branch, characterized by a constant energy $\hbar\omega_0$ in the vicinity of the Brillouin zone center. Each of the two branches has three different modes, one longitudinal and two transversal modes. Accordingly, one needs a certain energy, provided by the temperature of the crystal to excite optical phonons. In this work, one is only interested in a temperature range up to 70K. This allows to neglect the optical phonons, which become dominant at higher temperatures [Hirakawa 86].

The propagation of a phonon disturbs the perfect periodicity of the crystal which is required to establish Bloch functions, energy dispersions, etc.. These phonon perturbations) can influence the electron motion in two different ways:

- (a) Short range perturbations of the crystal potential are described by a deformation potential and hence the electron - phonon interaction is called coupling by deformation potential. They are found in every solid.
- (b) Equally, the lattice deformation can perturb the local electrical neutrality of the lattice. Consequently, an electric field is produced, which will influence the electron motion. This is a coulomb type of perturbation and thus of long range. These phonon- electron interaction are called coupling by the piezoelectric potential. They exist only in polar materials, like in GaAs, e.g. in materials which have a lack of inversion symmetry.

An approximation often used but not justified rigorously assumes the energy of the phonons to be small, so that the scattering can be considered elastic.

In order to discuss the electron - phonon interaction, one needs to resort to quantum theory of the harmonic oscillator.

The lattice vibrations represent coupled oscillators and the displacement \vec{u} , representing the deformation of the unit cell or the two atoms in the unit cell, must be represented in "normal" coordinates, where

the different modes are uncoupled. In first order perturbation theory, the electronic energy perturbation is related linearly to the strain in the crystal $\nabla \mathbf{u}$ and is given by

$$V_{def}^{ext}(\vec{R}) = \Xi \frac{\partial \vec{u}}{\partial \vec{R}} \quad (3.35)$$

where Ξ is the deformation potential for the particular valley of interest.⁶ Expressing the displacement \vec{u} in normal coordinates $\vec{v}_{\vec{Q}}$, equation 3.35 becomes:

$$V_{def}^{ext}(\vec{R}) = \Xi \sum_{\vec{Q}(3D)} \frac{i\vec{b}_{\vec{Q}}\vec{v}_{\vec{Q}}}{\sqrt{N}} e^{i\vec{Q}\vec{R}} + \text{complex conj.}, \quad (3.36)$$

where N is the number of unit cells in the periodic crystal and $\vec{b}_{\vec{Q}}$ the polarization vector. The normal coordinate displacement can be written in terms of the phonon creation and destruction operators a^+ and a :

$$V_{def}^{ext} = \Xi \sum_{\vec{Q}} \left[\frac{\hbar}{2NM\omega_{\vec{Q}}} \right]^{\frac{1}{2}} i\vec{Q} (a_{\vec{Q}} + a_{-\vec{Q}}^+) e^{i\vec{Q}\vec{R}}, \quad (3.37)$$

where M is the mass of the oscillator, e.g. the total mass of the unit cell and $\omega_{\vec{Q}}$ corresponds to the angular frequency of the mode with wavevector \vec{Q} . This leads to the following matrix element:

$$\begin{aligned} \langle \alpha' \vec{k}' | V_{dp}(\vec{R}) | \alpha \vec{k} \rangle &= \Xi \sum_{\vec{q}_z} \sum_{\vec{q}(2D)} \left[\frac{\hbar}{2NM\omega_{\vec{Q}}} \right]^{\frac{1}{2}} i\vec{Q} (a_{\vec{Q}} + a_{-\vec{Q}}^+) e^{i\vec{q}\vec{r}} \\ &\quad F_{\alpha'\alpha}(\vec{q}_z) \delta(\vec{k}' - \vec{k} - \vec{q}) \end{aligned} \quad (3.38)$$

with $F_{\alpha',\alpha}(\vec{q}_z) = [f dz [\xi_{\alpha'}(z)] [\xi_{\alpha}(z)] e^{i\vec{q}_z z}]$

For the screened (= effective) potential, one has formally the same expression by replacing $F_{\alpha',\alpha}(\vec{q}_z)$ with $F_{\alpha',\alpha}^{eff}(\vec{q}_z)$:

$$F_{\alpha',\alpha}^{eff}(\vec{q}_z, \vec{q}) = \sum_{\beta, \beta'} \epsilon_{\alpha, \alpha', \beta, \beta'}^{-1}(\vec{q}) F_{\beta', \beta}(\vec{q}_z) \quad (3.39)$$

Having the equation

$$(a_{\vec{Q}} + a_{-\vec{Q}}^+) |n_{\vec{Q}}, n_{-\vec{Q}}\rangle = \sqrt{n_{\vec{Q}}} |n_{\vec{Q}}-1, n_{-\vec{Q}}\rangle + \sqrt{n_{-\vec{Q}}+1} |n_{\vec{Q}}, n_{-\vec{Q}}+1\rangle, \quad (3.40)$$

⁶The acoustic phonons are taken three dimensional in this work.

where $n_{\vec{Q}}$ denotes the number of phonons in the mode $\omega_{\vec{Q}}$. for the phonon operators, one obtains for the transition probability between state $|\alpha, \vec{k} >$ and $|\alpha', \vec{k}' >$, neglecting again any kind of correlations,

$$| < \alpha' \vec{k}' | V_{def}^{ext}(\vec{R}) | \alpha \vec{k} > |^2 = \frac{2\pi}{\hbar} [\frac{\hbar}{2NM}] \Xi^2 \sum_{\vec{q}_z} \sum_{\vec{q}} [\frac{\vec{Q}^2}{\omega_{\vec{Q}}}] |F_{\alpha'\alpha}^{eff}(\vec{q}_z, \vec{k}' - \vec{k})|^2 \cdot \\ \delta(\vec{k}' - \vec{k} - \vec{q}) \{ n_{\vec{Q}} \delta(E_{\vec{k}'} - E_{\vec{k}} - |\hbar\omega_{\vec{Q}}|) + n_{-\vec{Q}} + 1 \} \delta(E_{\vec{k}'} - E_{\vec{k}} - |\hbar\omega_{\vec{Q}}|) \}$$

Taking the scattering process elastic, means that one neglects the differences on energy. Beyond, one also neglects 1 with respect to $n_{\vec{Q}}$ in the phonon population. Given $\omega_{\vec{Q}} = v_s * \vec{Q}$ and $n_{\vec{Q}}$

$$| < \alpha' \vec{k}' | V_{def}^{eff}(\vec{R}) | \alpha \vec{k} > |^2 = \frac{2\pi}{\hbar N} \frac{\Xi^2}{M v_s} \sum_{q_z} \sum_{\vec{q}} n_{\vec{Q}} \hbar \omega_{\vec{Q}} |F_{\alpha'\alpha}^{eff}(\vec{q}_z, \vec{k}' - \vec{k})|^2 \\ \delta(\vec{k}' - \vec{k} - \vec{q}) \quad (3.41)$$

Beyond, one approximates $n_{\vec{Q}} \hbar \omega_{\vec{Q}} \sim k_B T$, which is valid, if $k_B T \ll \hbar \omega_{\vec{Q}}$. Using the relations $SL_z = \Omega_0$ (volume of the unit cell) $M/\Omega_0 = \rho$ (volumic mass) and $\rho v_s^2 = c_L$ (elastic constant, v_s the sound velocity), one finally obtains for the transition probability:

$$| < \alpha' \vec{k}' | V_{def}^{eff}(\vec{R}) | \alpha \vec{k} > |^2 = \frac{L_z \Xi^2}{NM v_s} \int_{-\infty}^{\infty} dq_z |F_{\alpha'\alpha}^{eff}(\vec{q}_z, \vec{k}' - \vec{k})|^2, \quad (3.42)$$

where L_z is the length of the channel. As the alloy scattering potential, the deformation potential scatters isotropic in the $r_{||}$ - , r_{\perp} - plane. This interaction potential is in the experimentally considered temperature range ($T = 0 - 70$ K) negligible. This is the reason, why this scattering potential will not be explained in detail when discussing the results. Nevertheless, it has been included in the numerical calculations.

2D Modulated Electron Gas Instead of having the plane wave functions $\Psi_{\alpha}(r_{||}, r_{\perp}, r_z) = \frac{1}{\sqrt{A}} \xi_{\alpha}(r_z) e^{i(k_{||} r_{||} + k_{\perp} r_{\perp})}$, it shall be recalled that one now has wave functions of the form

$$\Psi_{\alpha}(r_{||}, r_{\perp}, r_z) = \frac{1}{\sqrt{A}} e^{i(k_{||} r_{||} + k_{\perp} r_{\perp})} \sum_{\alpha} \xi_{\alpha}(r_z) \sum_{p \in Z} a_{p(\alpha)}(\vec{k}_{\perp}) e^{ip \frac{2\pi}{L_{\perp}}} \quad (3.43)$$

As discussed in section 2.2.3, the intersubband - coupling is negligible in the untilted zone of the wafer (the splitting between two subbands is of the order

of 0.05 meV. and hence only the projection on a single subband, the most important for a given state, is kept). Thus the lateral subband-index α is dropped for readability: $a_p = a_{p(\alpha)}$. \vec{k}_\perp lies in the first Brillouin zone and $a_p(\vec{k}_\perp)$ is the coefficient of the modulated function's in plane variation on the plane wave $\frac{1}{\sqrt{A}}\xi_\alpha(r_z)e^{i(k_\parallel r_\parallel + k_\perp r_\perp)}e^{ip\frac{2\pi}{L_\perp}}$. ξ_α are the wave functions corresponding to the electrical subband of the same structure, but laterally unmodulated.

Taking these wavefunctions and calculating the transition probability for a general (unscreened) scattering potential $V^{scatt.}(\vec{R})$ ($V^{scatt.}(\vec{q}, r_z)$ is the 2D in - plane Fourier transform of the scattering potential), one obtains:

$$| \langle \alpha' \vec{k}' | V^{scatt.}(\vec{R}) | \alpha \vec{k} \rangle |^2 = \sum_{q,p,m} [\langle V^{scatt.}(\vec{q}, z) \rangle_{\xi(r_z)} \cdot a_p(\vec{k}_\perp) a_{p+m}(\vec{k}'_\perp)] \delta(\vec{k}'_\parallel - \vec{k}_\parallel - \vec{q}_\parallel) \delta(\vec{k}'_\perp - \vec{k}_\perp - \vec{q}_\perp + m * \frac{2\pi}{L_\perp}) \quad (3.44)$$

Some general remarks on this equation:

- $\langle V^{scatt.}(\vec{q}, r_z) \rangle_{\xi(r_z)}$ is the scattering potential, averaged over the r_z - direction.
- The δ - function reflects the momentum conversation in the r_\parallel - direction and the quasi - momentum conversation in the r_\perp - direction. Thus, the magnitude of the diffusion vector q_m assumes the following form:

$$q_m = \sqrt{(\vec{k}'_\parallel - \vec{k}_\parallel)^2 + (\vec{k}'_\perp - \vec{k}_\perp + m * \frac{2\pi}{L_\perp})^2} \quad (3.45)$$

with $m = 0$ describing a "direct" process, with $m \neq 0$ an "umklapp" process.

- The wavefunction amplitudes $a_p(k_\perp)$ are determined from the self - consistent band structure calculation. Without modulation, the only non - zero amplitude is the one corresponding to the miniband index. With modulation, the Fourier component $V^{(p)}$ ($= V^{(-p)}$) couples states of same wave vector and belonging to minibands with index differing by $\pm p$: as an example, miniband (-1) is coupled to the lower miniband (0) by $V^{(1)}$ and to the upper miniband (+1) by $V^{(2)}$. Hence, this results in additional non - zero coefficient $a_0(k_\perp)$ and $a_1(k_\perp)$ to $a_{-1}(k_\perp)$. Naturally, a given process is only relevant (e.g. the transition probability

is different from 0), when the product $[a_p(\vec{k}_\perp)a_{p+m}(\vec{k}_\perp)]$, summed over p , is not zero. This proves that due to the lateral potential modulation additional scattering processes become possible. How they intervene in the transversal resistivity, will be discussed in chapter 5.

Chapter 4

Technological Processing of a Lateral Superlattice

From a theoretical point of view, one "introduces" a lateral potential modulation. From a practical point of view the question arises, how can one actually succeed in realizing a lateral potential modulation? In order to resolve the miniband structure of a lateral potential modulation, it is necessary (i) to reduce the periodicity of the lateral potential to length scales comparable to the Fermi wavelength of the electrons (~ 40 nm in GaAs heterojunctions), (ii) to impose a sufficiently strong potential modulation and (iii) to achieve a sufficiently high mobility modulated 2DEG such that broadening due to impurities and inhomogeneities does not obscure the minibands. One approach to meet these conditions seems to be provided by the growth of lateral superlattices on vicinal surfaces. The original idea steams from P. Petroff [Petroff 84]. The idea consists of the deposition of fractional monolayers $(\text{GaAs})_m(\text{AlAs})_n$ with $p = m + n \sim 1$ in a monolayer by monolayer growth on vicinal surfaces.

It was four years later that the first successful growth of lateral superlattices could be reported by transmission electron microscope micro-graphs [Gaines 88]. The substrates which are used were GaAs substrates deliberately misoriented with a surface normal oriented 2° from $[001]$ toward $[110]$. The average Al - composition is 50 %. These results are little later reproduced by Hirokoshi's group [Yamaguchi 89]. It becomes clear by regarding the TEM micrographs that the tilt of the lateral superlattices depends strongly on the coverage ratio p . Indeed, if the lateral superlattice coverage (GaAs and AlAs) differ from one by ϵ then the lateral superlattice is tilted with the tilt angle $\beta = \arctan(\epsilon/\alpha)$ where α is the misorientation angle of the vicinal surface.

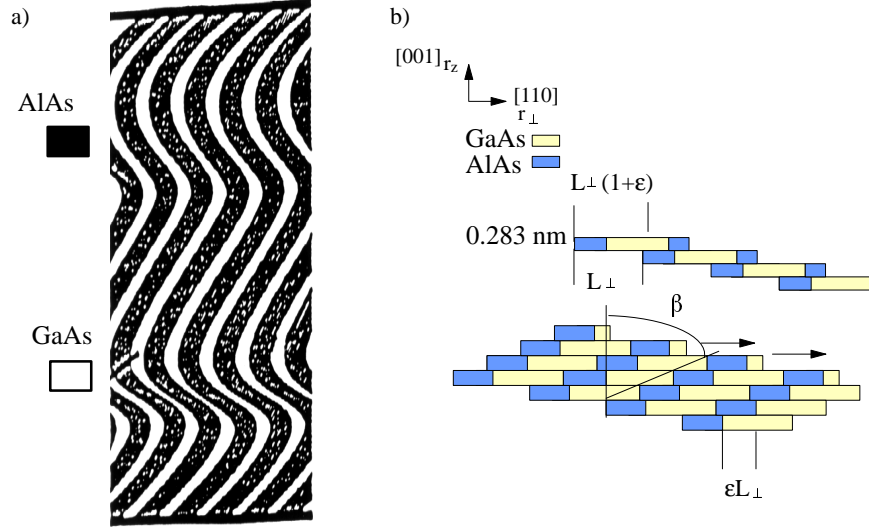


Figure 4.1: *Sketch of a serpentine superlattice (a) and a tilted lateral superlattice (b). a): An intentional change of the per - cycle coverage during growth leads to serpentine superlattices [Miller 85]. b): The substrate is not turned during growth. Due to a lateral flux gradient, there are zones on the sample, where the lateral superlattice is tilted and other where not.*

To circumvent this difficulty, Miller et al. [Miller 91][Miller 92] proposed an original structure: the serpentine superlattices (see Fig. 4.1.a). The idee consists of sweeping intentionally the per - cycle coverage during growth through a range including that needed for a vertical (untilted) structure. Additionally, the sample was rotated (one rotation per monolayer) to avoid any lateral flux gradient. The disadvantage of these structures is that the width of the lateral superlattice (in growth direction) is very small.

Another approach to succeed in non - tilted lateral superlattice was proposed by F. Laruelle [Laruelle 97]: The substrate is **not** turned during growth. Due to the lateral flux gradient, one thus has zones, where the lateral superlattice is tilted and zones, where the lateral superlattice is vertical. Moreover, F. Laruelle could show that the relevant parameter is not the tilt angle β but the product $N\epsilon$ (N is the number of lateral superlattice monolayers) as far as electronic properties are concerned [Laruelle 97](Fig. 4.1.b). It is the latter approach which is chosen in this work.

The optical properties of these tilted and untilted superlattices were analyzed in a systematic study as a function of the lateral periodicity by Bloch [Bloch 94]. She could demonstrate that pronounced features due to the lateral potential modulation are exhibited in the polarization spectra, when taking a periodicity of 32 nm. These structures in the polarization spectra diminish when diminishing the period of the lateral potential modulation, e.g. taking vicinal surfaces with smaller terrace length. This is due to the stronger coupling of the quantum wires. By this experiments, e.g. the strength of the features depends on the terrace length, it is equally demonstrated that the observed features are due to the formation of a lateral superlattice and not, for example, due to anisotropic ALAs island formations.

In this section the idea of the structure and fabrication of lateral superlattices on vicinal surfaces shall be developed in more detail: first the grown structures are discussed, next the growth conditions are explained and finally, the way, how the structures are processed, is described. It shall be emphasized that the achievement of low disordered lateral superlattices is in praxis quite difficult. The difficulties are mainly due to the great number of critical parameters during preparation of the substrate and growth (quality of the substrate, purity of the products, used for the chemical etching, purity of the water, precision of the indication of the temperature during growth, purity of the cells, ...) which are not always well known.

4.1 Doped Lateral Superlattices

Fig. 4.2 shows a typical structure of a doped lateral superlattice: One starts

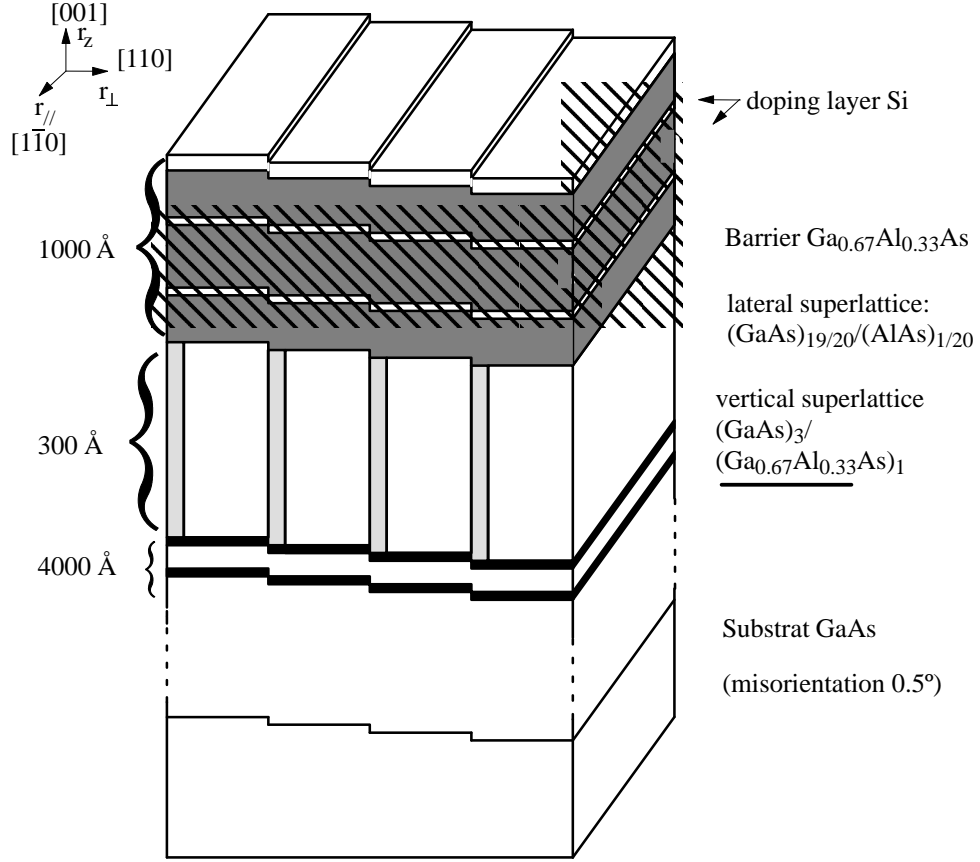


Figure 4.2: *A typical structure of the samples studied in this work. The lateral superlattice is embedded in the heterostructure.*

with a vicinal surface substrate on which one grows $\sim 1\mu\text{m}$ GaAs. The purpose of this layer (called "buffer") is to smooth the surface. Next, one grows a vertical superlattice which has a double function:

- It serves as a barrier for the electrons which will be confined in the lateral superlattices.
- It purges the impurities, improving thus the quality of the heterostructure.

A channel of typical 30 nm is grown in which the lateral superlattice is embedded (with an averaged Aluminium content between $x_{Al} = 5\%$ and 7%).

It follows the barrier (averaged Aluminium content typically $x_{Al} = 33\%$) with two planes of Silicon doping. The first plane assures the charge transfer in the heterostructure, the second plane satisfies surface states. The spacer, which is the distance between the heterostructure and the first plane of Silicon varies between 9 and 20 nm, according to the desired charge transfer. To hinder the oxidation of the sample, one finishes the growth by passivating the sample with 10 nm GaAs.

How these structures are obtained technologically, shall be described in the next paragraphs.

4.2 Growth Conditions

Substrate Choice Substrates for the lateral superlattices growth were semi - insulating GaAs wafers grown by the liquid encapsulated Czochralski technique obtained by Sumitomo. In all the structures studied here the misorientation angle is 0.5° , corresponding to a terrace length $L = 32$ nm. This terrace length was proven to be the best [Bloch 94]: Shorter periods enhance the coupling in the lateral superlattices and thus leading to an effective smaller potential modulation. Larger lateral terraces have for consequence a greater disorder, since a great part of the atoms stick to the surface before reaching the step-border, e.g. the averages diffusion length is smaller than a terrace length for the temperature range chosen in this work [Lelarge 96]. (The reason for the chosen temperature is given later.)

Substrate Preparation The best vicinal surface quality and luminescence and electronic results were obtained when the substrate was treated by a chemical attack just prior to loading into MBE. This substrate preparation consists of a degreasing procedure (two trichlorethylene and two isopropanol bath), an etch in an 4:1:1: solution of $\text{H}_2\text{SO}_4:\text{H}_2\text{O}_2:\text{H}_2\text{O}$ for 80 s., followed by a thorough rinse in deionized water. This substrate preparation proved to be a critical and very important step in the successful fabrication of lateral superlattices. The highest possible purity of each ingredient is absolutely necessary. An empirical method to estimate the quality of the substrate after the chemical attack is the time between the start of the growth on the substrate and the appearance of the splitting (see RHEED -measurements!).

Desoxidation The MBE chamber is equipped with an introduction chamber and three ultrahigh vacuum chambers (introduction, analyse and transfer chamber) and one growth chamber. The substrate are attached with Indium on a molybden sample holder which has been degassed approximately 12 hours at 700°C in the introduction module before.

Substrate and sample are deoxidized in the analyse module at 500°C for ca. 12 hours just before the growth will take place. The purpose of this procedure is avoiding the desoxidation of the sample in the growth chamber in order to keep the evaporation cells as pure as possible. Nevertheless, the sample will be heated 5 minutes at 650°C under As pressure in the growth chamber, so that impurities have segregated on the surface will evaporate.

RHEED - Monitoring Growth conditions are very critical and have thus to be controlled in situ. A powerful technique is the in situ RHEED - technique [Larsen 87]. RHEED (Reflection high energy electron diffraction) is a very surface - sensitive technique where most of the scattered electron intensity is reflected from just the top couple of monolayers. Thus it gives insight in the surface morphology of the substrate as well as it reflects the growth mechanism responsible for heterostructures and LSL quality.

Surface morphology of a lateral superlattice

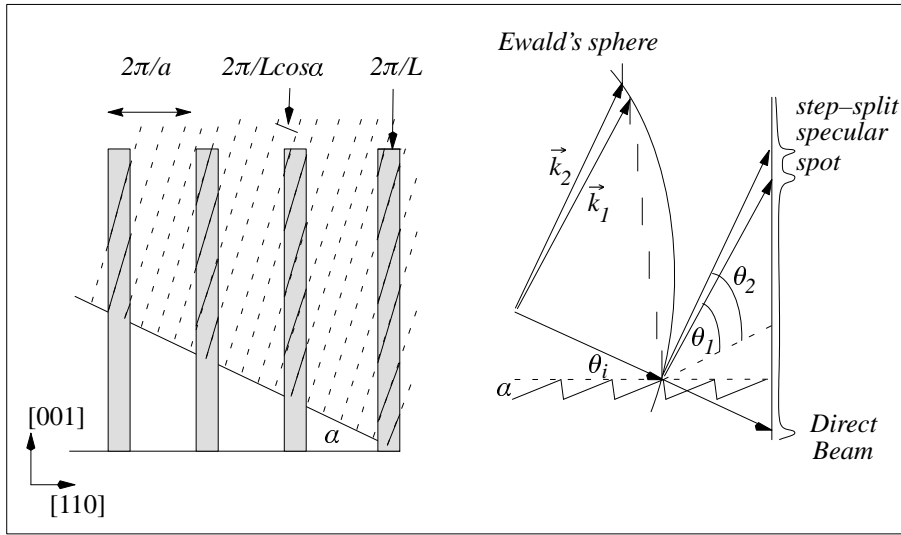


Figure 4.3: *Left: Reciprocal lattice construction of a vicinal surface. Right: The geometry for monitoring the surface of a vicinal surface is shown [Chalmers 89]. The electron beam is incident from the left and scattered electrons impinge on the RHEED screen on the right. An intensity profile along the central streak is equally sketched: Due to the vicinal surface, the specular beam is split.*

A vicinal surface can be viewed as the convolution of a single terrace of atoms and a periodic lattice of points, where each point represents a terrace location [Henzler 74]. Therefore, the reciprocal lattice of the vicinal surface can be derived as the intersection of the reciprocal lattice rods of a single terrace with the reciprocal lattice planes of the periodic step lattices. When the incident beam satisfies a Bragg condition, all reflected electrons are in phase and form a sharp peak. In an out of phase condition the interference

from different terraces results in a splitting of the beam into two separate peaks. The angular separation of the two peaks is determined by the terrace width [Pukite 84]. If the terrace widths are nonuniform, they will lead to broadening of the individual peaks. Hence, the peak widths and their separation give an indication of the step distribution on the surface. Equally, the time between the start of the growth and the appearance of this splitting allows to draw conclusions on the surface quality after the chemical etching. (The splitting can only appear, if the surface is sufficiently smooth that the periodicity due to the terraces can form a lattice!) Moreover, the steady observation of these spots allows to improve or adjust adequately the growth conditions in situ. However, having a well defined splitting of the specular spot all along the growth is only a necessary condition to obtain a lateral superlattice with good optical and electronic properties, unfortunately, it is not a sufficient one!

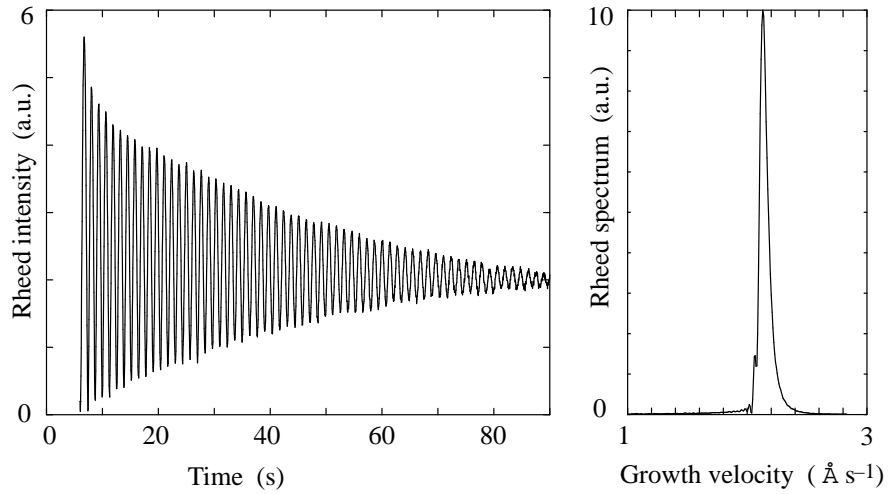


Figure 4.4: *Typical Rheed oscillations (left) and its Fourier transformed (right). The growth rate is in this case 0.22 nm/s.*

Atomic Flux calibrations Before the growth, it is important to know with high precision the growth rate of each material. The measuring of the growth rate (e.g. atomic flux calibration) is also done by Rheed measurements, or more precisely by measuring the associated frequency of the intensity oscillations of the specular spot of the RHEED (see Fig. 4.4).

The oscillations transmit the variation of the surface roughness during growth. The Ga - atoms, which hit the surface, react with the Arsenic by forming islands. Hence, the surface roughness increases and will increase while the distance between the islands remain greater than the Ga diffusion length. The change of the surface roughness causes a change in the surface reflectivity, e.g. the specular spot intensity diminishes. In contrast, when the distance between the island becomes smaller than the diffusion length of the Ga - atoms, the adatoms incorporate themselves preferably at the islands' boundary and the intensity of the specular spot increases again. Once a monolayer is completed, the majority of the island has disappeared and the surface becomes smooth again. Accordingly, the periode of the oscillations correspond exactly to one monolayer. By this method one is able to calibrate the flux of the elements of group III with the precision of 1 %.

The RHEED - oscillations are measured on a nominal substrat GaAs (2*2 mm) heated to a temperature of 560°C. Nominal Ga-flux is typically set to a continous growth rate of 0.05 nm/s, the Al-flux to 0.025 nm/s for the MEE regime (see below) and to 0.2 nm/s (Ga-flux) (0.1 nm/s Al - flux) for the MBE -regime.

Growth Conditions The decisive fact for the achievement of a low disordered lateral superlattice, is that the adatoms, once deposited on the surface will migrate to the steps to get incorporated there. Only then a lateral regular ordered and low disordered superlattice can be realized. The physical quantity which describes the possibility for an adatom to wander around is the migration length. This length will depend on the substrate temperature, the purity of the substrat (because if the surface has a low impurity amount, the interaction probability of the adatoms is diminished) and the arsenic pressure. Practically one has to find a compromise between these physical quantities. It was found in the MEE - method ("Migration enhances Method") proposed 1986 by Horikoshi [Horikoshi 86]: It consists in interrupting the As - flux while depositing the elements of group III in order to improve the surface mobility of the adatoms. Naturally, one has to stay below the critical temperature T_{cs} above which the surface reconstruction changes from (2×4) to (4×2) , transiting from an As - rich surface to a Ga - rich surface. The optimal growth temperature was demonstrated to be 580 °C [Horikoshi 86](and also taken for all samples grown in this work). Beyond, one deposits the Ga by quarter - monolayer. Between the depositions, the growth is stopped, keeping a low As - flux.

By this growth cycle one assures that the surface remains stabilized on

As (e.g. no Ga - islands can be formed, which is detrimental for the optical and electronic properties of the structure.)

4.3 Sample Fabrication

To obtain well defined lateral superlattices, besides the high stability of the materials flux, another prerequisite is necessary: The individual layers must be stacked exactly on top of each other. This prerequisite is only fulfilled for a small zone on the grown sample due to the flux gradient of the MBE chamber's cells. In this work it is the Ga - flux (the lateral superlattice consists to 95% of GaAs), which is dominant, leading to Ga - rich and Ga - low zones, e.g. to zones, where the lateral superlattice is tilted. The consequence of the tilt is basically a reduction of the lateral potential modulation (discussed in 2.2.3). One thus needs a method to find the zone of maximal potential modulation, e.g. the zone $p = 1$. How this zone is experimentally found, shall be briefly described next.

4.3.1 Experimental Detection of the zone $p = 1$

The zone $p = 1$ corresponds to the zone where the lateral superlattice is not tilted (see also end of section 2.2.3). Hence, the lateral potential modulation is maximal, resulting in a maximal spectral shift at the center of the first miniband, which can be detected by photoluminescence measurements. One "scans" the sample in a distance of $\Delta z = 500 \mu\text{m}$, and can thus exactly identify the zone of maximal potential modulation. The maximum of the energetical shift is accompanied by a maximum in the corresponding linear polarization value $P_{rate} = \frac{I_{\perp} - I_{\parallel}}{I_{\perp} + I_{\parallel}}$, where I_{\perp} (I_{\parallel}) corresponds to an absorbed light polarized perpendicularly (respectively parallelly) to the step edges [Bloch 94]. In praxis, one takes photoluminescence spectra and linear polarization spectra simultaneously. This allows a cross - check to be sure about the zone of maximal lateral potential modulation. In Fig. 4.5 a typical photoluminescence and polarization spectrum is shown, once for the untilted ($p = 1$) and once for the tilted zone. Taking these spectres over the whole sample allows to determine the zone $p = 1$, which then will be processed for transport measurements.

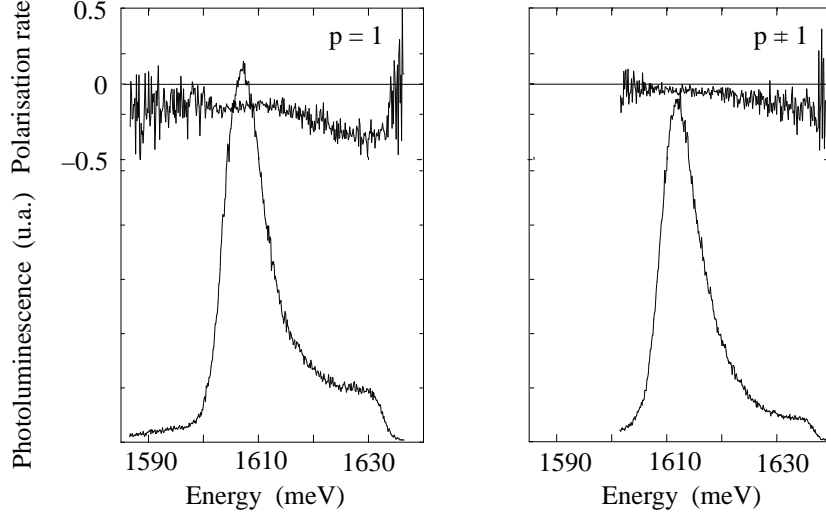


Figure 4.5: *Photoluminescence and corresponding linear polarization spectrum for the zone $p = 1$ (left) and $p \neq 1$ (right). As the potential modulation increases, the absolute value of the polarization rate P_{rate} increases and gets more structured. The maximum of the PL spectrum is at lower energy (here 1608 meV with respect to 1612 meV in the tilted zone) due to the spectral shift at the center of the first miniband at the Brillouin zone center, allowing to detect the zone $p = 1$.*

4.3.2 Sample Processing

The process to fabricate Hall bars seems to be quite standard. However, for the first time ohmic contacts (AuGe/Ni/AuGe) as well as non - leaking gates were successfully realized on these structures. This is the reason, why the "working recipes" shall be briefly documented.

1. Choice of the sample layout:

To measure the resistance corresponding to the perpendicular and parallel direction with respect to the lateral superlattice, the sample layout shown in Fig. 4.6 is used. The advantage of such a sample layout is that one measures the resistance corresponding to the perpendicular and parallel direction with respect to the lateral superlattice is measured at exactly the same place. The sample is patterned by UV - lithography.

2. Ohmic Contacts

To find the "recipe" to realize ohmic contacts, a modified TLM -

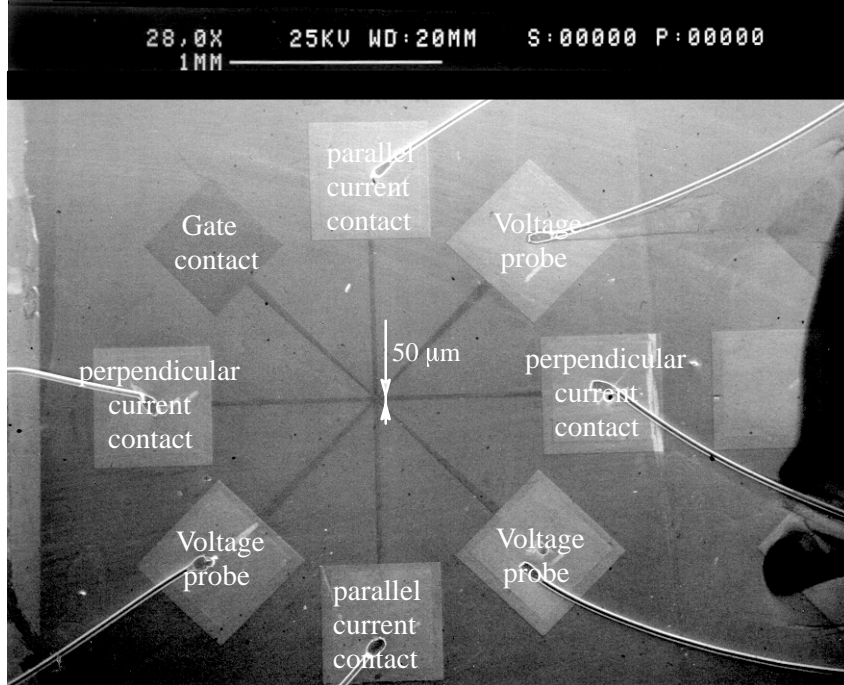


Figure 4.6: *Sample layout used for transport measurements: The central zone is $50 \times 50 \mu m^2$.*

method [Heiblum 82][Pardo 00] was applied. The best parameters were to be found: 5 nm Ni/34 nm Ge/68 nm Au/15 nm Ni/15 nm Ge/30 nm Au which were alloyed by the following manner: 5 min. at 110° , 2 min. at 360° and 40 s. at 430° .

3. Realization of a gate

(a) Change of the growth condition

To change the Fermi energy, and hence the electron density, one needs to be able to apply an electric field between the metal on top of the sample (= gate) and the electron gas. This will only work, if no current passes between the gate and the two dimensional electron gas. Up to now this was one of the technical problems to overcome in order to get more insight into the physics of modulated electron systems.

Kim and al. [Kim 96] showed that even thick ternary alloy (300 nm $Al_{0.33}Ga_{0.7}As$) barrier between gate and 2DEG do not prevent a current leakage due to microscopic structural inhomogeneities.

The idea is that by using (even thick) ternary alloy, there will always be zones rich on Ga, which allow the current to find a "way" between gate and 2DEG.

To overcome this problem, it is essential to use a digital alloy barrier (we find that 100 nm composed of 2 monolayer AlAs / 4 monolayer GaAs is enough to hinder any leakage current). The idea is that alternating the deposition of AlAs/GaAs prevents Ga rich zones.

Another crucial point is the reduction of the growth temperature (typically from 580° to 540°) after the first plane of the doping to avoid the diffusion of Si towards the surface.

(b) Deposition of the gate

The gate was deposited in two steps: first, 5 nm Ti is deposited. Since Titanium is semitransparent, one has the additional possibility to perform optically measurement. To avoid the non - functionality of the gate due to (unintended) charges, in a second step a Ti/Au (20 / 200 nm) with holes were deposited (see also Fig. 4.6).

Once having the sample grown, optically characterized and processed, the sample can now be investigated by transport measurements.

Before presenting the experimental results obtained in this work, the numerical results shall be discussed. The next chapter starts with the discussion of the results obtained for unmodulated 2DEG's and is followed by the one obtained for modulated 2DEG's.

Chapter 5

Numerical Results

In this chapter numerical results obtained during this work are presented. In the first section, the effect of including higher subbands in the dielectric function is analyzed. On the basis of this analysis, different screening models can be defined. The importance of the difference between these screening models is investigated in section two: Different mobilities - depending on the chosen screening model - are calculated for the remote ionized impurity and for the alloy scattering potential as a function of charge density and temperature and compared. Finally, mobilities of a modulated 2DEG are calculated as a function of charge density and temperature (section 3). Hereby, the influence of the scattering angle, the second Fourier coefficient of the lateral potential modulation and the impact of higher subbands are systematically studied.

All calculations are executed with the following parameters of a heterostructure: The Aluminum content in the channel is assumed to be $x_{Al} = 5\%$, in the barrier $x_{Al} = 33\%$, the spacer $r_{z_{pac.}} = 9$ nm, the residual impurities are $N_A = 2.9 \cdot 10^{14} \text{ cm}^{-3}$, resulting in a charge transfer of $N_s = 4.5 \cdot 10^{11} \text{ cm}^{-2}$ at $T = 4.2\text{K}$. It shall be emphasized that these parameters are identical for a modulated and an unmodulated 2DEG (However, in the case of a modulated 2DEG, the Aluminum content $x_{Al} = 5\%$ is modulated in one lateral dimension!)

5.1 Screening

In the following, the effect of including higher subbands in the dielectric function is analyzed.

The motivation to study the effect of including higher subbands in the dielectric function arises from experimental mobility measurements of unmod-

ulated and modulated 2DEG. The here presented results are one necessary part to understand the experimental results.

The first actual calculation of the mobility in the multisubband system was done by Nelson and Brown [Nelson 74] for bulk Si. Similar calculations were then performed by many other authors (for example [Ando 76][Stern 78] [Hai 95]). However, in these references, no comparison between different screening models were made.

The physical origin of enhanced screening when the second subband is populated (due to a high charge density ($N_s > 9 \cdot 10^{11} \text{cm}^{-2}$) or to higher temperature ($> 40\text{K}$) shall be first explained.

Principally, one has to distinguish between three different regimes at a given temperature:

- $E_F - E_0 \ll 6k_B T$: the electron system is not degenerate.
- $E_F - E_0 \gg 6k_B T$: the electron system is degenerate.
- $E_F - E_1 \gg 6k_B T$: the electron system is degenerate and the second subband is occupied.

Hence, the transition from one regime to the other depends on the position of the Fermi level¹ with respect to the (fundamental) subband and is thus a function of the charge density N_s and the temperature T : at sufficiently low density or sufficiently high temperature every system will not be degenerate. Reduced or enhanced charge densities are obtained by the application of an electric field. The five lowest subband energies, the Fermi level and the thermal energies $k_B T$ are listed in the following table for $T = 0\text{K}$ and $T = 70\text{K}$ for the three different cases $N_s(4.2\text{K}) = 2 \cdot 10^{11} \text{cm}^{-2}$, $N_s(4.2\text{K}) = 4.5 \cdot 10^{11} \text{cm}^{-2}$, $N_s(4.2\text{K}) = 1 \cdot 10^{12} \text{cm}^{-2}$.

As already discussed in chapter 3.6, the screening is described by the dielectric function. If there is only one subband populated, the dielectric function is a scalar and is given by [Stern 67]

$$\epsilon(\vec{q}, T, E_F) = 1 + q_0 \frac{F(\vec{q}, r_z, r_{z'}) \Pi(\vec{q}, T, E_F)}{q}, \quad (5.1)$$

with $q_0 = m^* e^2 / 2\pi \hbar^2 \epsilon_0 \epsilon_r$. In the case of including more than one subband, the dielectric function becomes a matrix which its elements given by

$$[\epsilon(q, T, E_F)]_{\alpha'\alpha, \beta'\beta} = \delta_{\alpha'\alpha, \beta'\beta} + q_0 \frac{F_{\alpha'\alpha, \beta'\beta}(\vec{q}, r_z, r_{z'}) \Pi_{\beta'\beta}(q, T, E_F)}{q} \quad (5.2)$$

¹Fermi level E_F is taken as a synonym of the chemical potential. With the Fermi energy E_F^0 is meant the Fermi level at $T = 0\text{K}$, i.e. $E_F^0 = E_F(T = 0\text{K})$.

	$N_s = 2e10^{11} \text{ cm}^{-2}$		$N_s = 4.5e10^{11} \text{ cm}^{-2}$		$N_s = 1e12^{11} \text{ cm}^{-2}$	
T (K)	4.2K	70K	4.2K	70K	4.2K	70K
E_F (meV)	7.69	5.78	15.17	14.12	33.66	32.01
E[0] (meV)	87.69	88.40	101.7	102.1	128.9	129.6
E[1] (meV)	112.1	113.1	128.2	129.3	161.5	164.6
E[2] (meV)	140.8	141.9	157.3	158.5	190.6	193.8
E[3] (meV)	154.6	155.9	172.4	174.0	208.7	213.1
E[4] (meV)	167.6	169.0	185.7	187.3	221.8	226.2
$k_B T$ (meV)	0.35	5.83	0.35	5.83	0.35	5.83

Table 5.1: *Subband energies and Fermi levels at $T = 4.2K$ and $70K$ for the three charge densities, exemplarily used in the calculations of this chapter.*

with the T - dependent polarizability $\Pi_{\alpha\alpha'}(\vec{q}, T, E_F)$ and the form factor $F(\vec{q}, r_z, r_{z'})$. It shall be reminded that α, β denote the initial subbands occupied by the two interacting electrons, and the indices α', β' denote the final subbands.

To show the influence of higher subbands on the screening, the total transition probability of a screened potential has to be calculated. It is given by [Sotirelis 93]

$$| \langle \xi_{\alpha'}(r_z) | V_{diff}^{eff}(\vec{q}, r_z) | \xi_{\alpha}(r_z) \rangle |^2 = \left| \sum_{\beta, \beta'} [\epsilon(q)]_{\alpha'\alpha, \beta'\beta}^{-1} \langle \xi_{\beta'}(r_z) | V_{ext}^{eff}(\vec{q}, r_z) | \xi_{\beta}(z) \rangle \right|^2.$$

This signifies that one sums over all β -subband transition "densities", with β the number of subbands one takes into account. It shall be underlined that it is of no interest to compare single inverse dielectric matrix elements with the (scalar) dielectric function $1/\epsilon(\vec{q})$ as found in literature [Tang 89]. Rather, the **total** transition probability of a screened potential has to be calculated.

5.1.1 Multisubband Polarizability Matrix

The multisubband static polarizability matrix for the subbands α and α' is given by [Stern 67]

$$\Pi_{\alpha\alpha'}(\vec{q}, T, E_F) = 2 \sum_k \frac{g^0(E_{\alpha} + \frac{\hbar^2}{2m^*} \vec{k}^2, E_F) - g^0(E_{\alpha'} + \frac{\hbar^2}{2m^*} (\vec{k} + \vec{q})^2, E_F)}{E_{\alpha} + \frac{\hbar^2}{2m^*} (\vec{k} + \vec{q})^2 - \frac{\hbar^2}{2m^*} \vec{k}^2} \quad (5.3)$$

which can be written in an integral representation [Maldague 78] by

$$\Pi_{\alpha\alpha'}(\vec{q}, T, E_F) = \int_{-\infty}^{\infty} dE G(E_F - E, T) \Pi_{\alpha\alpha'}^0(\vec{q}, E), \quad (5.4)$$

$$G(E_F - E, T) = \frac{\partial g^0}{\partial E} = \frac{1}{4k_B T \cosh^2[\frac{E_F - E}{2k_B T}]}.$$

$\Pi_{\alpha\alpha'}^0(\vec{q}, E_F)$ is the static polarizability function at $T = 0K$ defined as [Tang 89]

$$\begin{aligned} \Pi_{\alpha\alpha'}^{0,real}(\vec{q}, T = 0K, E_F^0) = & \quad (5.5) \\ & \frac{m^*}{\pi \hbar^2} \left\{ -[\omega_- - \text{sign}(\omega_-)] \left[\omega_-^2 - \frac{2E_{F_\alpha}^0 \vec{q}^2}{m^2} \right]^{\frac{1}{2}} \cdot \theta \left[\frac{m^* \omega_-}{\vec{q}^2} - 2m^* E_{F_\alpha}^0 \right] \theta(E_{F_\alpha}^0) \right. \\ & \left. - [-\omega_+ + \text{sign}(\omega_+)] \left[\omega_+^2 - \frac{2E_{F_\alpha'}^0 \vec{q}^2}{m^2} \right]^{\frac{1}{2}} \cdot \theta \left[\frac{m^* \omega_+}{\vec{q}^2} - 2m^* E_{F_\alpha'}^0 \right] \theta(E_{F_\alpha'}^0) \right\} \end{aligned}$$

with

$$\begin{aligned} \omega_- &= E_\alpha - E_{\alpha'} - \frac{\hbar^2 \vec{q}^2}{2m^*} \\ \omega_+ &= E_\alpha - E_{\alpha'} + \frac{\hbar^2 \vec{q}^2}{2m^*} \\ E_{F_\alpha}^0 &= E_F^0 - E_\alpha \end{aligned}$$

Furthermore, $\text{sgn}(x) = +1$ (-1), if x is positive (negative). Θ is the Heaviside function.

If only one subband is occupied, equation 5.5 simplifies to the well - known equation [Stern 67]

$$\Pi(\vec{q}, T = 0K, E_F^0) = \frac{m^*}{\pi \hbar} (1 - \theta(\vec{q} - 2k_F) (1 - \sqrt{1 - (\frac{2k_F}{q})^2})). \quad (5.6)$$

Inspection of equation 5.4 indicates that the main contribution to the integral is in the region $E = E_F$. The factor $G(E_F - E, T)$ approaches $\delta(E_F - E)$ as the temperature decreases to zero and becomes $1/4k_B T$ for very large T , which is due to the property of the derivative of the Fermi - Dirac function $\frac{\partial g^0}{\partial E}$. The behavior of the intrasubband polarizability matrix element of the ground state Π_{00} is shown in Fig. 5.1 as a function of $q/2k_F$ for different temperatures for $N_s = 4.5 \cdot 10^{11} \text{ cm}^{-2}$. For small q the polarizability is constant and equal to the density of state $\frac{m^*}{\pi \hbar}$ and diminishes as $\frac{1}{q}$ for $q > 2k_F$. At higher temperature,

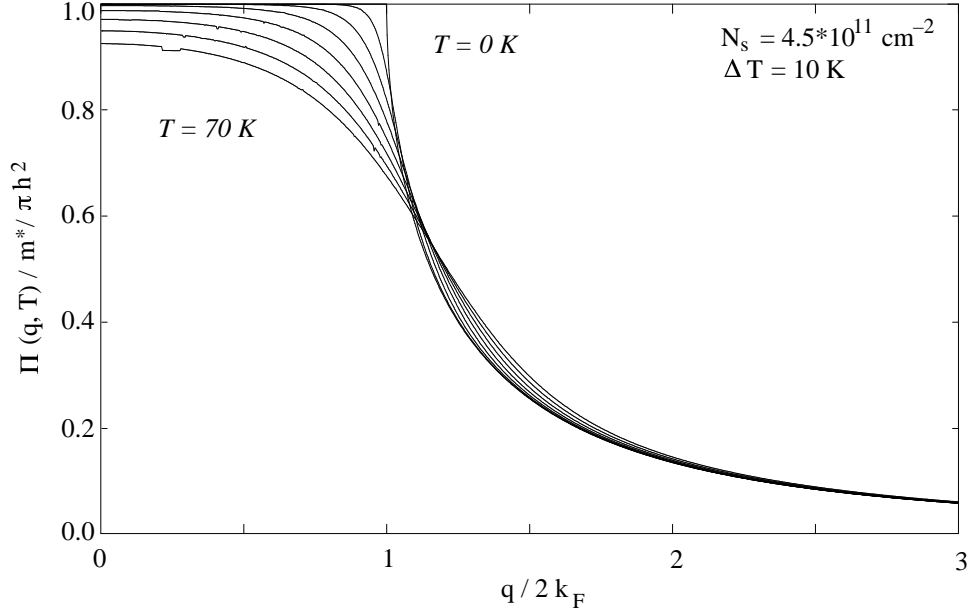


Figure 5.1: *Intrasubband polarizability as a function of $q/2k_F$ for $T = 0K, 10K, \dots, 70K$ for $N_s = 4.5 * 10^{11} \text{ cm}^{-2}$; with higher temperature the polarizability decreases for small q .*

the polarizability is weakened for $q < 2k_F$ with respect to the case $T = 0K$ and enhanced for $q > 2k_F$. This is well known [Stern 67]. However, less well known is that the temperature dependence of the polarizability function also depends on the considered charge density, as will be discussed in the following.

It is important to note that in the case of $T > 0K$, the decrease of the polarizability for small \vec{q} is intrinsically related to the temperature dependence of $g^0(E)$ and depends on the position of the Fermi level (and hence on the considered charge density) with respect to the fundamental subband: if $E_F - E_0$ is small (slightly degenerate system), the polarizability will diminish as soon as the temperature increases (and hence $6k_B T > E_F - E_0$; in opposite, if $6k_B T < E_F - E_0$ (strongly degenerate system), the polarizability is hardly temperature dependent. This behavior is depicted in Fig. 5.2 where the intrasubband polarizability of the fundamental subband is calculated a) for a weakly degenerate case ($N_s = 2 * 10^{11} \text{ cm}^{-2}$, $E_F^0 - E_0 = 7.7 \text{ meV}$ at $T = 0K$ and b) for a strongly degenerate case ($N_s = 1 * 10^{12} \text{ cm}^{-2}$, $E_F^0 - E_0 = 33.7 \text{ meV}$ at $T = 0K$). While the polarizability matrix elements remain nearly constant

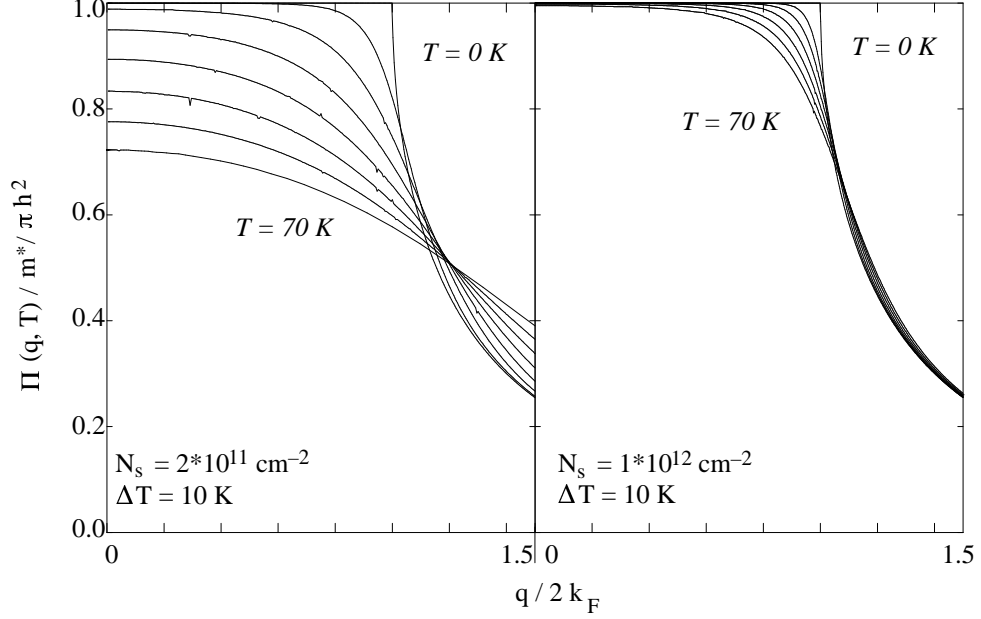


Figure 5.2: *Polarizability as a function of $q/2k_F$ in the case for an undegenerate (left) and degenerate (right) 2DEG. While in the case of an undegenerate 2DEG the polarizability depends strongly on the temperature, the polarizability of a degenerate 2DEG remains almost temperature independent.*

between $T = 0K$ and $T = 70K$ for the strongly degenerate case (b), it diminishes for T greater than $T = 20K$ for the weakly degenerate case (a). This is easily understandable by looking at Fig. 5.3, where the derivative of the Fermi Dirac function (according to the corresponding temperature), centered at each Fermi level E_F (corresponding to the undegenerate case) is shown. (Note that the Fermi level is in the given examples almost temperature independent and thus the temperature dependence of the polarizability function is in first order determined by the Fermi - Dirac function.) In the case for the weakly degenerate case, at $T > 20 K$, when integrating $\partial g^0 / \partial E$, one "loses" states on the lower energetical side, since no states for $E < E_0$ exist. Oppositely, for the strongly degenerate case, $\partial g^0 / \partial E$ is always integrated in a range $\mu \pm 6kT > E_0$.

Another important feature are the intersubband polarizability matrix elements, which shall be discussed next. As one can see from equation 5.5, one expects also intersubband contributions, even if only one subband is beneath the Fermi energy, since one term in equat. 5.5 will be different from

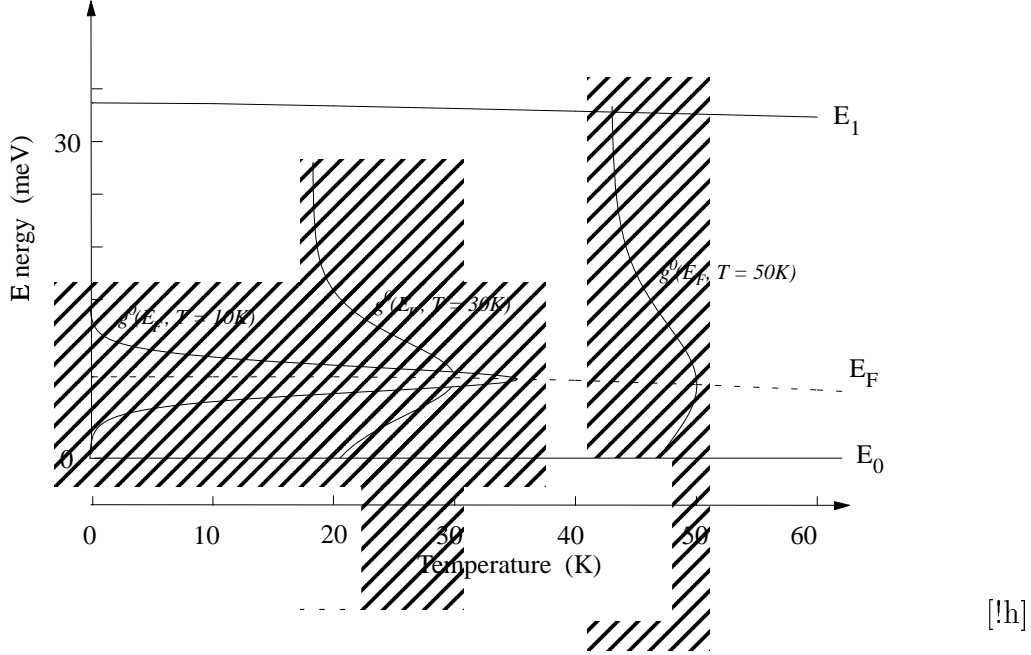


Figure 5.3: *Sketch of the integration limits for the polarizability function: as soon as $6k_B T > E_0$, the polarizability matrix elements diminish for $q < 2k_F$ due to the non - existence of states with $E < E_0$.*

zero. This is shown in Fig. 5.4, where the intersubband polarizability matrix elements $\Pi_{0\alpha}$ with $\alpha = 0 \dots 4$ for $T = 0K$ are shown.

The Fermi energy is 16 meV above the first energy level, thus 12 meV beneath the second one. As seen in the figure, the intersubband polarizability Π_{01} matrix element is non - vanishing: it has a value of $\sim 60 \%$ of the intra-subband matrix element Π_{00} . Naturally, the magnitude of the intersubband polarizability elements $\Pi_{\alpha\alpha'}$ depends on the position of the Fermi level with respect to the subbands α, α' , determining the intersubband matrix elements $\Pi_{\alpha\alpha'}$. In Fig. 5.5 the intersubband matrix element Π_{01} is shown for different Fermi energy positions: as the Fermi energy E_F^0 approaches the second subband, the polarizability increases, thus resulting in an enhanced screening. However, if the Fermi energy is far away from a subband, the contributions from this intersubband polarizability element are negligible. This justifies a n - subband approximation (with an n - subband approximation is meant that only the n lowest subbands are considered and all higher subbands are neglected.) Already at this point it becomes obvious that taking only one subband into account leads to an underestimation of the screening. Natu-

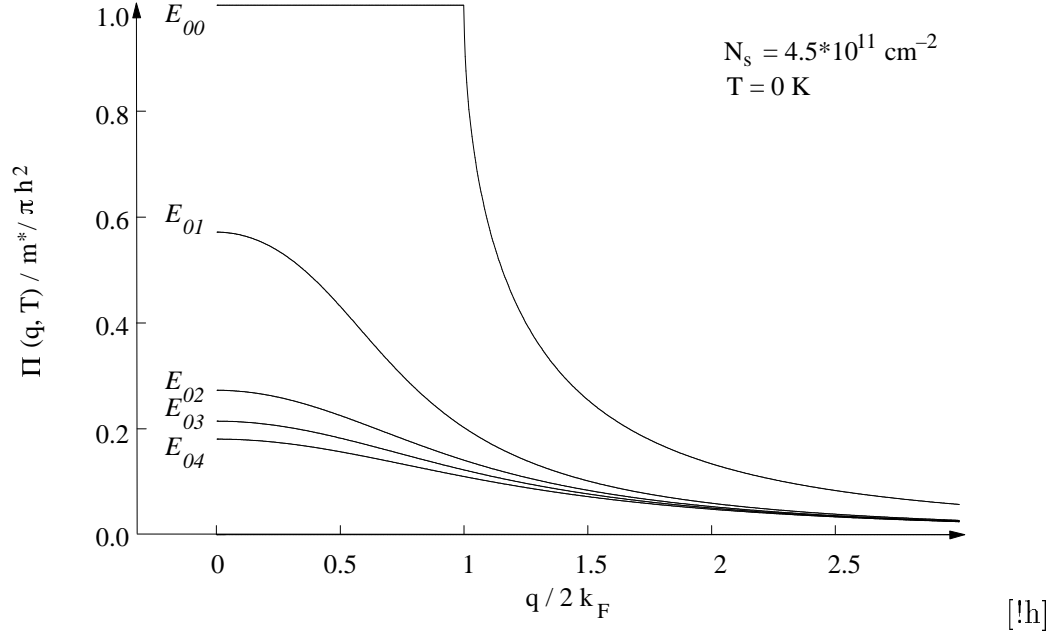


Figure 5.4: *Intersubband matrix elements as a function of $q/2k_F$ for $T = 0K$: with increasing distance $E_\alpha - E_F^0$, the strength of the matrix element decreases.*

rally, the error committed by only taking one subband into account becomes more pronounced at higher temperatures and or higher charge densities when energetical higher subbands are occupied.

The result that higher, unoccupied subbands contribute to the screening, even when they are above the Fermi level, is at first glance a surprising fact. These classical not allowed transitions to states above the Fermi level are due to the quantum mechanical allowed virtual transitions [Hai 95].

The second important term to determine the strength of the interaction (e.g. in which way the interactions are screened) is given by the formfactor $F_{\alpha'\alpha,\beta'\beta}(\vec{q})$ (equation 5.2) which will be discussed next.

5.1.2 Formfactor

The formfactor

$$F_{\alpha'\alpha,\beta'\beta}(\vec{q}, r_z, r_{z'}) = \int dr_z dr_{z'} \xi_{\beta'}(r_{z'}) \xi_{\alpha'}(r_{z'}) \xi_{\beta}(r_z) \xi_{\alpha}(r_z) e(-q|r_z - r_{z'}|) \quad (5.7)$$

is due to the finite extension in the r_z - direction of the wavefunctions of the quasi two - dimensional electron system [Bastard 88]. Its role is to average

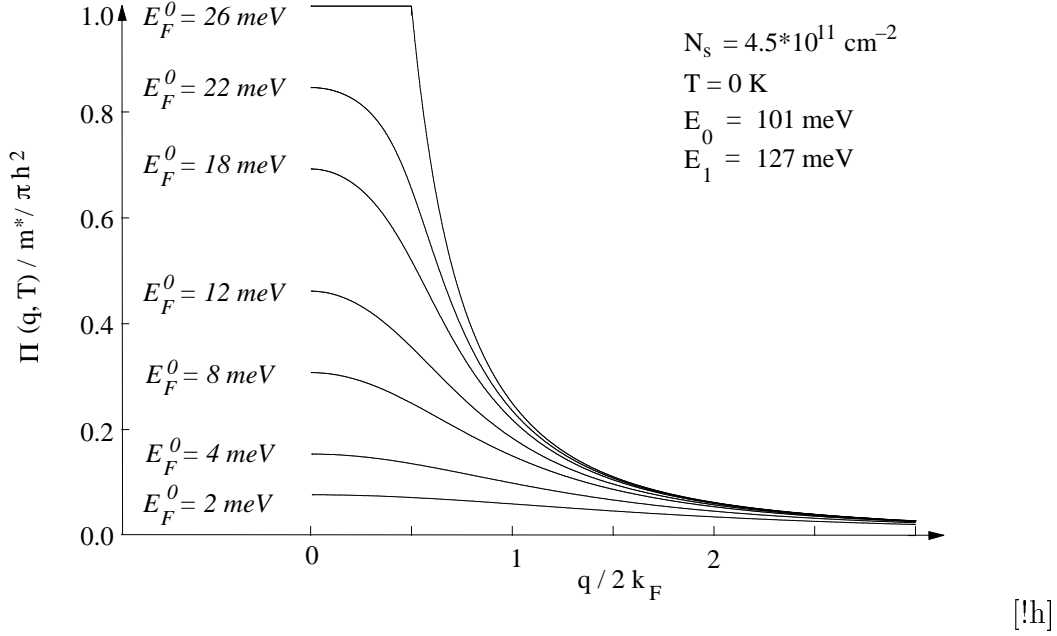


Figure 5.5: *Intersubband matrix element Π_{01} for different positions of the Fermi energy at $T = 0 \text{ K}$. The contribution increases as the Fermi energy approaches the second subband.*

over the charge distribution in the quantum structure. Naturally, it does not depend explicitly on the temperature. Taking a two subband structure, one obtains six different form factors which are depicted in Fig. 5.6 as a function of $q/2k_F$. They are all of similar value at large q . In the limit $q \rightarrow 0$, the form factors for interactions which involve intrasubband transitions tend to unity, while the form factors for interactions involving intersubband transitions tend to zero. This is due to the orthogonalization of the wavefunctions.

Before comparing transition probabilities (e.g. mobilities) for different interaction potentials for an unmodulated 2DEG, one effect, which will turn out to be of special importance for modulated 2DEG's shall be emphasized: The importance of taking higher subbands into account, depends also on the considered scattering vector \vec{q} . This is immediately clear, if one looks once again at Fig. 5.1. At greater q , regardless of the temperature, the polarizability becomes similar; oppositely, at smaller q the polarizability depends for lower charge density on the temperature. This behavior is visualized in Fig. 5.7: The transition probability for remote impurity scattering is calculated as a function of temperature for two different values of the scattering vector

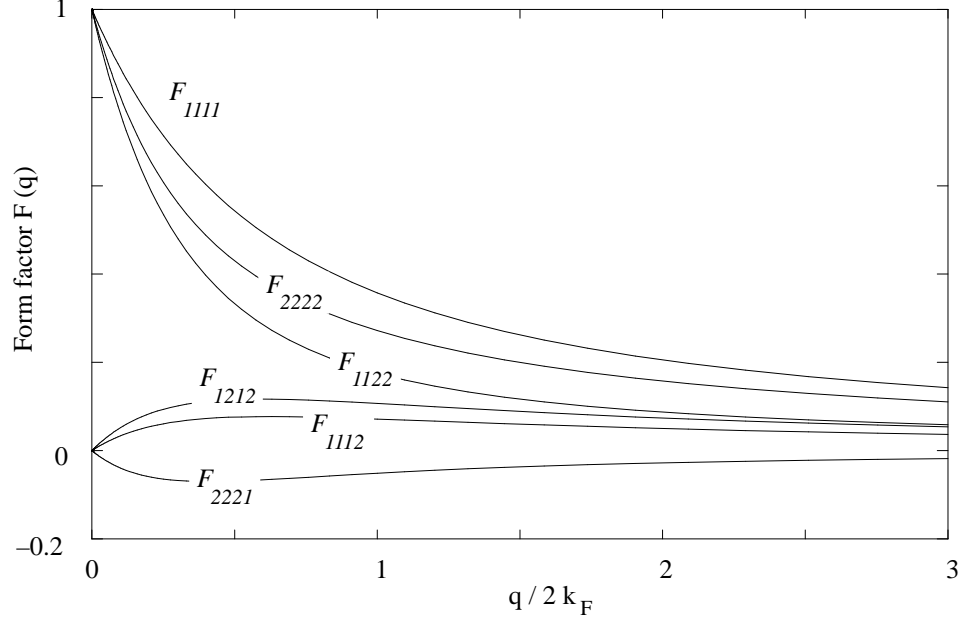


Figure 5.6: *Formfactors for a system of two subbands: for large q , they are all of similar value, whereas at small q the formfactors involving intersubband transitions tend to unity whereas the one involving intersubband transitions become equal to zero.*

\vec{q} , once in the frame of a one subband dielectric function model, once while taking five subbands into account. For this calculation the band structure is always the one calculated at $T = 0\text{K}$. Consequently, all temperature effects arise solely from the polarizability function.

The effect of diminishing the unscreened potential modulation is more important for smaller q and especially in the temperature range between 40 - 60K. As expected, taking higher subbands (here five) into account, results in a smaller effective scattering potential. The difference between the one subband approximation and five subband approximation becomes more important at higher temperature. For comparison, the transition probability when taking a temperature independent one subband dielectric function is also shown (in a thin line). It is remarkable that within the temperature range of this work (up to 70K) one commits a smaller error by taking a temperature independent $\epsilon(\vec{q})$ (with respect to the the temperature dependent, multisubband dielectric function), than taking the temperature dependent one subband dielectric function. This is easily understandable, because the temperature dependence of $\epsilon(\vec{q})$ and the inclusion of more than one subband

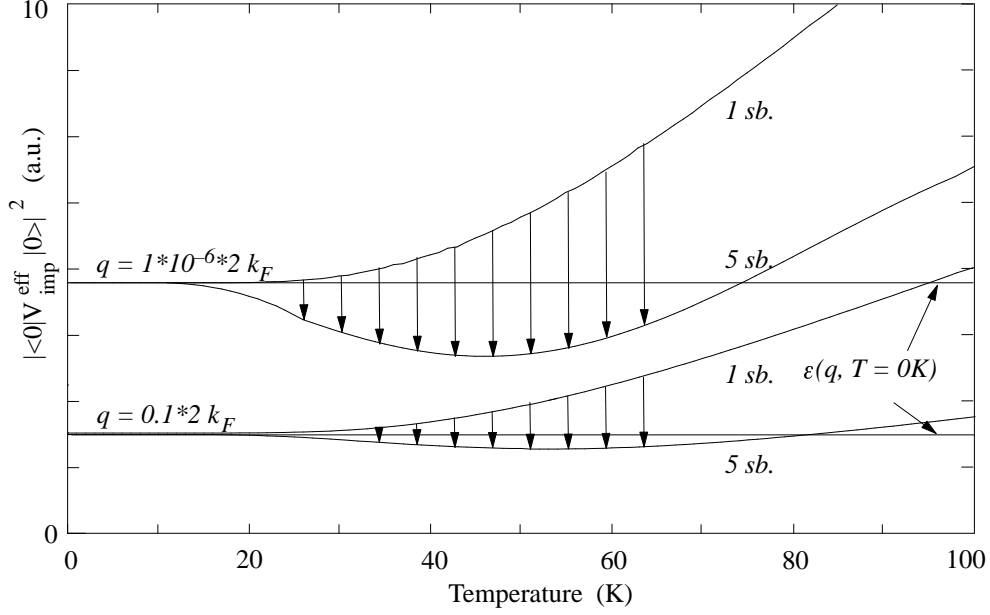


Figure 5.7: *Transition probability for remote ionized impurity scattering as a function of temperature for two different values of the scattering vector \vec{q} , once while taking one subband, once while taking five subbands into account: The effect of enhanced screening due to higher subbands is the more important, the smaller the scattering vector is.*

have the tendency to compensate each other: having reduced polarizability matrix elements at higher temperature (e.g. the screening is reduced), the inclusion of higher subbands results in an increase of the screening (due to the contribution of intersubband polarizability matrix elements). This, once again is more pronounced for small \vec{q} - vectors, where the variations of the polarizability as a function of temperature is more important.

5.2 Effective Interaction Potentials for Unmodulated 2DEG's

The impact of the in the previous section discussed enhanced screening on the mobility shall be discussed. For this reason, the mobility limited by remote ionized impurity scattering and the mobility limited by alloy scattering is calculated as a function of charge density and temperature for the following

different screening models:

- model 5 subbands: when calculating the dielectric function, the five lowest energy subbands are taken into account.
- model 2 subbands: when calculating the dielectric function, only the two lowest subbands are taken into account.
- model 1 subband: when calculating the dielectric function, only the fundamental subband is taken into account. This means that every matrix element is screened by the dielectric function of the first subband, regardless to which subband the states belong to.
- model "5 subbands, no intersubband screening": This is a model which is also quite often found in literature: it consists of neglecting all intersubband screening, e.g. every transition is screened by the proportional dielectric function matrix element respectively e.g.

$$\langle \alpha | V_{diff}^{eff} | \alpha' \rangle = \frac{\langle \alpha | V_{diff}^{ext} | \alpha' \rangle}{\epsilon_{\alpha\alpha'}(\vec{q})}$$

- long wavelength limit approximation ("Thomas - Fermi approximation"): In this approximation, the small \vec{q} limit is assumed, regardless of the scattering vector \vec{q} of the considered transition, e.g. the polarizability is $\Pi(\vec{q}, T) = \Pi(0, T)$.

It shall be reminded that the two considered scattering potentials have a different scattering vector dependence. This is visualized in Fig. 5.8, where the transition probability $|\langle 0 | V^{scatt} | 0 \rangle|^2$ is calculated as a function of the scattering vector q . The remote ionized impurity scattering favors small angle scattering (the most probable q is at about $q_{prob.} \sim 0.1 k_F$). Since the q - distribution is peaked around $q_{prob.}$, the averaged q ($\langle q \rangle$) is equally approximately $0.1 k_F$. In contrast, the alloy scattering potential favors scattering processes, involving large scattering vectors, leading to a $q_{prob.} \sim 2k_F$. Due to the large q - distribution, $\langle q \rangle$ is approximately given by k_F . This different q - dependence leads to the well known charge density and temperature behavior of the mobilities attached to these scattering potentials (Fig. 5.9) [Hirakawa 86]: The mobility limited by remote ionized impurity scattering increases with increasing charge density and with increasing temperature (Fig. 5.9.a), whereas the mobility limited by alloy scattering decreases with

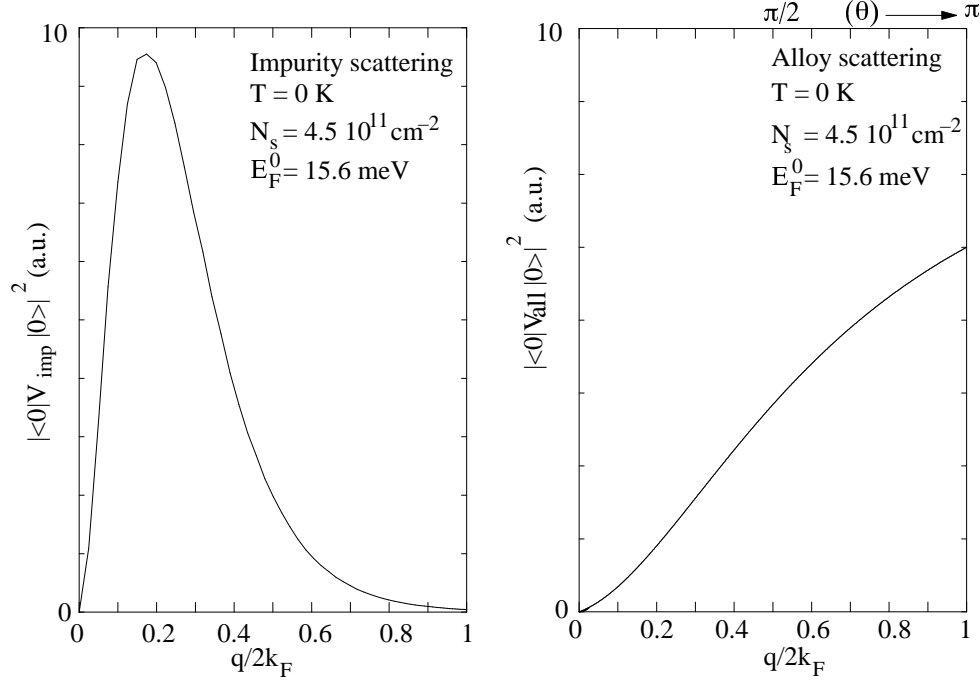


Figure 5.8: The transition probabilities $|\langle 0|V_{all}|0\rangle|^2$ as a function of $q/2k_F$ for the screened remote ionized impurity scattering (left) and for the screened alloy scattering potential (right): Remote ionized impurities favor small angle scattering, whereas the alloy scattering potential favors large angles scattering, spread in a large q - distribution.

increasing charge density and temperature (Fig. 5.9.b). This is discussed in more detail in [Hirakawa 86].

To evaluate the differences between the above present screening models, in Fig. 5.10 the mobility limited by remote ionized impurity scattering (a) and limited by alloy scattering (b) is calculated as a function of charge density for $T = 0$ K for the above discussed screening models.

One distinguishes three different zones:

1. $N_s \ll N_s(\text{intersubband})$: only one subband is occupied.
2. $N_s = N_s(\text{intersubband})$: the second subband starts to be populated. This becomes obvious in the mobility by a decrease due to intersubband scattering.
3. $N_s \gg N_s(\text{intersubband})$: the first and second subband are populated.

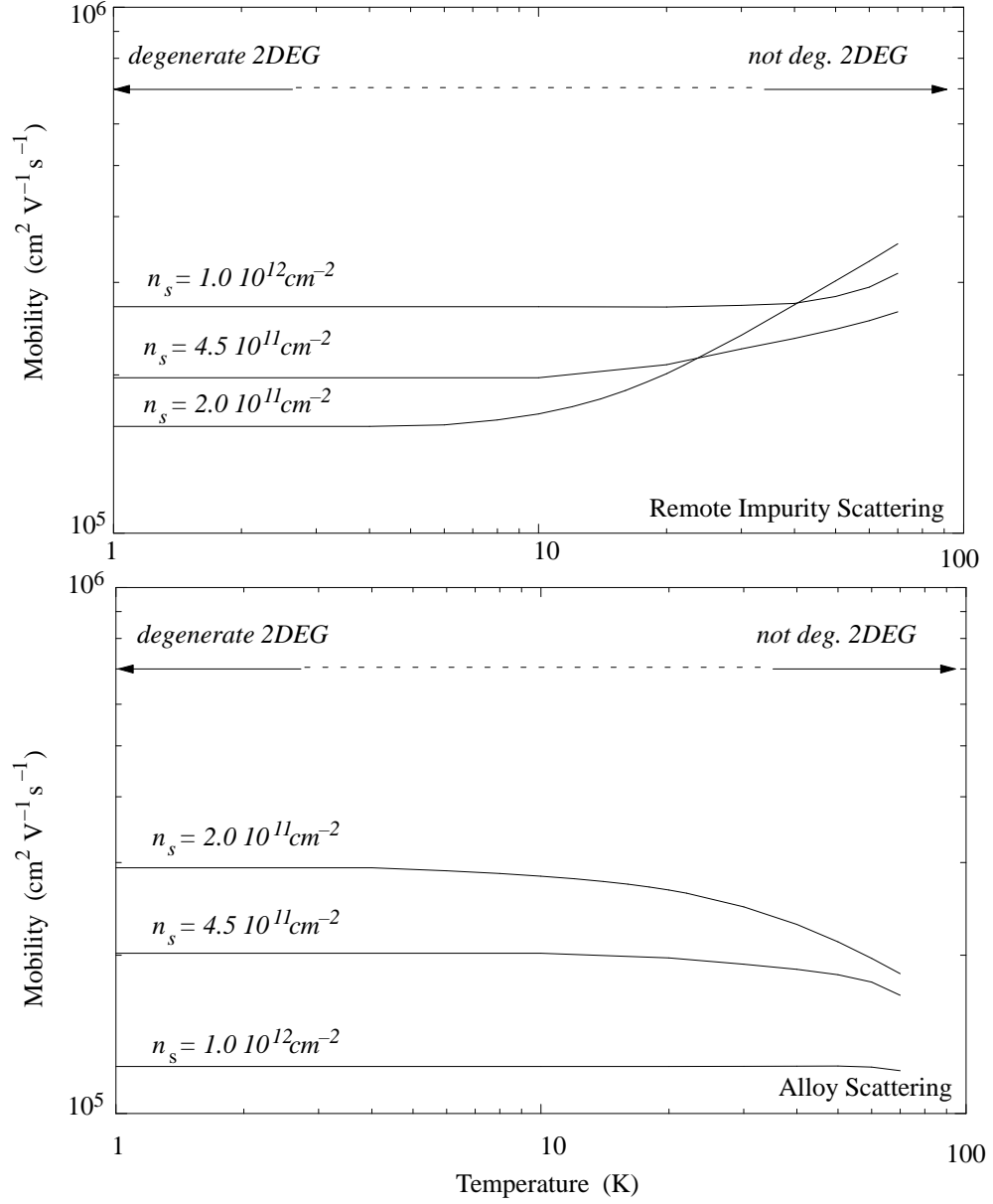


Figure 5.9: Mobility limited by impurity scattering (a) and by alloy scattering (b) as a function of temperature for three different charge densities: The mobility increases with increasing charge density and with increasing temperature in the case of remote impurity scattering, whereas it decreases in the case of alloy scattering.

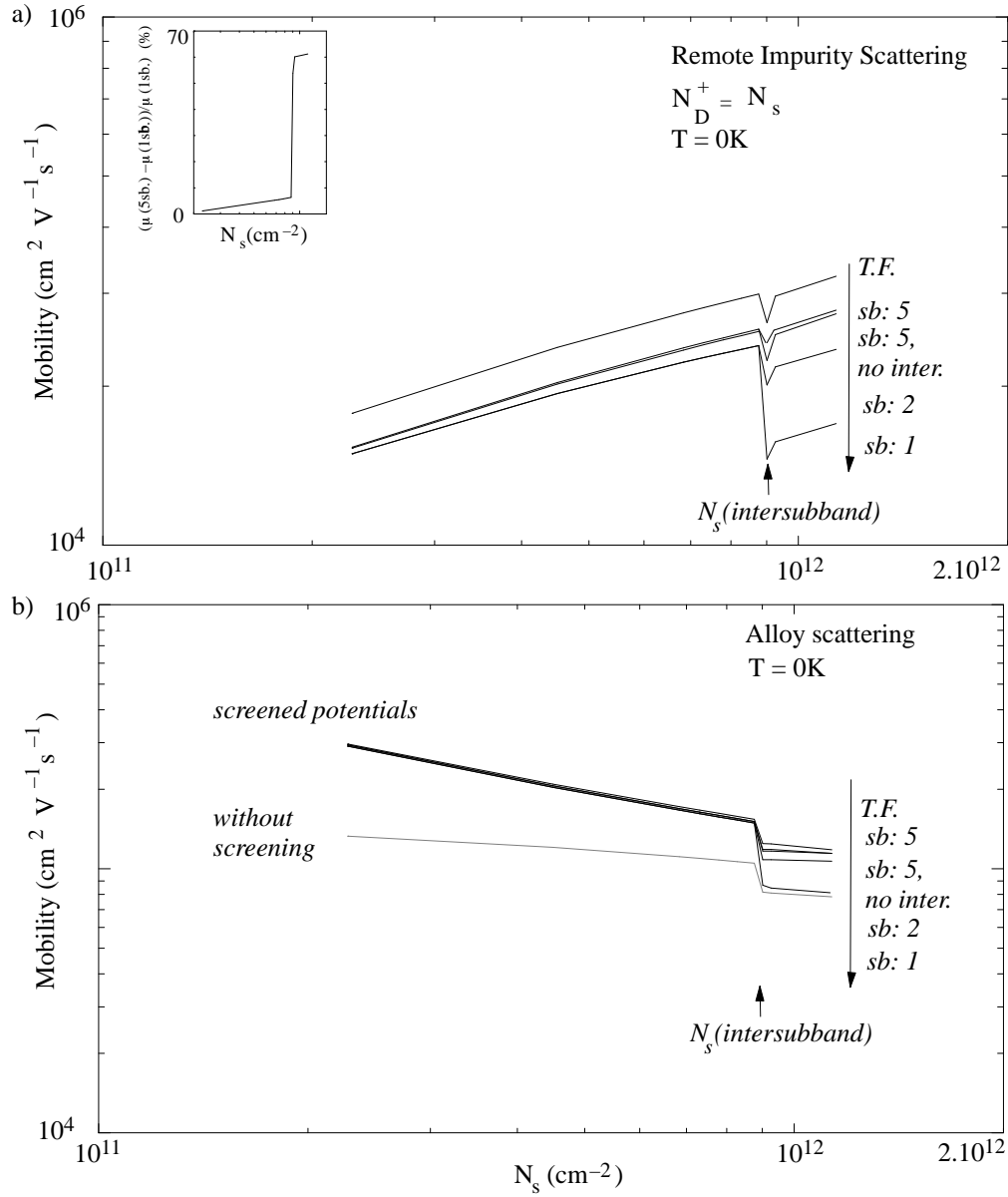


Figure 5.10: Mobility as a function of charge density for remote ionized impurity scattering (a) and alloy scattering (b) at $T = 0K$. Each curve corresponds to a different screening model. Including higher subbands in the dielectric constant, becomes especially important when the second subband starts to be populated.

Looking on the different curves in Fig. 5.10.a (remote ionized impurity scattering), the difference between including one or five subbands in the dielectric function is more pronounced when the second subband becomes populated. In the inset of Fig. 5.10.a, the relative difference between the mobilities, including five or one subbands in the dielectric function is shown. The difference increases gradually with increasing charge density and becomes significant as soon as the second subband is populated. Regarding Fig. 5.10.b (alloy scattering), one basically finds the same results of enhanced screening when $N_s \gg N_s(\text{intersubband})$ as in the case of remote ionized impurity scattering. However, the difference between the five subband model and the one subband model is less pronounced. As the second subband gets populated, the mobility limited by alloy scattering decreases 19% when including five subbands in the dielectric function, whereas including only one subband leads to a mobility drop of 40%. This is consistent with the above explained q - dependence of the effect of enhanced screening: as smaller the scattering vector q is, as greater is the effect of the inclusion of higher subbands in the dielectric function.

Calculated results of other screening models are equally shown. Suppressing contributions from intersubband matrix elements in the dielectric subband calculations turn out to be a fairly good approximation, differing 7% from the as most exact considered five subband screening model. Thus, to simplify the numerical calculations, one can justify for remote ionized and for alloy scattering in the here considered charge density range the intersubband matrix elements. Naturally, the long wave length approximation (Thomas Fermi approximation) overestimates the screening, thus calculating a higher mobility. There is no significant difference to observe between taking two or five subbands into the screening model into account. The difference becomes greater as one approaches the third subband (not shown here). This demonstrates the justification of taking $(n + 1)$ - subbands into account, when calculating the dielectric function, where n is the number of occupied subbands.

In Fig. 5.11 the temperature dependent mobility for a charge density of $n_s = 4.5 \cdot 10^{11} \text{ cm}^{-2}$ is shown for remote ionized impurity scattering (a) and alloy scattering (b) for different screening models. In the insets the relative increase of the mobility, when taking five subbands into account with respect to the one subband screening model is shown as a function of temperature. Once again, it is obvious that taking higher subbands into account becomes more important when higher subbands are populated, thus at higher temperature (resulting in a difference in the calculated mobilities up to 35% at

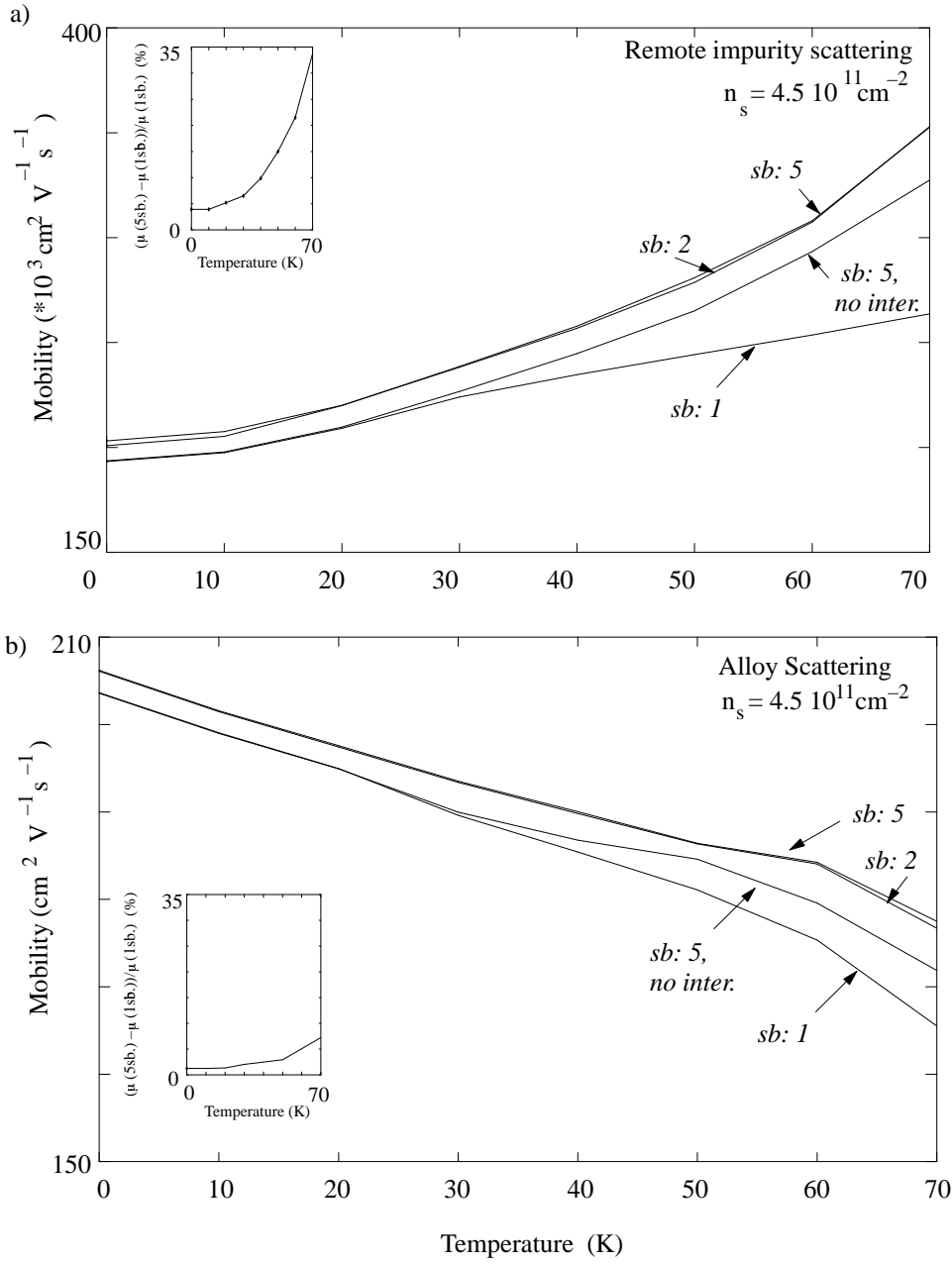


Figure 5.11: Mobility limited by remote ionized impurity scattering (a) and for alloy scattering (b) for different screening models: at higher temperature the mobility when taking higher subbands into account is up to 35 % higher (remote ionized impurity scattering) with respect to a one subband dielectric function.

$T = 70\text{K}$, when remote ionized impurity is considered). Integrating $\Pi(\vec{q}, T, E_F)$ at higher temperature has the contribution of intersubband polarizability matrix elements in the dielectric function calculation for consequence. This can be nicely seen by comparing the results of the 2 (or 5 subband) screening model with the five subband screening model, neglecting intersubband contributions: at low temperature the difference in the mobility of these two calculations is solely due to the intersubband matrix element $\Pi_{0\alpha}$, α denoting upper subbands. As the temperature increases, higher subbands become populated, resulting in a more efficient screening by the following processes:

- the intrasubband polarizability matrix elements of higher subbands start to contribute. This is documented by the beginning difference between the model "five subbands no intersubband transition" and the model taking one subband into account: between $T = 0\text{K}$ and $T = 30\text{K}$, there is no difference between the two models, showing that there are no intrasubband contributions from higher subbands. From $T = 30\text{K}$ on, a difference of the two models can be remarked, becoming greater at higher temperature.
- equally, the intersubband contributions increase slightly. This manifests itself by the difference between the models "five subbands" and "five subbands no intersubband transition", which increases slightly with temperature. However, this contribution is far less important than the contribution due to the intrasubband polarizability of higher subbands.

Remarkably, the difference of including five subbands instead of one in the dielectric function is five times more pronounced for the impurity scattering potential than for the alloy scattering potential. This is due to the different q - dependence of the considered scattering potentials and the fact that the effect of enhanced screening is more dominant at smaller scattering vector.

In conclusion, a significant difference between a screening model taking higher subbands into account and the one taking only one subband into account becomes apparent at higher temperature and higher charge density. Taking higher subbands into account, the screening is more efficient, resulting in a higher mobility. In a simplified picture, this corresponds well to the idea that going from 2D to 3D, the Coulomb interaction $V(q)$ changes from $1/q$ to $1/q^2$ implying a better small q screening.

The consequence of this q - dependent effect of the multisubband screening will be even more interesting for modulated 2DEG's. The reason for this will be explained in the next section.

5.3 Effective Interaction Potentials for Modulated 2DEG's

To deal with a modulated 2DEG means looking at the bridge between a two - dimensional and a one - dimensional electron gas. Interesting new effects are expected due to the lateral potential modulation in one direction.

This section discusses these effects (with respect to an unmodulated electron gas) and shows, how they manifest themselves in the transport properties of a modulated 2DEG. Similar calculations were already made 1979 by T. Ando [Ando 79]. However, he only assumes a short range scattering potential and discusses only the energy range around the first minigap. Additionally, he does not discuss temperature dependent effects. In the following the parallel and perpendicular mobility of a lateral modulated 2DEG are discussed for both a long range scattering potential (remote ionized impurity scattering) and a short range scattering potential (alloy scattering) as a function of charge density as well as temperature. This discussion allows to show how the parallel and perpendicular mobility of a modulated 2DEG is changed due to the modified bandstructure, i.e. due to the minigaps and minibands in the perpendicular direction.

The discussion will be mainly based on regarding the change of the Fermi surface, as the Fermi energy is swept through the band structure, and its consequences for the transport properties. All Fermi energy surfaces will be presented in reduced Brillouin zone.

As already stated, in the best realized lateral superlattices of this work, the potential modulation has an estimated potential modulation peak to peak of about $V_{pp} \sim 15$ meV and the periodicity is given in these samples by the terrace length $L_{\perp} = 32$ nm, corresponding to an inclination angle of 0.5° . One thus finds $\lambda_F \sim L_{\perp}$ and $E_F \sim V_{pp}$, leading to a strongly modulated electron system. Their Fermi surfaces are expected to be strongly modified with respect to the unmodulated case: Due to the lateral periodical potential modulation, minigaps and minibands arise in the direction of the lateral potential modulation, leading to the modification of the Fermi surface and thus changing the transport properties of the considered modulated two dimensional electron gas. The way, in which the Fermi surface differs from the isotropic two dimensional Fermi surface depends naturally on the position of the Fermi energy with respect to the band structure of the modulated two dimensional electron gas.

In Fig. 5.12 three band structures with its corresponding Fermi surfaces are depicted: in Fig. 5.12.a, the Fermi energy is in the middle of the first

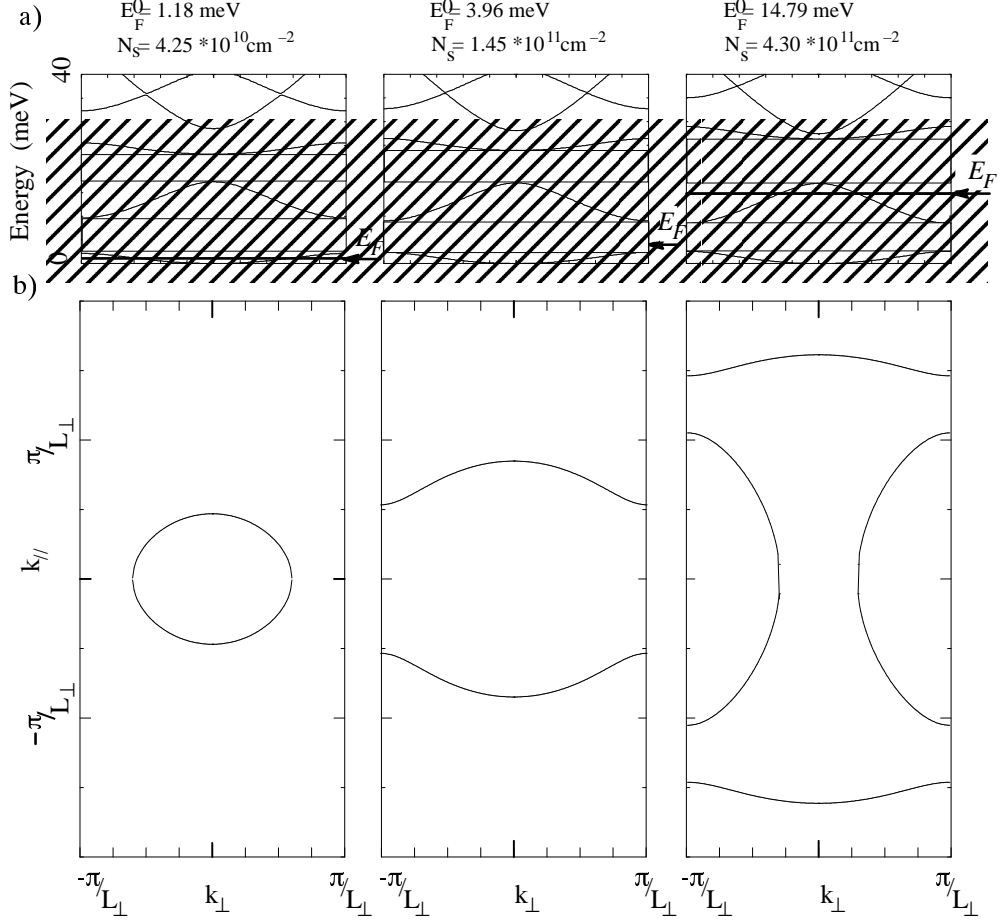


Figure 5.12: Bandstructures (a) at $T = 0K$ and corresponding Fermi surface (b) for different positions of the Fermi energy. From left to right: $E_F^0 \in E_{band}^{(1)}$, $E_F^0 \in E_{gap}^{(1)}$ and $E_F^0 \in E_{band}^{(2)}$. The first and second minigap are indicated by zebras. As the Fermi energy is in the second miniband, "lenses" due to the second miniband appear in the Fermi surface. At higher energy, the second subband is equally visible.

miniband ($E_F^0 \in E_{band}^{(1)}$). The corresponding Fermi surface does not differ significantly from the one of a 2DEG, e.g. differs only little from a circle. For this reason one does not expect a great difference of the transport properties of a modulated 2DEG with respect to an unmodulated electron gas in this energy range. In Fig. 5.12.b, the Fermi energy is in the first minigap $E_F^0 \in E_{gap}^{(1)}$. The corresponding Fermi surface is strongly modified with respect to an isotropic Fermi surface. As the Fermi energy approaches the second mini-

band, the minigaps become greater. Consequently, the deviation from the Fermi surface of an unmodulated electron gas becomes more important. The deviation is greatest just before the Fermi energy enters the second miniband and its magnitude depends naturally on the strength of the lateral potential modulation. Once the Fermi energy has crossed the second miniband (Fig. 5.12.c), "lenses" due to the second miniband appear at the edges of the Brillouin zone in the Fermi surface. As the Fermi energy increases, these "lenses" become larger.

In the following, the mobility of a modulated 2DEG and especially the consequences of the distortion of the Fermi surface for the mobility shall be investigated. In a first step, numerical results as a function of Fermi energy at $T = 0\text{K}$ will be presented. In a second step, the temperature dependence of the transport properties is discussed.

Comparing the mobility limited by remote ionized impurity scattering (long range scattering potential) with the mobility limited by alloy scattering (short range scattering potential) gives the possibility to sensor or analyze the particular feature of the Fermi surface of a modulated 2DEG in two different approaches: The characteristic of the remote ionized scattering potential is the small angle scattering. One thus is especially sensitive to the local change of the Fermi surface. Contrarily, regarding the alloy scattering potential, one gets an averaged, global view of the Fermi surface, since the averaged scattering vector is rather great (around k_F , see section 5.2).

5.4 Mobility as a Function of Fermi Energy

In this section, the temperature is always assumed to be $T = 0\text{K}$. The Fermi energy is changed by changing the charge density. Since the calculations are performed at $T = 0\text{K}$, the Fermi energy corresponds to the kinetic energy of the electrons. The strength of the lateral potential modulation is assumed to be $V_{pp} = 23\text{ meV}$, leading to a first minigap of size $E_{gap}^{(1)} = 6\text{ meV}$ and a second minigap of size $E_{gap}^{(2)} = 9\text{ meV}$ ($V_{sd}^{(2)} = 2.0$). The scattering angle θ is taken as the one between the group velocities of the states \vec{k} and \vec{k}' in the discussion of the general behavior of the mobility, e.g. $\theta \equiv \theta_{\vec{v}_k}$, and only one subband is taken into account while calculating the dielectric function. In a first approach, the general behavior of the mobility of a modulated 2DEG as a function of Fermi energy shall be discussed for remote ionized impurity and alloy scattering, in a second step, the influence of the following parameters on the mobility shall be discussed in detail:

1. the scattering angle $\theta_{\vec{v}_{\vec{k}}}$ "against" the scattering angle $\theta_{\vec{k}}$,
2. the influence of the second Fourier component of the lateral potential modulation,
3. the influence of taking higher subbands in the dielectric function into account.

It shall be reminded that the parallel (perpendicular) direction corresponds to the direction, which is parallel (perpendicular) to the lateral potential modulation. Hence with parallel (perpendicular) mobility is meant the parallel (perpendicular) component of the mobility.

5.4.1 Small Angle Scattering Potential

It shall be reminded that the remote ionized impurity potential is given by

$$V_{imp}^{ext}(\vec{R}) = \frac{-e^2 Z_i}{4\pi \epsilon_0 \epsilon_r} \frac{1}{|\vec{R} - \vec{R}_i|} \quad (5.8)$$

$$= \frac{-e^2 Z_i}{4\pi \epsilon_0 \epsilon_r S} \sum_{\vec{q}(2D)} \frac{2\pi}{q} e^{-q|r_z - r_{z_i}|} e^{-i\vec{q}(\vec{r} - \vec{r}_i)} \quad (5.9)$$

and favors strongly scattering processes with small scattering vector \vec{q} (see Fig. 5.8).

In Fig. 5.13, the parallel (a) and perpendicular (b) mobility limited by remote ionized impurity scattering is shown as a function of Fermi energy. As a reference, the mobility of an unmodulated 2DEG with the same structure parameters is shown (dashed line). The energy of the minibands and minigaps are indicated by vertical straight lines.

The behavior of the parallel and perpendicular mobility limited by remote ionized scattering can be explained by the following two features:

1. the scattering potential favors small angle scattering, leading to a general increase of mobility with increasing Fermi energy. This general behavior is equally shown in Fig. 5.9.a for an unmodulated 2DEG.
2. the density of state increases drastically on the energetical lower side of a minigap, decreases like $1/\sqrt{E}$ (one -dimensional behavior) in the energy range of the minigap and has a step function like increase at the onset of a miniband (see. Fig. 2.13).

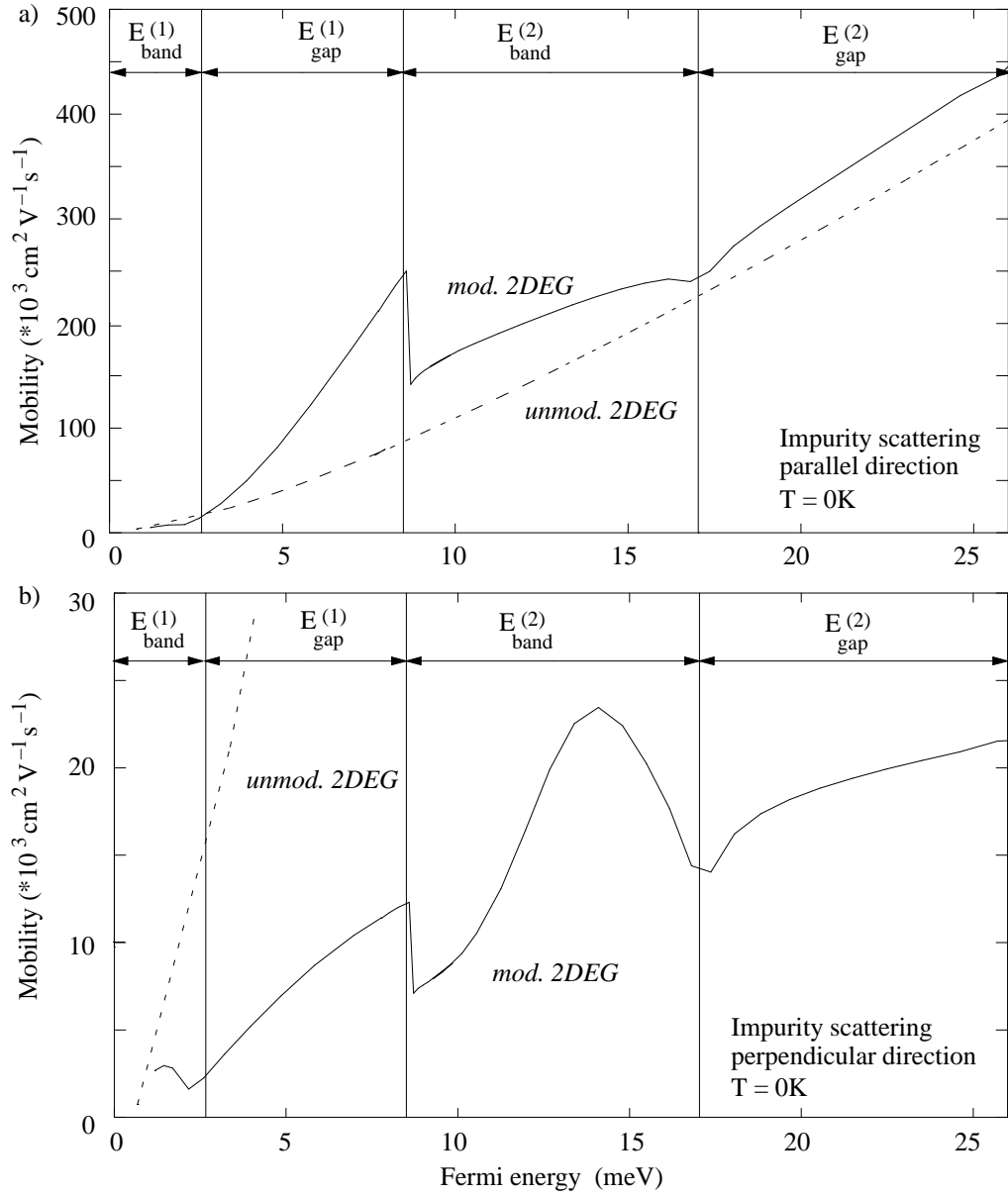


Figure 5.13: Parallel (a) and perpendicular (b) mobility as a function of Fermi energy: As soon as $E_F^0 > E_{band}^{(1)}$, the parallel mobility is strongly enhanced whereas the perpendicular mobility is reduced by a factor of ten with respect to an unmodulated 2DEG. Equally shown is the mobility of an unmodulated 2DEG (dashed line).

The different energy ranges $E_F^0 \in E_{band}^{(1)}$, $E_F^0 \in E_{gap}^{(1)}$, $E_F^0 \in E_{band}^{(2)}$ and $E_F^0 \in E_{gap}^{(2)}$ of Fig. 5.13 shall be discussed:

- $E_F^0 \in E_{band}^{(1)}$
 The parallel and perpendicular mobilities are similar to the one of an unmodulated 2DEG, if the Fermi energy is in the energetical lower part of the first miniband, since the Fermi surfaces of an unmodulated and modulated 2DEG are similar in this energy range. As the Fermi energy approaches the first minigap, two effects become important:
 a) The density of states increases drastically, leading to an enhanced scattering probability and thus to a reduction of the mobility.
 b) Due to the distortion of the Fermi surface, when the Fermi energy approaches the first minigap, the parallel velocity component increases while the perpendicular velocity component decreases. This explains, why the decrease in the perpendicular mobility (Fig. 5.13.b) is stronger than the decrease of the parallel mobility (Fig. 5.13.a).
- $E_F^0 \in E_{gap}^{(1)}$
parallel direction:
 The mobility increases drastically with respect to an unmodulated 2DEG. This is due to the flattening of the Fermi surface. As a the consequent, the scattering angle $\theta_{\vec{v}_{\vec{k}}}$ decreases: $\theta_{\vec{v}_{\vec{k}}} < \theta_{\vec{k}}$ for scattering processes taking place in the first miniband.

perpendicular direction:
 The most striking feature is that the mobility barely increases with increasing Fermi energy (e.g. for the chosen parameters about ten times less than for an unmodulated 2DEG). This is mainly due to the flattening of the minigaps and thus the reduction of the perpendicular velocity component.
- $E_F^0 \in E_{band}^{(2)}$
 As the Fermi energy enters the second miniband, a step function like decrease appears in the parallel as well as in the perpendicular mobility: this is related to the step like increase of the density of states [Cole 77]. Because of the increase of the density of states, the scattering time and consequently the mobilities diminish, when the Fermi energy enters the second miniband. As the Fermi energy increases, the "lenses" of the Fermi surface, corresponding to the second miniband become greater, leading to the increase of the mobility attached to the states of the

second miniband. This increase of mobility has thus the same physical origin as the mobility increase which is seen in an unmodulated 2DEG. However, as the Fermi energy increases, another effect (besides the increase of the density of states) becomes more important and finally dominant: the umklapp process (e.g. backscattering process), leading to a new decrease of the perpendicular mobility. A detailed explanation is given in 5.4.4.

- $E_F^0 \in E_{gap}^{(2)}$

parallel direction:

Once the Fermi energy enters the second minigap, the umklapp processes are reduced for the parallel direction. The parallel mobility follows basically the one of an unmodulated 2DEG. As the Fermi energy increases, the Fermi surface become flatter, resulting in an increase of the mobility.

perpendicular direction:

Oppositely, the perpendicular mobility increases barely. This is understandable by looking on Fig. 5.14. The first and second miniband are close to each other and interminiband scattering becomes important. They are the most important for states $k_{\perp} \sim \pi/L_{\perp}$, because for these states the minibands are close in the k - space and hence only a small scattering vector is necessary. These interminiband scattering processes become more important with increasing Fermi energy. As sketched in Fig. 5.14, these scattering processes involve a large scattering angle $\theta_{\vec{q}}$. Consequently, the perpendicular mobility remains low.

Having gained an understanding of the general behavior of the mobility of a modulated 2DEG for scattering potential, which favors small angle scattering, it shall now be looked on the mobility of a modulated 2DEG for a scattering potential, which favors rather large angle scattering processes.

5.4.2 Large Angle Scattering Potential

As it has been previously shown (Fig. 5.8), the probability is maximum for a scattering vector $q = 2k_F$, resulting in an averaged $q \sim k_F$. Moreover, it shall be reminded that the screened alloy scattering potential (which enters in the scattering matrix elements) does have a scattering vector dependence due to the \vec{q} - dependent dielectric function. Especially, the scattering probability

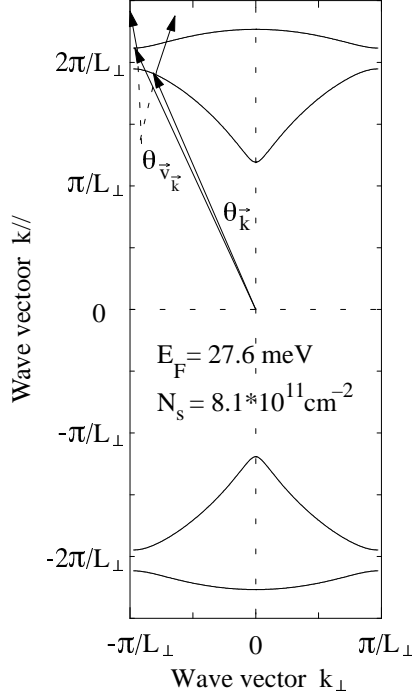


Figure 5.14: *Fermi surface corresponding to the position of the Fermi energy in the second minigap. For states vicinal to $k_{\perp} = \pi/L_{\perp}$, interminiband scattering becomes important.*

for the screened alloy scattering potential goes to zero as q goes to zero (due to the divergence of the dielectric function for $q = 0$).

Regarding the parallel and perpendicular mobility (Fig. 5.15) limited by alloy scattering, one finds again special features which are due to the behavior of the density of states:

- $E_F^0 \in E_{band}^{(1)}$
The mobilities decrease as a function of energy as in the case of an unmodulated 2DEG.
- $E_F^0 \in E_{gap}^{(1)}$
Interestingly, the parallel and perpendicular mobility have an opposite behavior: whereas the parallel mobility increases as the Fermi energy increases, the perpendicular mobility decreases. This is again due to the flattening of the part of the Fermi surface, corresponding to the first

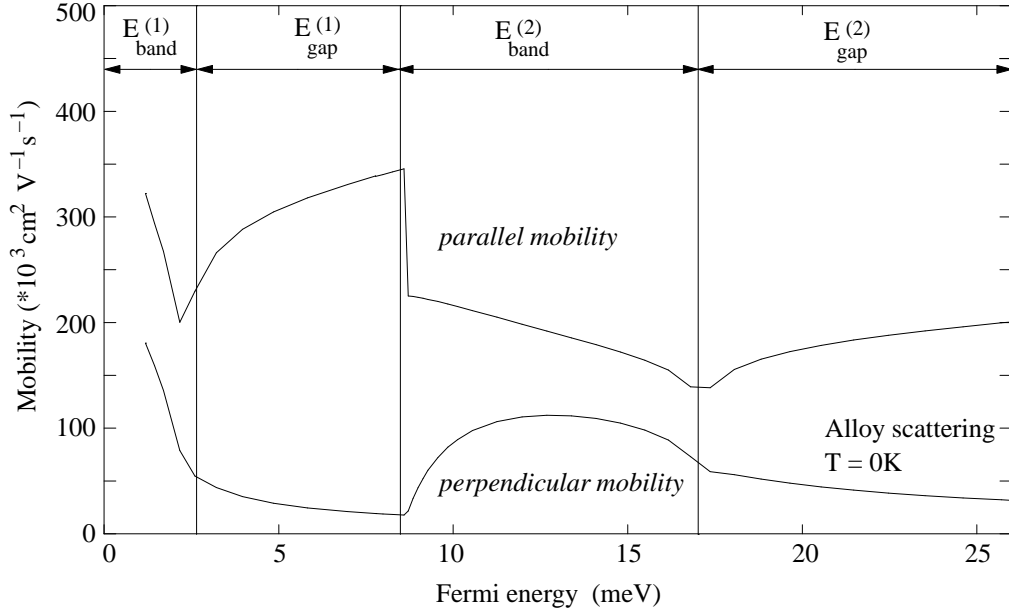


Figure 5.15: *Parallel and perpendicular mobility of a modulated 2DEG limited by alloy scattering as a function of Fermi energy: The mobilities are not a monotonously decreasing function of energy (in contrast to a 2DEG behavior).*

miniband. Consequently, the parallel velocity component is increased, whereas the perpendicular velocity component is decreased.

- $E_F^0 \in E_{band}^{(2)}$

In this energy range, the mobility behavior is reversed: whereas the parallel mobility decreases, the perpendicular mobility increases in the lower part of the second miniband. As the Fermi energy increases, the perpendicular mobility saturates and then decreases.

The decrease of the parallel mobility is the same as seen in an unmodulated 2DEG. The perpendicular mobility increases due to the "lenses" which are now seen in the Fermi surface, corresponding to the second minibands and increasing the averaged perpendicular velocity component.

- $E_F^0 \in E_{gap}^{(2)}$

The mobilities have about the same behavior as in the first minigap due to the same physical reason.

Summarizing the general behavior of the mobility limited by remote ionized impurity scattering and limited by alloy scattering, one notices the following effects: The mobility decreases, as the Fermi energy approaches a minigap. As the Fermi energy enters a miniband, e.g. the second one, a step like decrease of the mobility is seen ² The reason is given by the low mobility and hence the small discontinuity. These characteristics are due to the dependence of the density of states (e.g. due to the van Hove singularities) and are sometimes called "w" - structure [Matheson 82]. Moreover, the perpendicular mobility shows special features, i.e. it decreases, when the Fermi energy approaches the second minigap. These special features are now analyzed by comparing the mobilities with the one, when having changed one parameter (e.g. the angle, the form and magnitude of the lateral potential modulation or taking higher subbands into account, when calculating the dielectric function).

5.4.3 Scattering Angle $\theta_{\vec{v}_{\vec{k}}}$ "against" $\theta_{\vec{k}}$

The parallel and perpendicular mobility limited by ionized impurity scattering (Fig. 5.16) are shown as a function of Fermi energy, once taking the scattering angle $\theta_{\vec{k}}$ (the corresponding mobility will be referred to as $\mu(\theta_{\vec{k}})$) and once the angle $\theta_{\vec{v}_{\vec{k}}}$ between the group velocities of the states \vec{k} and \vec{k}' ($\mu(\theta_{\vec{v}_{\vec{k}}})$, respectively).

This allows to evaluate the difference on the mobility arising from the choice of angle, which shall be pointed out in the following.

- $E_F^0 \in E_{band}^{(1)}$
There is no significant difference between the two calculated mobilities, in agreement with the corresponding energy surface, which is in this energy range basically a circle, e.g. $\theta_{\vec{v}_{\vec{k}}} = \theta_{\vec{k}}$.
- $E_F^0 \in E_{gap}^{(1)}$
A significant difference on the slopes between the two curves becomes obvious. Taking the angle $\theta_{\vec{v}_{\vec{k}}}$, the mobility increases (in the parallel and perpendicular direction) by a factor 3 faster than taking the angle $\theta_{\vec{k}}$. This is due to the flattening of the Fermi surface and thus the "aligning" of the group velocities in the parallel direction, e.g. $\theta_{\vec{v}_{\vec{k}}} < \theta_{\vec{k}}$.

²In the perpendicular mobility limited by alloy scattering, the discontinuity is not seen because a) the discontinuity is small due to the low mobility and b) the mobility has not been calculated exactly for the onset of the second miniband, i.e. $E_F^0 = E_{band}^{onset(2)}$.

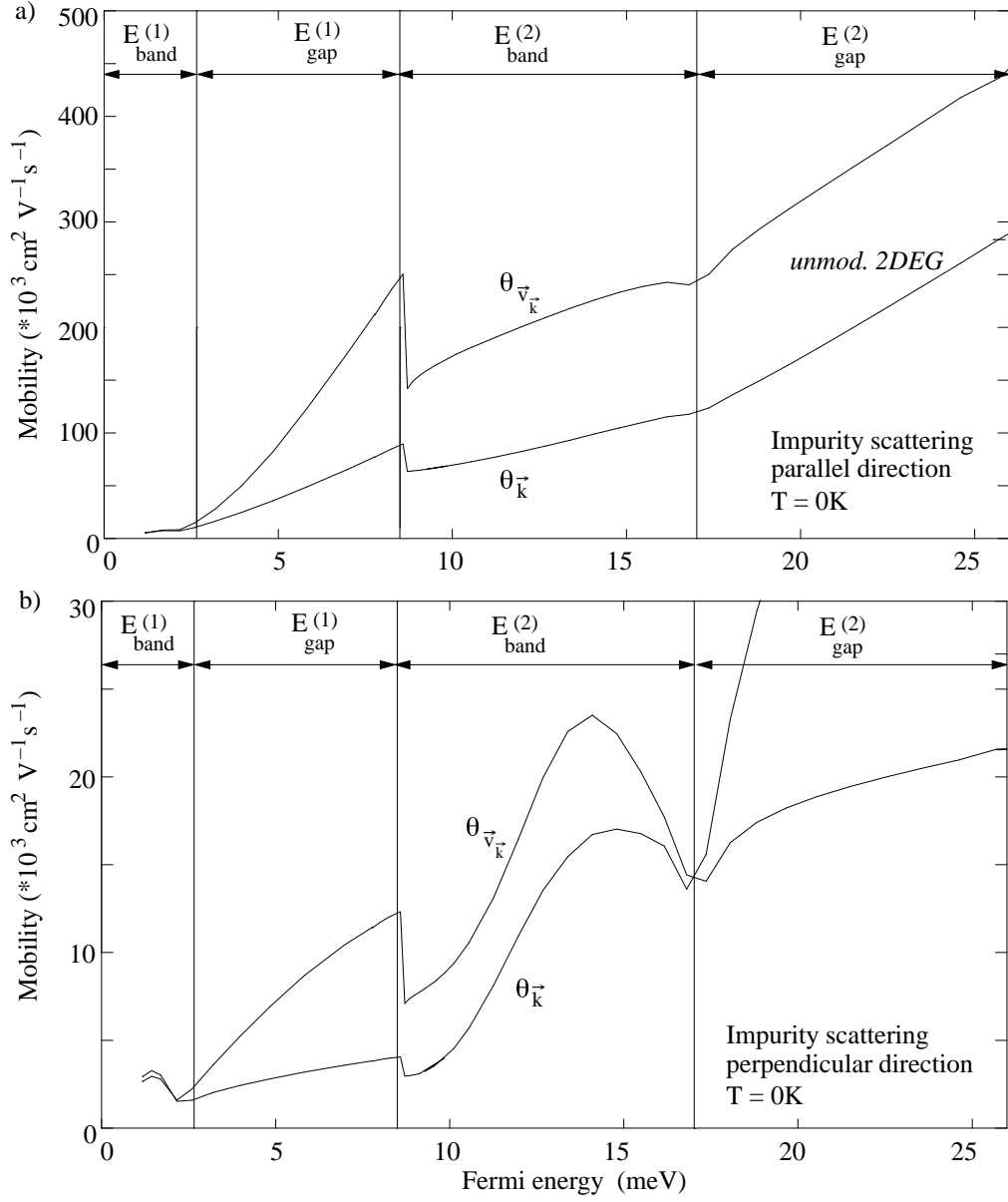


Figure 5.16: Parallel (a) and perpendicular (b) mobility as a function of Fermi energy for impurity scattering, once taking the scattering angle $\theta_{\vec{v}_{\vec{k}}}$, once $\theta_{\vec{k}}$: The parallel mobility $\mu(\theta_{\vec{v}_{\vec{k}}})$ is superior to the mobility $\mu(\theta_{\vec{k}})$ in the entire energy range. The perpendicular mobility $\mu(\theta_{\vec{v}_{\vec{k}}})$ is superior if $E_F^0 < E_{gap}^{(2)}$, whereas it is inferior with respect to $\mu(\theta_{\vec{k}})$, if the Fermi energy is in the second minigap.

- $E_F^0 \in E_{band}^{(2)}$

The discontinuity, which appears as the Fermi energy enters the second miniband, is more pronounced in the mobility curves $\mu(\theta_{\vec{q}_k})$ than in the mobility curves $\mu(\theta_{\vec{k}})$. This demonstrates the effect of the appearing "lenses" (see Fig. 5.12). Since the curvature of these "lenses" is stronger with respect to the Fermi surface of an unmodulated 2DEG, the angle $\theta_{\vec{q}_k}$ is greater than $\theta_{\vec{k}}$. As the Fermi energy increases, the mobility $\mu(\theta_{\vec{q}_k})$ increases with about the same slope as in the case of an unmodulated 2DEG, whereas the mobility $\mu(\theta_{\vec{k}})$ has a slower increase. This is mainly due to the states $\vec{k} = (k_{\parallel} \sim 0, k_{\perp})$: The k attributed to these states are smaller in comparison to the k attached to the Fermi surface of an unmodulated 2DEG. Hence for a given scattering vector \vec{q} , the scattering angle is in average greater. This effect becomes more important, as the Fermi energy increases (the distance between the "lenses" becomes smaller!), leading to a small increase of the mobility $\mu(\theta_{\vec{k}})$ as a function of Fermi energy. As the Fermi energy approaches the second minigap, other processes, however, become even more important, leading to a new decrease of the mobility: the umklapp processes. They are more important for the mobility $\mu(\theta_{\vec{v}_k})$ than for the mobility $\mu(\theta_{\vec{k}})$ due to the stronger curvature of the part of the Fermi surface belonging to the second miniband ("lenses") with respect to the curvature of a Fermi surface, belonging to an unmodulated 2DEG.

- $E_F^0 \in E_{gap}^{(2)}$

As the Fermi energy enters the second minigap, the umklapp processes disappear progressively: the mobilities assume a similar behavior to the one of an unmodulated 2DEG, except the perpendicular mobility $\mu(\theta_{\vec{v}_k})$: The effect of the opening of the second minigaps leads to inter-miniband scattering with great scattering angle (see also Fig. 5.14).

Regarding now the parallel and perpendicular mobility limited by alloy scattering (Fig. 5.17), one practically does not observe any difference. This is due to the characteristic of a large angle scattering potential: The Fermi surface is often crossed (the average scattering vector \vec{q} is in the order of \vec{k}_F). This explains why one does not see any signatures of the local change of the Fermi surface in the mobility curves, e.g. $\mu(\theta_{\vec{k}}) \sim \mu(\theta_{\vec{v}_k})$.

The partial conclusion can be drawn, that choosing $\theta_{\vec{v}_k}$ instead of $\theta_{\vec{k}}$ contributes to the enhancement of the anisotropy of the mobility μ_{\parallel} and μ_{\perp} in the case of a long range scattering potential. However, from a theoretical

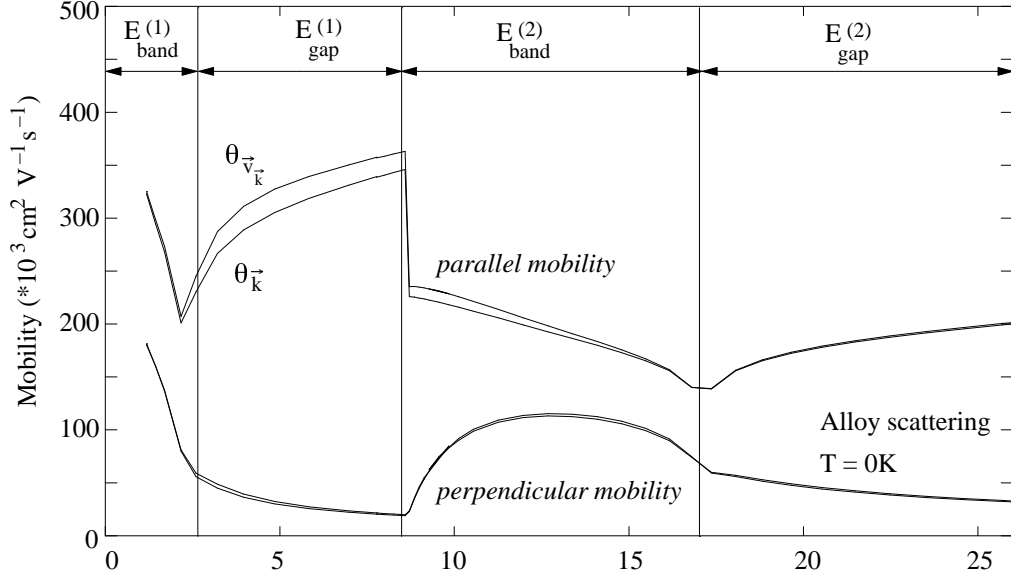


Figure 5.17: *Parallel and perpendicular mobility as a function of Fermi energy for alloy scattering, once having taken the scattering angle $\theta_{\vec{v}_{\vec{k}}}$, once $\theta_{\vec{k}}$: Due to a rather great averaged scattering vector \vec{q} , there is no difference between the two scattering angles.*

point of view, the choice of the angle remains an open question [Ziman 61].

5.4.4 Impact of the Second Fourier Coefficient

In this section it is discussed, how the second Fourier coefficient of the lateral potential modulation (see also chapter 2.2.2) influences the mobility of a modulated 2DEG. The motivation for this study arises from experimental data: The resistivity in the perpendicular direction increases with a greater slope than for an unmodulated 2DEG as a function of temperature. To explain these results, scattering processes are needed, which strongly change the group velocity of the perpendicular direction of the participating states. As it will be shown, such scattering processes are introduced by the second Fourier coefficient.

The inclusion of the second Fourier coefficient in the band structure calculation has two related, but nevertheless different effects:

1. Modification of the bandstructure (e.g. flattening of the Fermi surface).

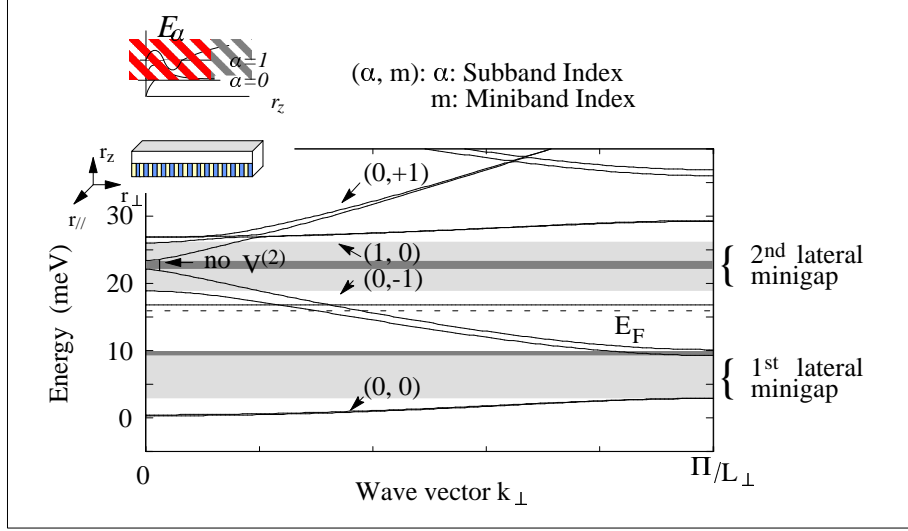


Figure 5.18: *Bandstructure of a modulated 2DEG, once taking one Fourier coefficient in the bandstructure calculations, once taking higher Fourier components into account. Taking $V^{(2)}$ into account, results in a larger second miniband and a flattening of the second and third miniband.*

2. Introduction of umklapp processes which involve two reciprocal lattice vectors.

These two effects shall be detailed in the following.

In Fig. 5.18, the bandstructures of modulated 2DEG's, once assuming a sinusoidal potential modulation and once including a second Fourier component are shown.

Without a second Fourier component, the second miniband is small ($E_g^{(2)} = 1.3$ meV) and consequently one has a greater energy dispersion of the second miniband with respect to the case where the second Fourier coefficient is included in the band structure calculations: in this case, one introduces an energy gap, comparable to the first energy gap ($E_g^{(2)} = 9.5$ meV). Hence, the second miniband becomes almost dispersionless with respect to the second miniband calculated by including only one Fourier coefficient. This results also in a difference of the corresponding Fermi surfaces: The "lenses" of the second miniband belonging to the band structure calculations having included the second Fourier component are closer at a given Fermi energy (due to the less dispersive second miniband). How this fact contributes to the enhancement of the scattering probability is explained next.

As discussed in chapter 3.7, the scattering matrix element is written the following:

$$|\langle \varphi_{\mathbf{k}} | V_{diff} | \varphi_{\mathbf{k}'} \rangle|^2 = \sum_{q,p,m} \left[\langle V^{diff}(q, r_z) \rangle_{\zeta(r_z)} \right]^2 [a_p(k_{\perp}) a_{p+m}(k'_{\perp})]^2 \delta(k'_{\parallel} - k_{\parallel} - q_{\parallel}) \delta(k'_{\perp} - k_{\perp} - q_{\perp} + m * \frac{2\pi}{L_{\perp}})$$

It shall be reminded, that the wave functions $\varphi_{\mathbf{k}}$ are written in the form $\varphi_{\mathbf{k}}(\vec{R}) = (1/\sqrt{A}) \exp(ik_{\parallel}r_{\parallel} + k_{\perp}r_{\perp}) \sum_{n,p} a_{n,p}(k_{\perp}) \exp[i2p\pi r_{\perp}/L_{\perp}] \zeta_{\alpha}(r_z)$, with $p = 0, \pm 1, \dots$ and $\zeta_{\alpha}(r_z)$ the wave functions corresponding to the electrical subbands of the same structure but unmodulated. The amplitudes $a_p(k_{\perp})$ are obtained from the self-consistent band structure calculations, as discussed in chapter 2.2.3. Without modulation, the only non-zero amplitude is that corresponding to the miniband index. The important feature is now that with a lateral potential modulation, each Fourier component $V^{(p)} (= V^{(-p)})$ couples states of same wavevector but belonging to minibands with indexes differing by $\pm p$ (see Fig. 5.18) by the rule $-m - m' = p$ (m, m' are the miniband indexes).

Fig. 5.19 shows an example for the Fermi surface when the Fermi energy is close to the second minigap. The most important scattering process which reduces the perpendicular mobility are given by backward scattering between the parts of the Fermi surface, corresponding to the miniband (-1) and (+1) around $k_{\parallel} = 0$. Such scattering processes (umklapp processes) are only allowed by the second Fourier component. The scattering vector is small (see Fig. 5.19, $\vec{q} = 2 \vec{k}_F - 4\pi/L_{\perp}$). Since the remote ionized impurity scattering favors small angle scattering, the process is highly probable, leading to a decrease of the perpendicular mobility as the Fermi energy approaches the second minigap.

The importance of the contributions of these states $\vec{k} = (k_{\parallel} \sim 0, k_{\perp})$, belonging to the extremities of the second miniband are nicely demonstrated in Fig. 5.20. The transport time $\tau(\vec{k})$ for remote ionized impurity scattering is calculated for each \vec{k} -state at $T = 0K$, once with and once without the second Fourier coefficient: While there is no difference in the first miniband, an important difference becomes apparent for states, belonging to the second miniband. The transport time diminishes, when including the second Fourier coefficient in the bandstructure calculations, reflecting the importance of the umklapp processes.

In order to differentiate between the effects which arise from the deviations of the Fermi surface (e.g. flattening of the parts corresponding to the

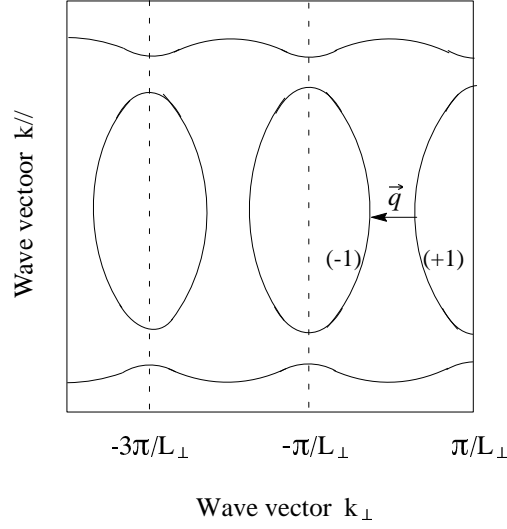


Figure 5.19: *Sketch of the scattering vector, involved in the scattering processes between states belonging to miniband (-1) and states belonging to (+1). These scattering processes are only allowed by the second Fourier coefficient of the lateral potential modulation.*

first miniband and stronger curvature of the parts corresponding to the second miniband) and those which are due to the umklapp processes, induced by the second Fourier coefficient, one is led to regard again Fig. 5.16.b, where the perpendicular mobility is shown once while taking the angle $\theta_{\vec{v}_k}$ and once the angle $\theta_{\vec{k}}$. Whereas the mobility $\mu(\theta_{\vec{v}_k})$ contains both effects, e.g. the distortion of the Fermi surface and the modification of the wave functions due to the second Fourier coefficient, the mobility $\mu(\theta_{\vec{k}})$ is barely sensitive to the distortion of the Fermi surface. Accordingly, the decrease of the perpendicular mobility $\mu(\theta_{\vec{k}})$ as the Fermi energy approaches the second energy gap is mainly due to the manifestation of the umklapp processes. The difference between the mobilities $\mu(\theta_{\vec{v}_k})$ and $\mu(\theta_{\vec{k}})$ are due to the distortion of the Fermi surface. It shall be emphasized that these backscattering process play only an important role when one discusses a long range scattering potential, which favors small angle scattering. This is equally documented by the fact that one basically finds no difference between the mobilities $\mu(\theta_{\vec{k}})$ and $\mu(\theta_{\vec{v}_k})$ in the case of alloy scattering.

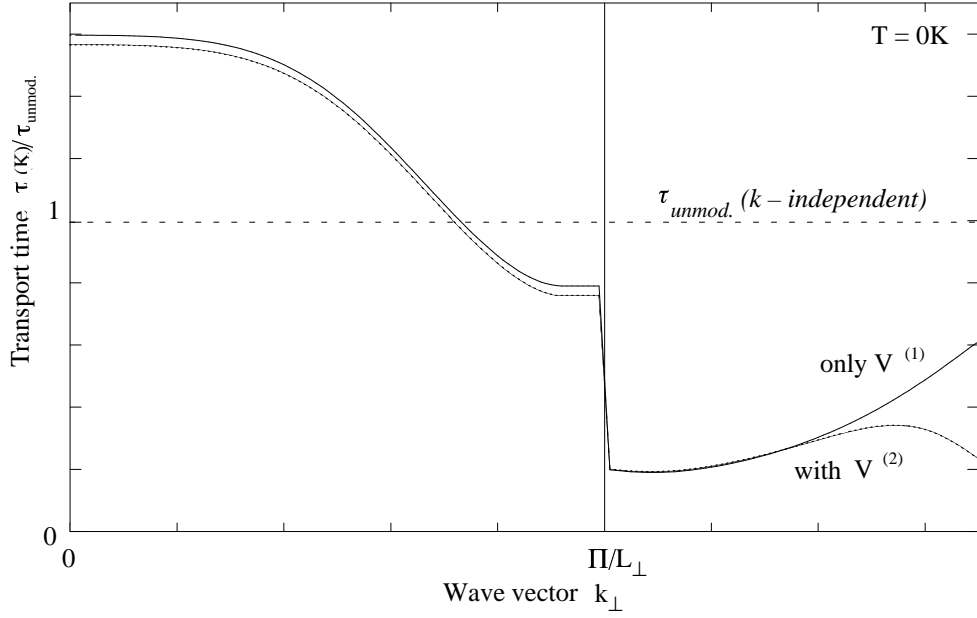


Figure 5.20: *Transport time (normalized to the one of an unmodulated 2DEG) as a function of the wave vector \vec{k}_\perp in extended Brillouin zone, once having included the second Fourier coefficient (solid line), once without (dashed line): The transport time corresponding to the extremities of the second miniband have a reduced transport time, when including the second Fourier coefficient in the bandstructure calculations. This is due to the umklapp processes, induced by the second Fourier component.*

Comparing the difference between a "one subband" or "three subbands" dielectric functions (Fig. 5.21 for the perpendicular mobility limited by remote ionized impurity scattering, taken as example), one does not find a decisive difference between the calculated mobilities, since all these calculations are executed at $T = 0K$ and the Fermi energy remains always inferior to the second subband. To see the interesting effects of the dielectric function, one has to study the mobilities as a function of temperature. This is done in the next section.

5.5 Influence of the Temperature

Experimentally, one remains always at finite temperature. Thus, one questions about the temperature effect on the perpendicular and parallel mobil-

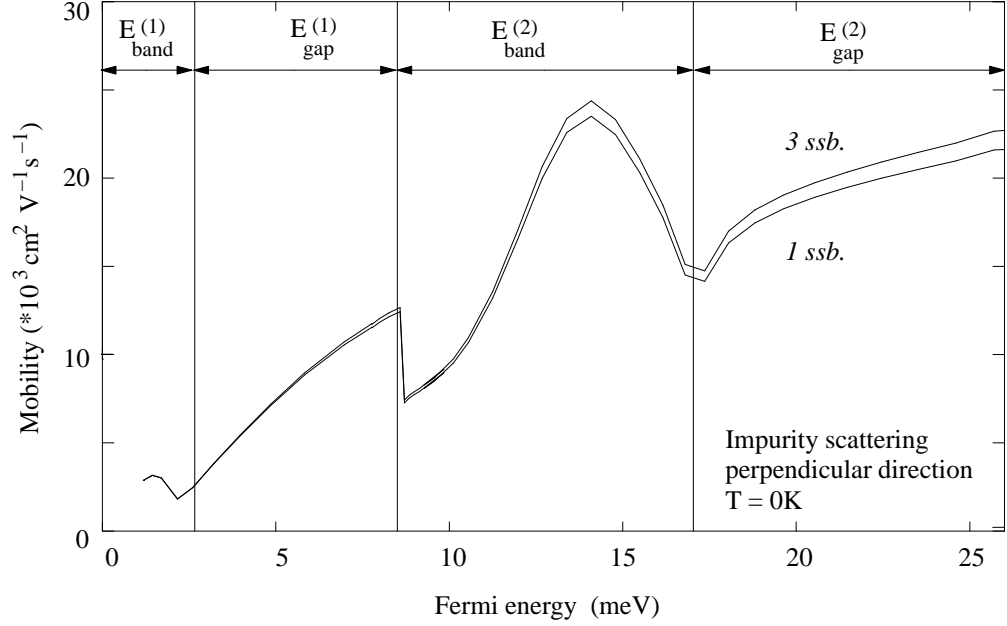


Figure 5.21: *Perpendicular mobility as a function of Fermi energy for remote ionized impurity scattering, including once one and once three subbands in the dielectric function at $T = 0K$. The maximum difference is only 10%: the Fermi energy is always inferior to the second subband energy and the calculation is performed at low temperature.*

ity of a modulated 2DEG. At finite temperature all states within the energy range $E_F \pm 6k_B T$ contribute to the conductivity. One thus has to average the electronic properties by integrating them, weighted by their statistical impact, e.g. $x(E) = \int \frac{\partial g^0}{\partial E} \cdot x(E) dE$. (g^0 is the Fermi - Dirac distribution.)

The averaging of the electronic properties can be regarded as a disadvantage, since it will cause to disappear pronounced structures in the perpendicular and parallel directions, which were analyzed in the previous section. On the other hand, it is interesting to look at the temperature effect on the mobility for a given charge density and to focus on the question how one can find signatures of the lateral minigaps and -bands in the parallel and perpendicular mobility. As will be shown in chapter 6.2.1, taking temperature dependent mobility curves for different charge densities leads to a consistent picture, demonstrating the existence of minigaps and -bands in the perpendicular direction.

In the following the effect of temperature will be again separately dis-

cussed for the remote ionized impurity - and alloy scattering potentials.

5.5.1 Vanishing of the Bandstructure Effects

As intuitively expected, the structures in the mobility curves discussed in the previous section vanish when one raises the temperature. This is shown in Fig. 5.22, where the perpendicular and parallel mobility is shown as a function of Fermi energy for different temperatures. Already at $T = 10\text{K}$, one can only guess the at $T = 0\text{K}$ (and still $T = 4.5\text{K}$) pronounced structures in the mobility curves as a function of Fermi energy. (The small fluctuations around the discontinuity are due to numerical instabilities.)

However, this is only one side of the temperature effect. The other side is that one does expect interesting temperature dependent effects in the parallel and perpendicular mobility. The reason is schematically indicated by the arrows in Fig. 5.22: Depending on the Fermi position at low temperature, the mobility increases or decreases as a function of temperature. Accordingly, one does not expect a monotonous behavior of the mobility as a function of temperature. Remarkably, when the Fermi energy is in the lower part of the second miniband, the parallel mobility decreases as a function of temperature, whereas the perpendicular mobility increases. This different temperature behavior of the mobilities is due to the lateral potential modulation. More precisely, the temperature dependence of the parallel and perpendicular mobility will be determined by the position of the Fermi energy at $T = 0\text{K}$ with respect to the lateral potential modulation (see also Fig. 5.23): Increasing the temperature, means integration over an energy range $E_F \pm 6k_B T$. If the mobility attached to the states within $E_F \pm 6k_B T$ were a linear function of energy, the mobility would remain, in first approximation, constant, since one integrates over the same number of states with enhanced mobility than with reduced mobility. If, however, there is for example a maximum (minimum) in the mobility close to $E_F(T = 0\text{K})$, the mobility will decrease (increase) as the temperature increases. This can be generalized to the following "rule" which will help to explain the results: The temperature **dependence** of the mobility is in first approximation proportional to the second derivative of the mobility with respect to the Fermi energy:

$$\frac{\partial \mu(T)}{\partial T} \sim \frac{\partial^2 \mu(E_F)}{\partial E_F^2} \Big|_{T=0K} \quad (5.10)$$

One can now distinguish between three cases:

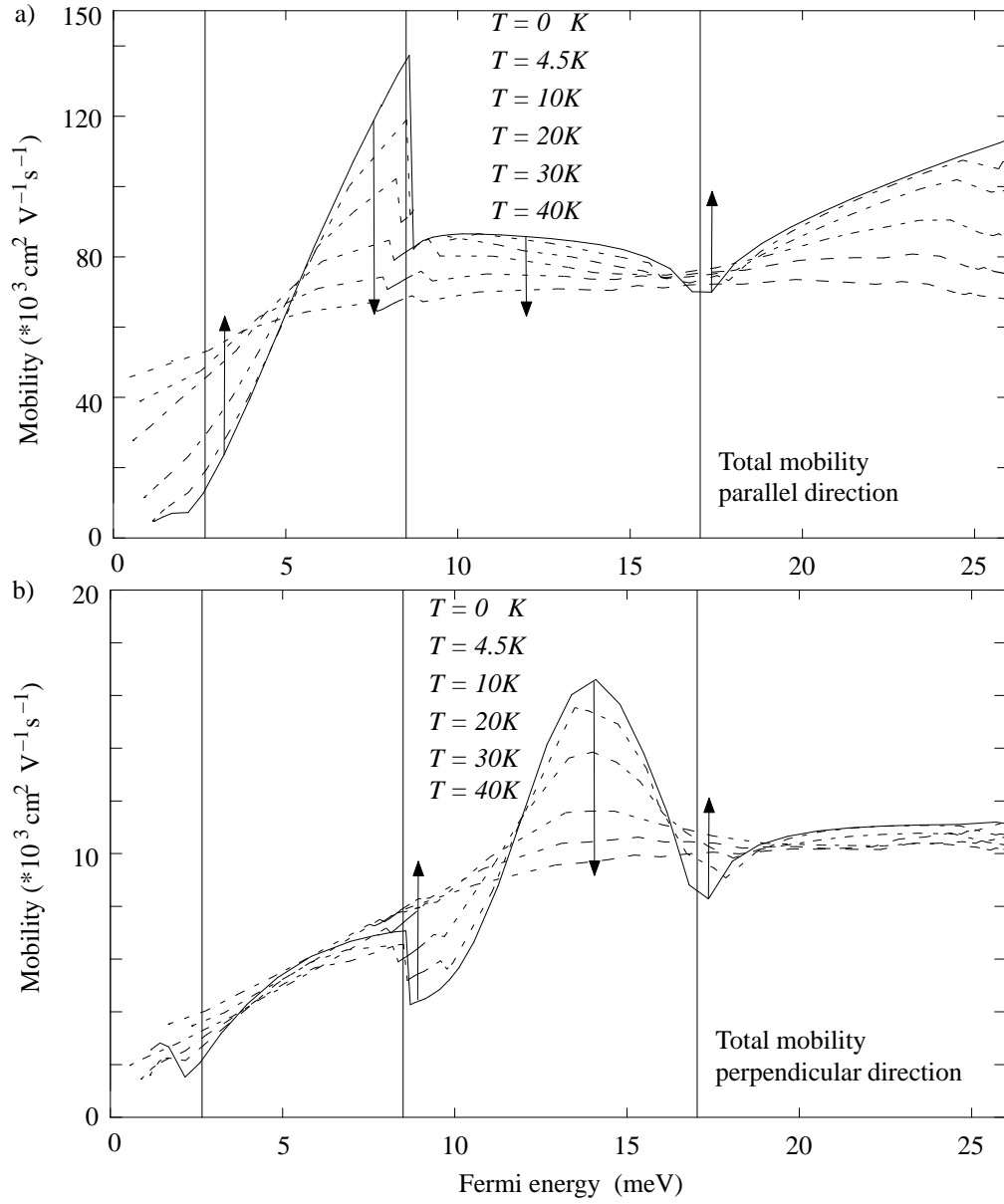


Figure 5.22: Total mobility for the parallel (a) and perpendicular (b) direction as a function of Fermi energy for different temperatures: At higher temperature the specific structures due to the lateral potential modulation vanishes. However, the temperature dependency of the mobilities depends strongly on the Fermi level position as indicated by arrows, leading to special features in the temperature dependent mobilities.

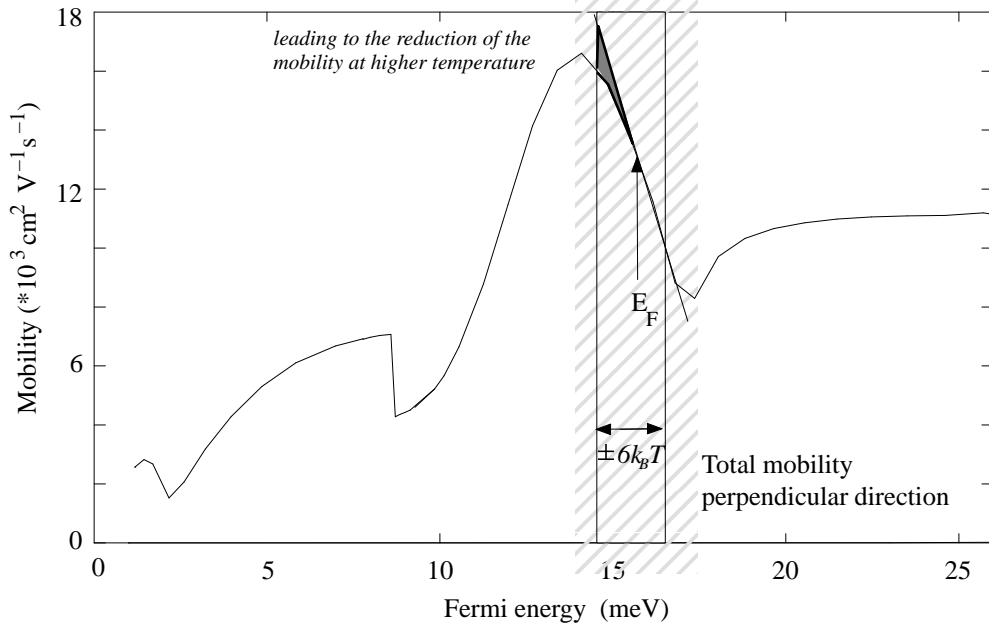


Figure 5.23: Sketch to explain the reduction or increase of mobility as a function of temperature: Having a local maximum (minimum) in the mobility curve as a function of energy, leads to a mobility decrease (increase) when raising the temperature.

- The Fermi position is at $T = 0K$ at (or close to) a (local) maximum:

$$\frac{\partial^2 \mu(E_F)}{\partial E_F^2} \Big|_{T=0K} < 0 \rightarrow \mu(T) \text{ decreases} \quad (5.11)$$

- The Fermi position is at $T = 0K$ at (or close to) a (local) minimum.

$$\frac{\partial^2 \mu(E_F)}{\partial E_F^2} \Big|_{T=0K} > 0 \rightarrow \mu(T) \text{ increases} \quad (5.12)$$

- The Fermi position is at $T = 0K$ at (or close to) an insertion point.

$$\frac{\partial^2 \mu(E_F)}{\partial E_F^2} \Big|_{T=0K} = 0 \rightarrow \mu(T) \text{ constant.} \quad (5.13)$$

In the following, the temperature dependent mobility shall be investigated for different positions of the Fermi energies. It allows to get insight in the temperature dependent features of the mobilities and how they can be attributed to the lateral potential modulation. The above established "rule" will be the basis of the explanations.

5.5.2 Mobility as a Function of Temperature

First the temperature dependent mobility is calculated for three different charge densities, e.g. for different positions of the Fermi level with respect to the lateral potential modulation. In these calculations, the temperature dependence of the bandstructure is taken into account, e.g. for each temperature the band structure is recalculated, as well as the second Fourier component and three subbands in the dielectric function are included. In a second step, these calculations are again compared to other calculations, in which one parameter is systematically changed.

The three charge densities are chosen as follows (see Fig. 5.24): At $T =$

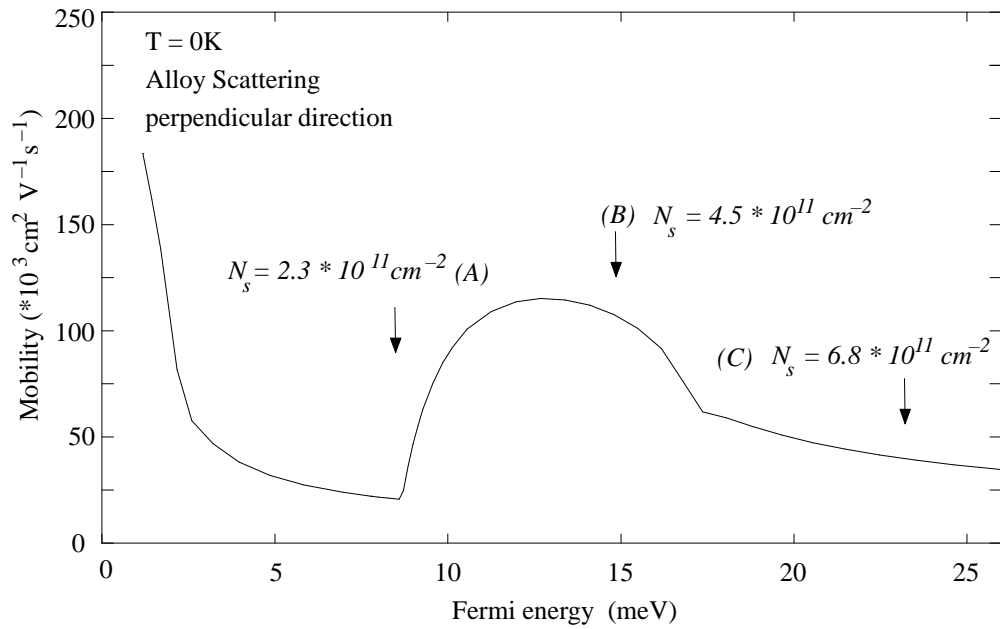


Figure 5.24: *Indication of the Fermi level at $T = 0K$ with respect to the lateral potential modulation for three different charge densities. For these charge densities the mobility as a function of temperature will be discussed.*

0K, once the Fermi energy is just on the top of the first minigap (A), once in the middle of the second miniband (B) and once in the second minigap (C). In Fig. 5.25 the parallel and perpendicular mobility as a function of temperature for remote ionized impurity scattering is shown. Interesting features are seen in the parallel and perpendicular mobility as a function of temperature:

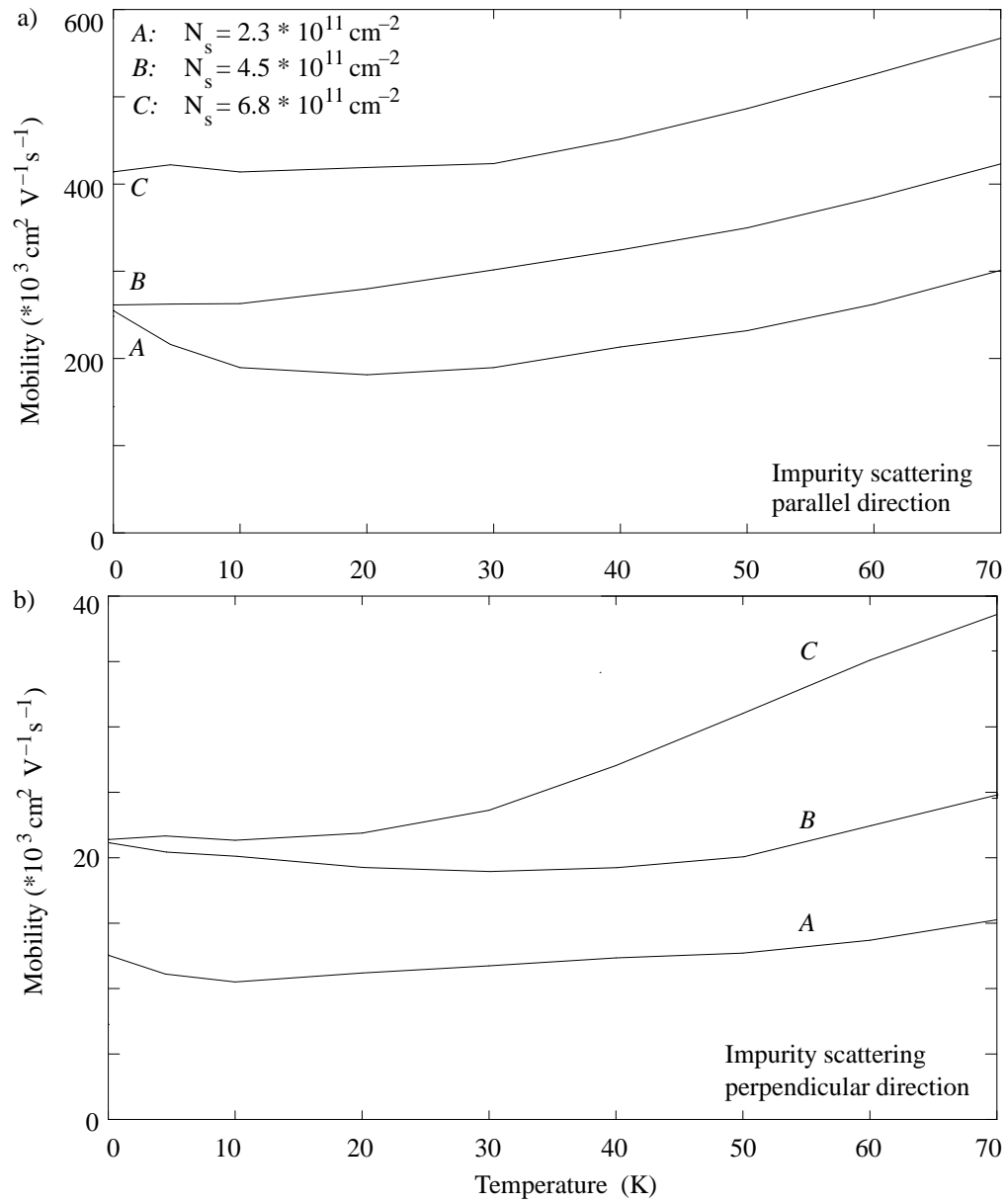


Figure 5.25: *Parallel mobility (a) and perpendicular mobility (b) for ionized impurity scattering as a function of temperature for three different charge densities: the temperature dependent behavior of the mobilities depend strongly on the position of the Fermi energy at $T = 0\text{K}$.*

- Curves A:
The parallel and perpendicular mobility decreases in the beginning of temperature increase. This feature is more accentuated in the parallel mobility. At higher temperature, the mobilities increase.
- Curves B:
While the parallel mobility increases as a function of temperature, the perpendicular mobility decreases slightly for $T < 50\text{K}$. For $T > 50\text{K}$, the perpendicular mobility equally increases.
- Curves C:
The parallel and perpendicular mobility remains constant and increases at higher temperature. This increase is in the perpendicular direction strong in comparison to the mobility curves corresponding to the other charge densities.

Regarding the mobility curves limited by alloy scattering as a function of temperature, even more pronounced features are seen:

- Curves A:
While the parallel mobility decreases monotonously as a function of temperature, the perpendicular mobility increases first as a function of temperature and remains then constant (in the considered temperature range).
- Curves B:
While the parallel mobility remains in first order constant, the perpendicular mobility decreases as a function of temperature.
- Curves C:
While parallel mobility decreases as a function of temperature, the perpendicular mobility increases slightly.

As explained in the beginning, the temperature dependence of the mobility can be predicted from the position of the Fermi energy on the "Mobility - Fermi energy curve at $T = 0\text{K}$ (see also Fig. 5.24). This is as an example demonstrated for the perpendicular mobility limited by alloy scattering, but is equally valid for the parallel direction and for the mobilities limited by remote ionized impurity scattering:

- Curve A:
At $T = 0\text{K}$, the position of the Fermi energy (corresponding to the

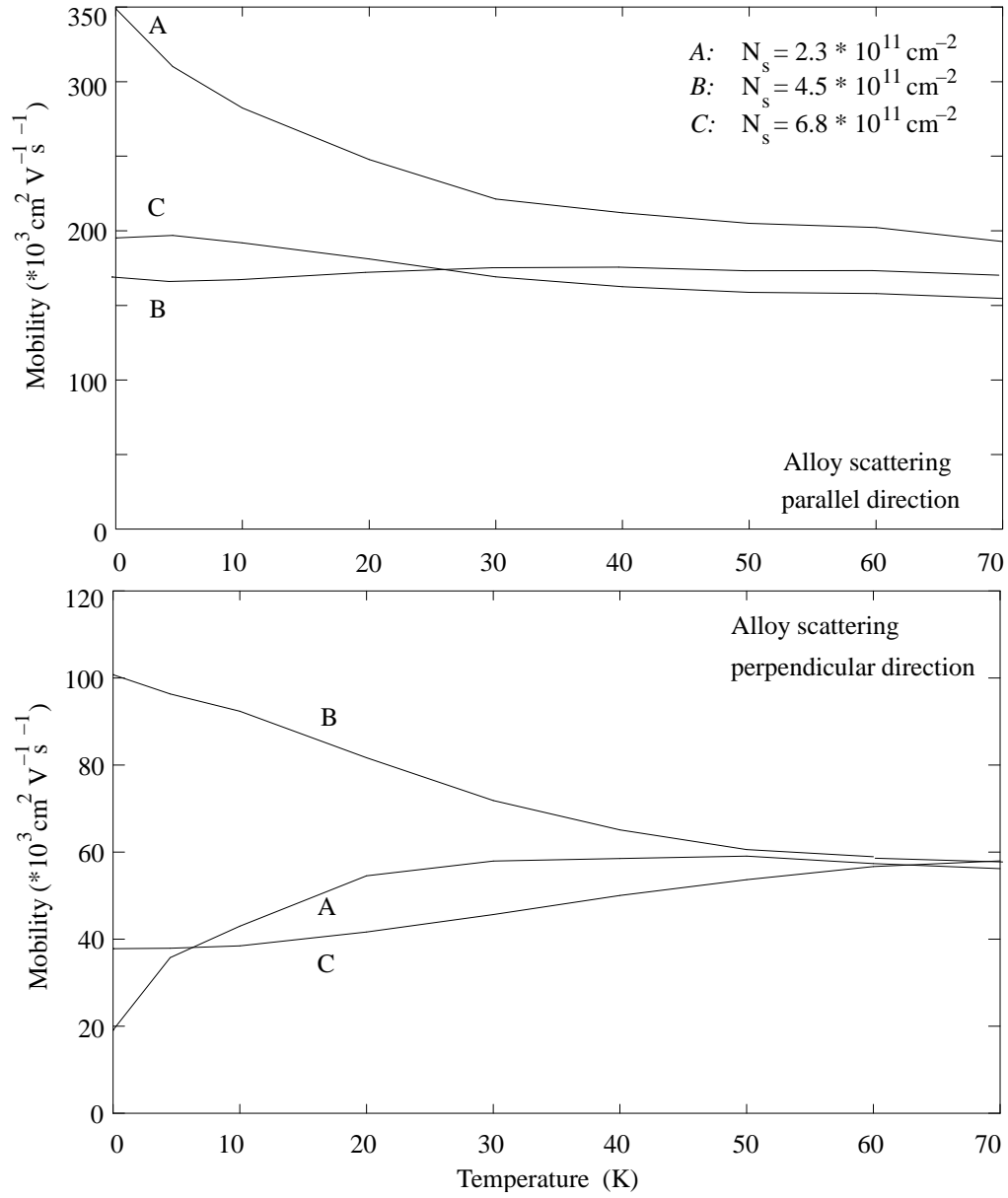


Figure 5.26: Parallel (a) and perpendicular (b) mobility for alloy scattering as a function of temperature for three different charge densities. The different temperature behaviors are discussed in the text.

charge density of curve A) corresponds to a local minimum in the mobility - Fermi energy curve. This leads to an increase of the mobility as the temperature increases.

- Curve B:

At $T = 0\text{K}$, the position of the Fermi energy (corresponding to the charge density of curve B) is close to a maximum in the mobility - Fermi energy curve. This leads to a decrease of the mobility as the temperature increases.

- Curve C:

At $T = 0\text{K}$, the position of the Fermi energy (corresponding to the charge density of curve C) corresponds to a plateau. Hence, in first approximation, the mobility remains constant, as one increases the temperature.

Inclusion of the second Fourier coefficient As already discussed, the second Fourier coefficient broadens significantly the second minigap (accompanied with the warping of the Fermi surface when the Fermi level is close to the second minigap) and enhances the number of scattering processes. At $T = 0\text{K}$, its most important impact has been seen on the perpendicular mobility, when the Fermi energy is in the second miniband.

In the following, two different types of calculations will be presented: once, only the first Fourier coefficient of the lateral potential modulation is included and once a second Fourier coefficient (keeping the first one constant) is added.

Regarding the parallel mobility as a function of temperature (Fig. 5.27) for the three different charge densities (Fig. 5.24), the temperature behavior of all curves is quite similar. The difference between including one or two Fourier coefficients in the bandstructure calculations, expresses itself basically in a shift of the different mobility values.

Looking on the perpendicular direction, one assumes to see more pronounced features due to the lateral potential modulation - but only if the Fermi energy is in the second miniband.

- Curve A:

There is no significant difference between the mobility curves, having taken one or two Fourier coefficients into account. This reflects the fact that the inclusion of the second Fourier coefficient becomes only

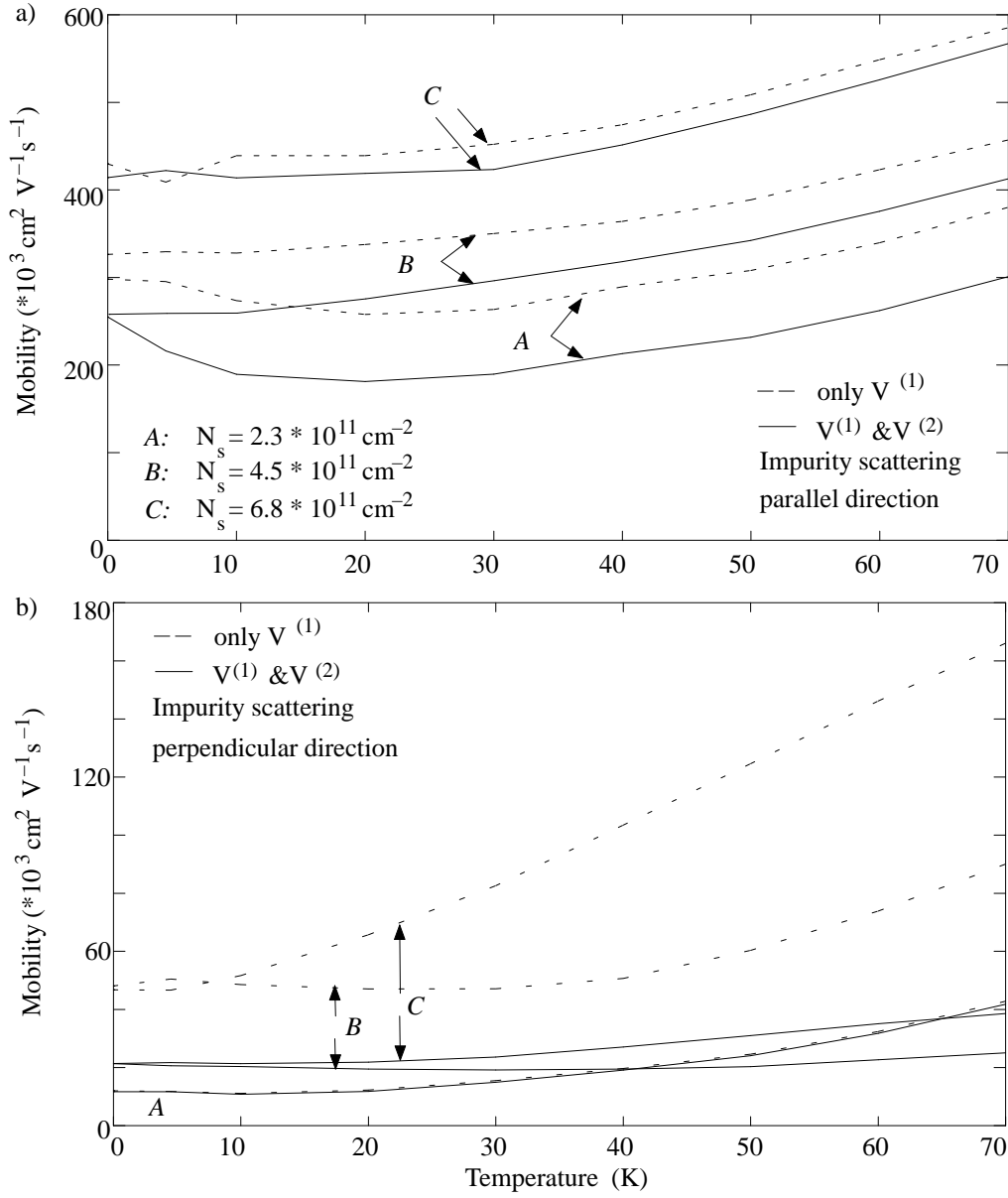


Figure 5.27: *Parallel (a) and perpendicular (b) mobility for ionized impurity scattering as a function of temperature for the three different charge densities, once having included the second Fourier coefficient and once considering a sinusoidal lateral potential: While there is no fundamental difference in the parallel direction, a difference for the perpendicular mobility becomes apparent for higher charge densities.*

important for higher charge densities, e.g. if the Fermi energy is in the upper part of the second miniband.

- Curve C and D:

Remarkably differences are seen for these two curves in the mobility values as well as in the temperature dependence: If one does not include the second Fourier coefficient, the mobility values at low temperature assume more than the double.

Additionally and even more exciting for the experimental detection of the existence of minigaps are the different slopes between the mobilities, when taking the second Fourier coefficients into account or neglecting them: Taking the first Fourier coefficient into account, the mobility increases by about a factor 3 between 0 K and 70 K with respect to a factor 2 when taking the first two Fourier coefficients into account.

Inclusion of higher subbands in the dielectric function Already in the case of an unmodulated 2DEG, the consequence of including higher subbands in the dielectric function was demonstrated: as soon as the temperature is high enough to integrate over states belonging to the second subband, the calculated mobility is higher when including higher subbands in the dielectric function. Moreover, it was pointed out that the difference between the calculated dielectric function (when including one or more than one subband) becomes the more important the smaller the scattering vector is (see also section 5.1). Consequently, one assumes that the effect of the dielectric function is especially important for remote ionized impurity scattering, since it is a scattering potential which favors small scattering vectors.

In Fig. 5.28 the temperature dependent parallel and perpendicular mobility, once while including one subband, when calculating the dielectric function, once while taking the three lowest subbands into account, are shown for different charge densities. As expected, the effect is more important for higher charge density and higher temperature is. For completeness, the mobilities limited by alloy scattering as a function of temperature are equally shown (Fig. 5.29), once having taken one subband, and once having included three subbands in the dielectric function. Once again, the difference is more important at higher temperature. However, the effect is much smaller in comparison to the one seen for the remote ionized impurity potential. This is due to the fact that the effect of taking higher subbands into account when calculating the dielectric function is more important for smaller scattering vector \vec{q} as discussed in chapter 5.1.

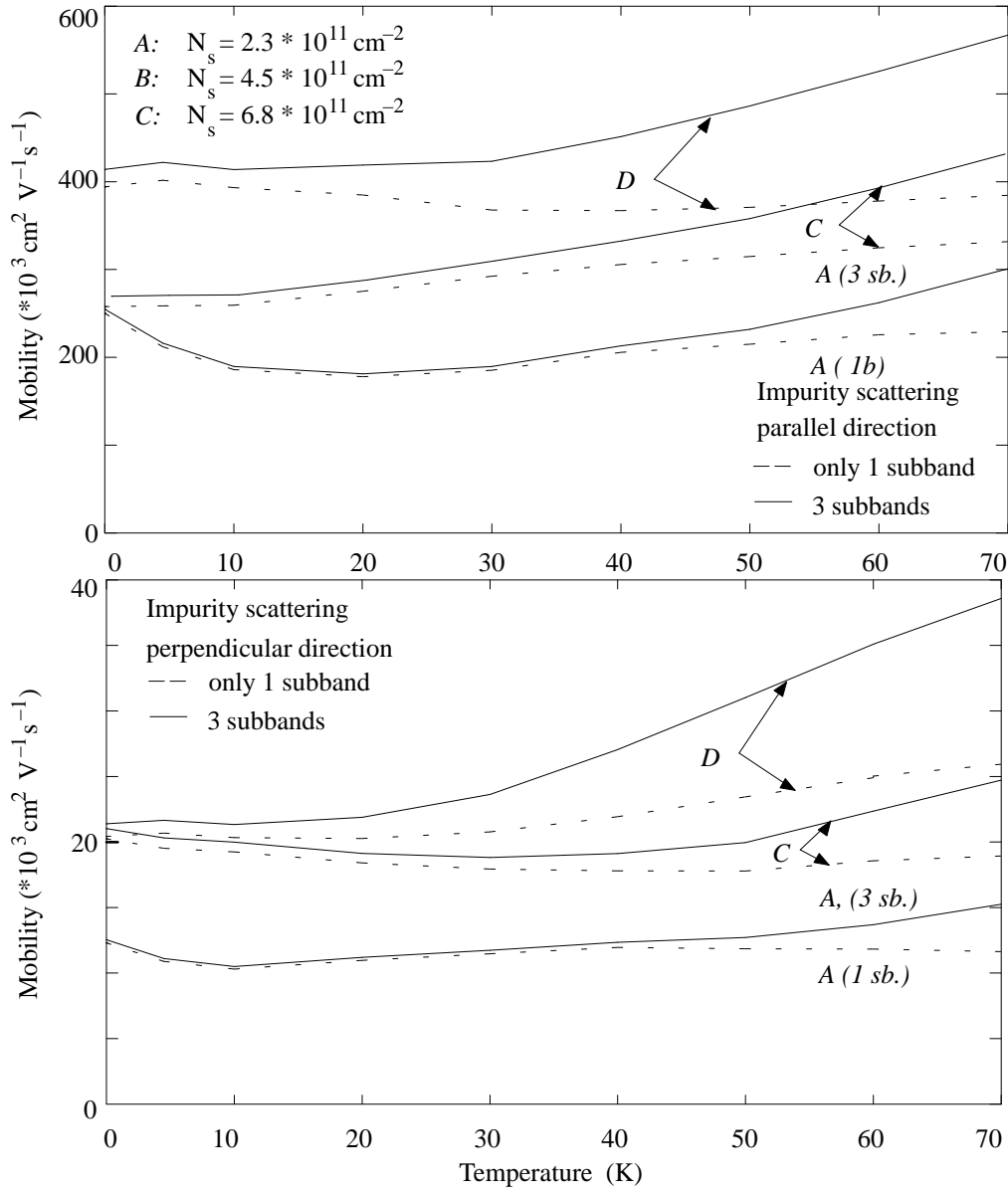


Figure 5.28: Parallel (a) and perpendicular (b) mobility for ionized impurity scattering as a function of temperature for the three different charge densities, once having included three subbands in the dielectric function, once taking only the fundamental subband into account: at higher temperature and for higher charge densities a strong enhancement of the mobility is seen, which is more pronounced in the perpendicular direction.

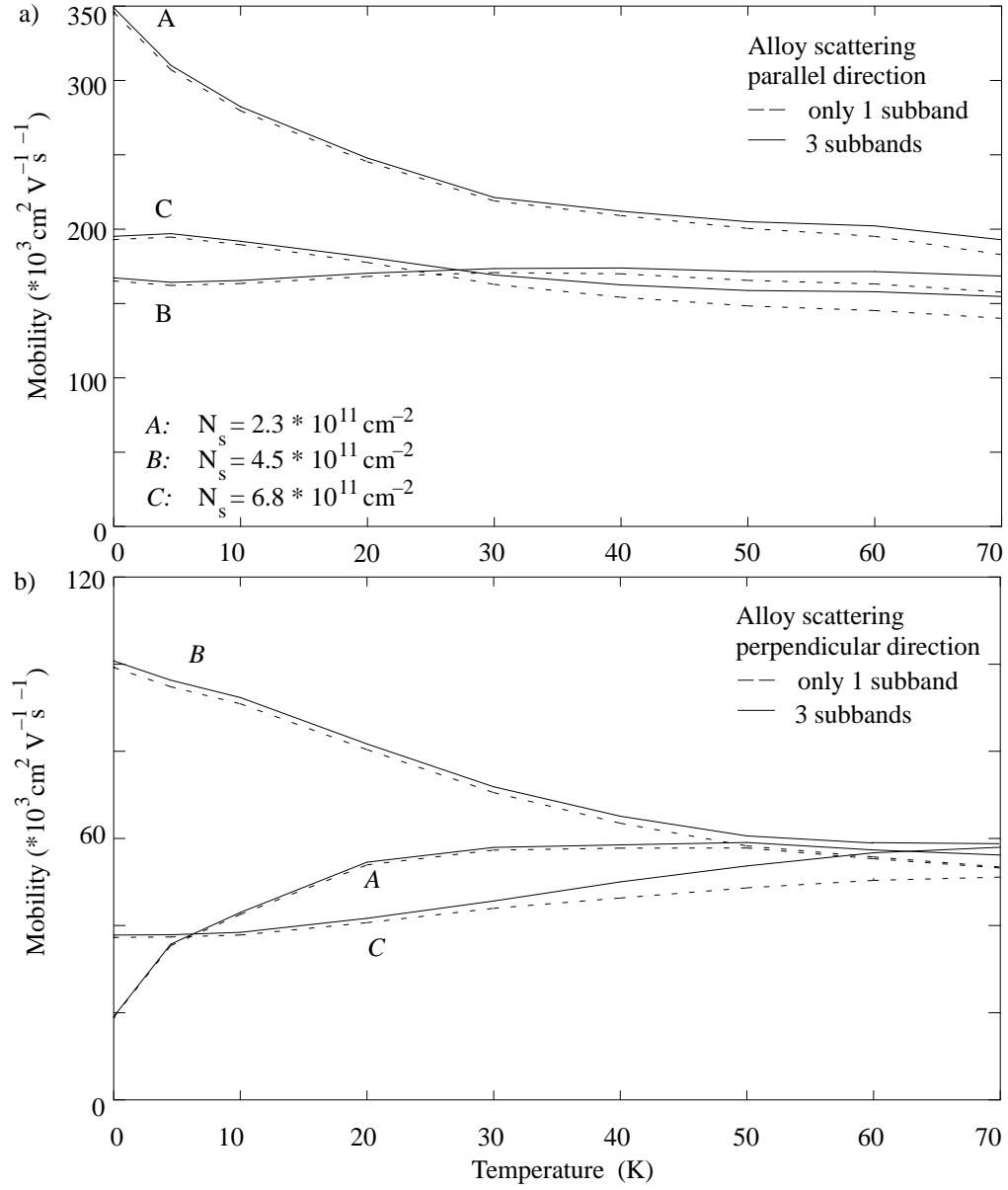


Figure 5.29: *Parallel (a) and perpendicular (b) mobility for alloy scattering as a function of temperature for the three different charge densities, once including three subbands in the dielectric function, once taking only the fundamental subband into account: the effect of the enhancement of the mobility when including three subbands in the calculations is small in comparison to ionized impurity scattering.*

In summary, one finds for different charge densities different temperature dependences of the parallel and perpendicular mobility. This has been explained in terms of the position of the Fermi level with respect to the modulated bandstructure. Such a mobility behavior can be considered as a signature of the existence of minigaps and minibands in the bandstructure.

Chapter 6

Experimental results

In the following the experimental set - up and the acquisition of data shall be described first. Then, the experimental results are presented. They will be analyzed with the help of the numerical results, presented in the previous chapter.

- **Experimental Set - up:** During this thesis, an experiment has been constructed which allows the following experiments:
 - measuring the longitudinal resistance and Hall resistance as function of gate voltage V_g , applied between a top gate and the 2DEG, at a fixed temperature in the range $T = 4.2 - 300\text{K}$.
 - measuring the longitudinal resistance and Hall resistance as a function of temperature.
 - illuminating the sample with a laser of wavelength $\lambda_{Laser} = 628\text{ nm}$.

To be able to do these experiments, a coil is used which provides a magnetic field B up to 0.5 Tesla. A carbon - class resistance is placed just next to the sample to measure accurately the sample's temperature. The temperature could be stabilized within $\pm 0.3\text{K}$.

- **Data acquisition:**

The Hall mobility is given in its general form by

$$\mu_H = \frac{ff}{R_{long.} \cdot N_H \cdot e}, \quad (6.1)$$

where μ_H is the Hall mobility, ff the formfactor of the sample geometry, N_H the Hall charge density, R_{long} the longitudinal resistivity and e the charge of an electron. All experiments are DC measurements. The longitudinal resistance is measured in four point geometry by a current - voltage curve $I(V)$ at zero magnetic field. The current I is typically swept between $-1 \cdot 10^{-6} \text{ A} < I < 1 \cdot 10^6 \text{ A}$.

The Hall charge density is given by

$$N_H = \frac{1}{e B R_H}, \quad (6.2)$$

with the Hall resistance $R_H = V_H/I$.

To obtain R_H as a function of the magnetic field, at 20 different constant low magnetic fields ($B < 0.5 \text{ T}$), current - voltage ($V_H(I)$, $-1 \cdot 10^{-6} \text{ A} < I < 1 \cdot 10^{-6} \text{ A}$) curves are taken. Each $V_H(I)$ curve gives thus the Hall resistance R_H at a given magnetic field. Plotting R_H as a function of the magnetic field B , one obtains from a linear fit the Hall density N_H .

To obtain the real charge density N_s , the Hall charge density has to be multiplied by a correction factor, by the Hall factor r_H [Szmulowics 86]:

$$N_s = N_H * r_H. \quad (6.3)$$

The Hall factor r_H takes the different group velocity distribution of the electrons at finite temperature into account. It is defined as:

$$r_H = \frac{m^*}{e B} \frac{\langle \frac{\tau(E)X(E)}{1+X(E)^2} \rangle}{(\langle \frac{\tau(E)}{1+X(E)^2} \rangle)^2 + (\langle \frac{\tau(E)X(E)}{1+X(E)^2} \rangle)^2} \quad (6.4)$$

with $X(E) = \omega_c \tau(E)$ ($\omega_c = \frac{eB}{m^*}$ is the cyclotron frequency of an electron). It thus depends on the magnetic field, the temperature and the scattering processes, one is considering. In the case of a modulated 2DEG one has to define two Hall factors $r_{H\parallel}$ and $r_{H\perp}$, where $\tau_{\parallel}(E)$ and $\tau_{\perp}(E)$ are integrated over the Fermi surface in the same way it is done in the conductivity and mobility calculations (see section 3.4). The Hall factor was calculated for every measured temperature. The scattering potentials remote ionized impurity scattering, residual impurity scattering, alloy scattering and acoustic phonon scattering are included in all calculations. The difference between N_s and N_H proved to be very small in the case of unmodulated two - dimensional electron systems ($< 2\%$) and becomes only important for modulated two -

dimensional electron systems, when $N_H < 1.6 \cdot 10^{-11} \text{ cm}^{-2}$ (The Hall factor as a function of charge density is shown later in section 6.2 for a modulated 2DEG).

6.1 Unmodulated 2DEG: Effect of Enhanced Screening

In this section the enhancement of the screening, when the second subband of an unmodulated 2DEG is populated is demonstrated in two experiments. The first one consists in deducing the mobility as a function of charge density by measuring the longitudinal and Hall resistivity as a function of gate voltage V_g at $T = 4.2\text{K}$. In the second one, the mobility is investigated as a function of temperature for a given charge density. The sample lay out used for these samples is a standard Hall - bar geometry.

An experiment similar to the first one was done by Mori [Mori 80] on an n - channel inversion layer on the silicon (100) surface. However, they did not compare different screening models. Additionally, they did not convincingly see the onset of the second subband, since they did not reach a high enough charge density. In AlAs/GaAs heterostructure, it was Störmer et al. [Störmer 82], who observed clearly for the first time the onset of the second subband in a mobility - charge density curve. They correctly attributed the decrease of mobility to the intersubband scattering, which takes place as soon as the second subband gets populated, but did not show any calculations. Vinter [Vinter 83] found a qualitative, but not quantitative agreement between the charge - density - voltage dependence of the sample studied in [Störmer 82], but did not discuss the mobility - charge density behavior. Hai et al. [Hai 95] studied the effect of the inclusion of higher subbands in the dielectric function when the second subband gets populated by comparing calculations and transport measurements in peaked δ - doped quantum wells.

An additional motivation to study the effect of enhanced screening as a function of temperature arises from the fact, that one expects the impact of including higher subbands in the dielectric function to be even stronger at higher temperature in modulated two - dimensional electron gas.

To investigate the screening effects experimentally, a standard AlAs/GaAs heterostructure (Q632) $\text{Al}_{0.33}\text{Ga}_{0.67}\text{As}$ with one δ - doping plane has been grown. The spacer thickness $r_{zsp.}$ is 2.5 nm. The spacer thickness is chosen to be sufficiently small to provide a high charge transfer into the

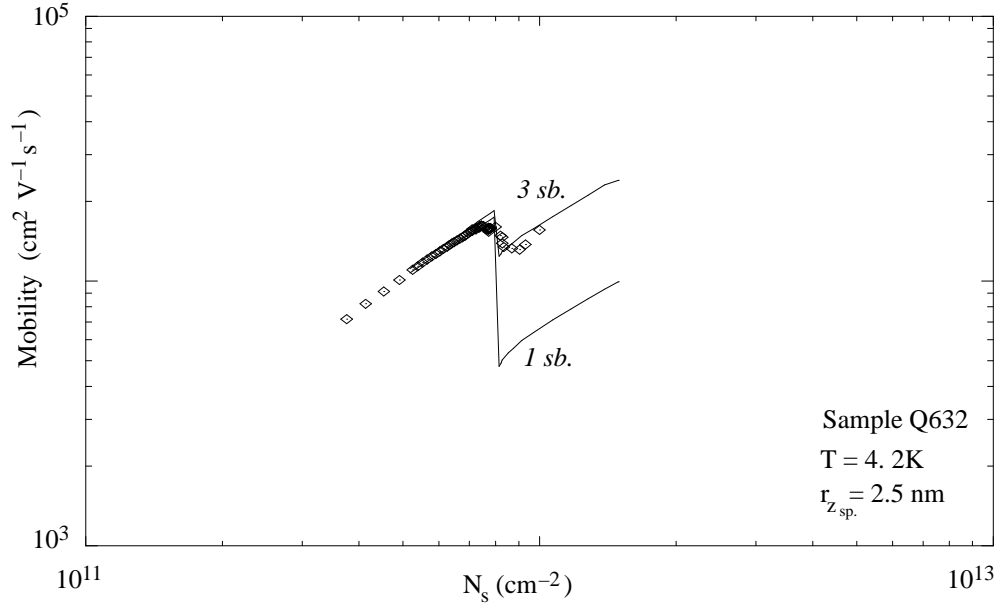


Figure 6.1: *Mobility as a function of charge density at $T = 4.2\text{K}$ (points) for sample Q632 with two fits, once having included three subbands in the dielectric function and once having taken only one subband into account. The agreement between the experimental data and the "three subbands" model is excellent.*

channel of the heterostructure. Thus, even at low temperature, the second subband is populated. Due to the small spacer the remote ionized impurity scattering is far dominant (99 %) with respect to all other scattering processes at low temperature.

In Fig. 6.1 the mobility as a function of charge density, measured at $T = 4.2\text{ K}$ is shown for sample Q632 ($r_{z.sp.} = 2.5\text{ nm}$). Equally shown are the corresponding calculations, having taken three (or one, respectively) subbands in the dielectric function calculations into account (The calculations are explained in detail in section 3.6). The number of ionized impurities is assumed to be $N_D^+ = 1.75 \cdot 10^{12}\text{ cm}^{-2}$. This value has been chosen to obtain good agreement between the calculated and measured mobility, when only the first subband is populated. It is also in good agreement with nominal doping of $N_D = 2.5 \cdot 10^{12}\text{ cm}^{-2}$. The calculations are executed at $T = 0\text{ K}$. The fit, corresponding to the inclusion of three subbands is in excellent agreement with the experimental data. Contrarily, taking only one subband in the dielectric function into account, the mobility drops far below the experimental

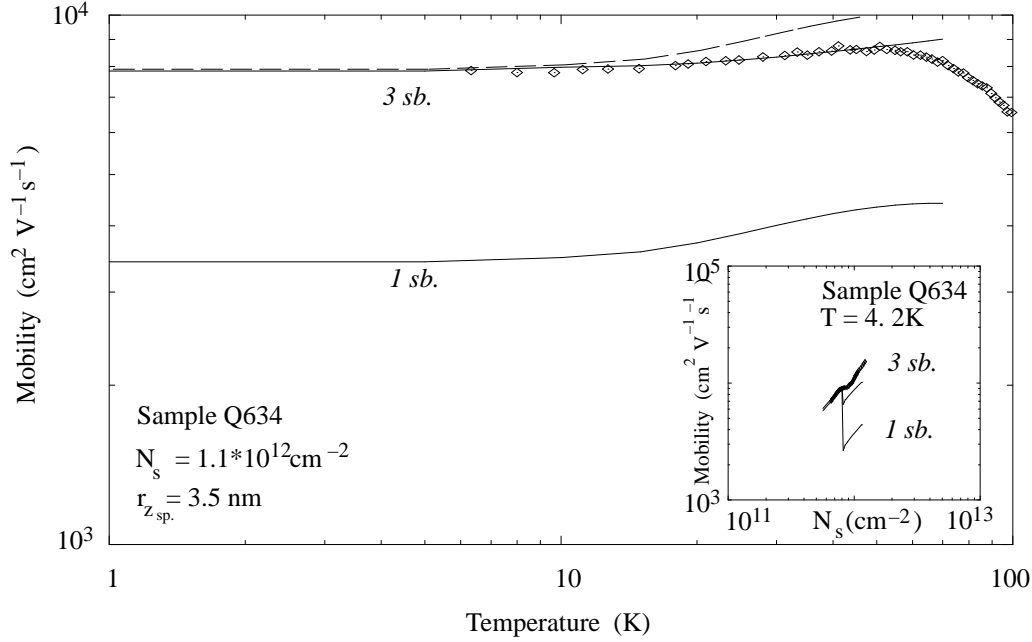


Figure 6.2: *Mobility as a function of temperature for sample Q634 with two fits (solid lines), once including three subbands in the dielectric function and once taking only one subband into account. In dashed line, a one subband calculation with an artificial low number of ionized donors to assure agreement between experiment and fit at low temperature is shown. However, the discrepancy at higher temperature shows that a "one subband" fit is less appropriate. In the inset the mobility of sample Q634 is shown as a function of charge density at $T = 4.2 \text{ K}$. The number of ionized donors is kept constant for both the charge density and temperature dependent mobility calculations.*

values, when the second subband gets populated. This experiment together with the numerical fits demonstrate clearly that a "one - subband" model of the dielectric function does not calculate correctly the mobility of an unmodulated 2DEG as soon as the second subband is populated. If the second subband is populated, higher subbands have to be included in the dielectric function. As explained in 5.2, the number of subbands which have to be taken into account is hereby determined to be $n+1$, where n is the number of occupied subbands.

To evaluate the difference in the temperature dependence of the screening models the mobility of sample Q634 ($z_{\text{spac.}} = 3.5 \text{ nm}$, $N_s(T = 4.2 \text{ K}) =$

$1.1 \cdot 10^{12} \text{ cm}^{-2}$) is investigated as a function of temperature. The results are shown in Fig. 6.2. In the inset the mobility as a function of charge density is shown. Although the spacer is greater with respect to Q632, a lower mobility is obtained. This demonstrates that the growth conditions were worse than the one for sample Q632. To calculate the mobility as a function of charge density, and to find good agreement between the calculated and measured mobility, when only one subband is populated, one has to assume $N_D^+ = 5.0 \cdot 10^{12} \text{ cm}^{-2}$.

Calculating the mobility as a function of temperature, the same value N_D^+ is taken. The mobility increases slowly and decreases from $T = 65\text{K}$ due to optical phonon scattering. A pronounced difference between the theoretical curves, once including three subbands and once having taken only one subband into account, is visible. Even, if one assumed an (artificial) low number of ionized impurities $N_D^+ = 3.0 \cdot 10^{11} \text{ cm}^{-2}$ to find agreement between the experimental data and the calculations at low temperature, one would not find good agreement at higher temperature (see Fig. 6.2, dashed line).

In summary, the good agreement between experiments and calculations demonstrate the importance of including higher subbands in the dielectric function at higher charge density and / or higher temperature. The number of subbands which have to be included is hereby determined to be $n+1$, where n is the number of occupied subbands.

6.2 Modulated 2DEG: Evidence of Minigaps

Having all the theoretical results discussed in chapter 5.3 in mind, the question arises which kind of effects can be experimentally demonstrated. The first trial to observe minigaps was done in two dimensional electron inversion layers on (119)Si [Cole 77]. They detected a for the existence of a minigap characteristic "w" - structure (see section 5.2) in the dc conductivity as a function of charge density. T. Evelbauer et al. [Evelbauer 86] observed a similar "w" - structure in metal - oxide - semiconductor structures prepared on high index surfaces of p-InSb. However, it was shown that these minigaps do not originate from a lateral superlattice effect [Sham 78].

In transport measurements, Sakaki et al. [Motohisa 89] were the first who measured an anisotropy of the mobilities in the parallel and perpendicular direction of a lateral structure grown on GaAs vicinal surfaces. The lateral structure was produced by the insertion of half an Aluminum monolayer in the channel region of a heterojunction grown on a vicinal surface. A plausible

approach of interpretation was that the anisotropy is a sign of nonparabolicity in the miniband structure of a periodic lateral potential. However, a single anisotropy in the mobilities does not demonstrate the existence of a lateral organization, e.g. the formation of a periodic modulation. The anisotropy of the mobility can equally arise from the formation of anisotropic islands. For instance, J. Bloch demonstrated that the anisotropy in optical properties of lateral structures due to the fractional deposition of one monolayer is not due to the lateral periodic organization along the steps but to the formation of anisotropic islands [Bloch 94]. The optical properties were independent of the lateral period given by the terrace length of the vicinal surfaces. In contrast, in lateral super - lattices, which consist of at least 10 monolayers, the optical properties depend strongly on the terrace length, indicating the influence of the lateral potential modulation [Bloch 94].

Recently, for the first time, clear evidence of the minigap induced by a superlattice has been shown by magnetoresistance measurements [Albrecht 99]. The periodic modulation of the 2DEG is obtained by means of patterned top gates. The miniband structure is manifested by modified Shubnikov-de Haas oscillations with higher periodicity.

However, the direct observation of the minigaps by measuring the mobility as a function of charge density at low temperature or the (indirect) observation by measuring the mobility as a function of temperature has so far been illusive in modulated two - dimensional electron systems. In this section, the evidence of minigaps in temperature dependent and charge density dependent measurements is given.

Two different kind of experiments are discussed:

- Temperature dependent measurements at a certain charge density. The charge density is changed by illuminating the sample with a laser wavelength of 628 nm at low temperature ($T = 4.2\text{K}$).
- Density dependent measurements at low temperature ($T = 4.2\text{K}$). The charge density is changed by the application of a bias voltage between a front gate and the modulated 2DEG.

In order to understand the experimental results, they are then compared to the previously obtained theoretical results.

The studied samples are all AlAs/GaAs lateral superlattices. The specific characteristics are listed in Table 6.1. It shall be reminded that in the case of a modulated electron gas, longitudinal and Hall resistance are measured in four point geometry for the parallel and perpendicular direction with respect to the lateral superlattice (see Fig. 6.3, sketched for a configuration,

Sample	L206.1	L206.2	K508
x_{Al}^{LSL} :	5 %	5 %	5 %
$x_{Al}^{Barr.}$:	33%	33%	33%
spacer:	9 nm	9 nm	9 nm
width of LSL:	20.4 nm	20.4 nm	12.4 nm
lat. pot. mod.:	max.	tilted	max.
$n_s(T = 4.5K)$:	$5.1 * 10^{11} \text{cm}^{-2}$	$5.1 * 10^{11} \text{cm}^{-2}$	$4.2 * 10^{11} \text{cm}^{-2}$

Table 6.1: *Parameters of the samples studied in this work. The difference between sample L206.1 and L206.2 is the strength of the lateral potential modulation, e.g. L206.2 is tilted.*

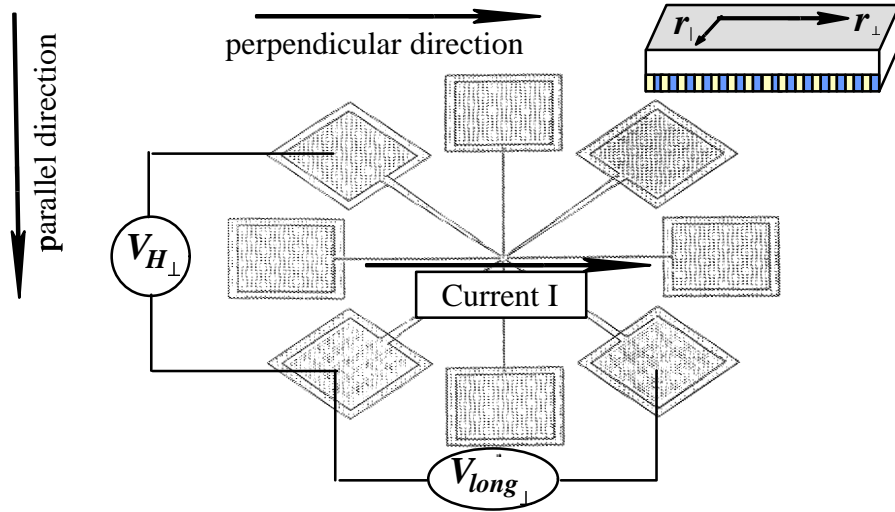


Figure 6.3: *Measurement configuration, when measuring the perpendicular direction: with one multimeter the longitudinal voltage $V_{long_{\perp}}$ is measured, with the other one the Hall voltage $V_{H_{\perp}}$*

when measuring the longitudinal and Hall resistance of the perpendicular direction). All presented experimental results are measured in four - point geometry with this sample lay-out. Equally, the data acquisition procedure is the same for all measurements, described below. Due to the sample layout, the parallel and perpendicular resistance cannot be measured at the same time. Thus, for a given charge density and for a given temperature, first the parallel direction is measured, then the perpendicular one. Accordingly, one

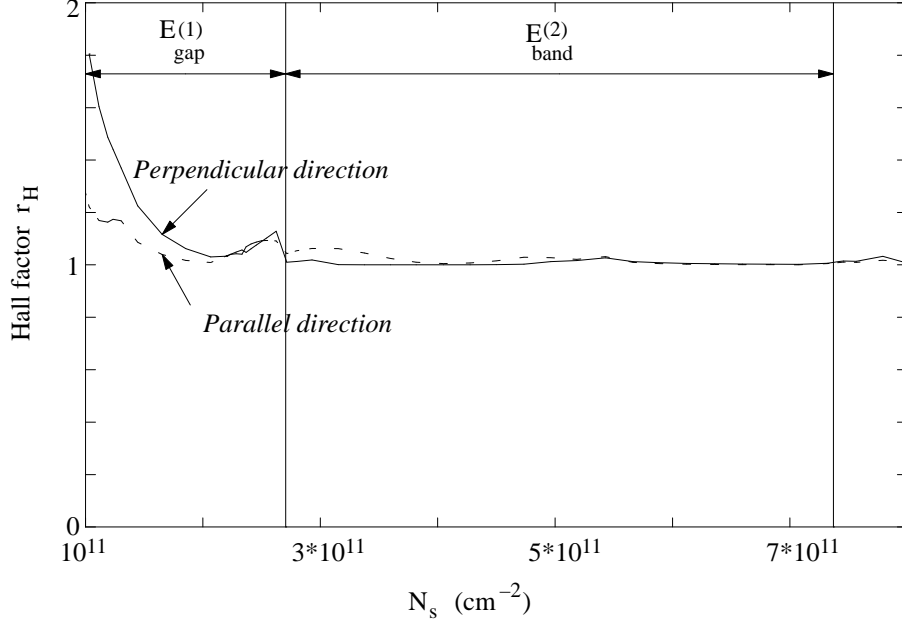


Figure 6.4: Hall factor r_H as a function of charge density N_s . r_H differs only significantly from one, when the Fermi level is in the first minigap.

now defines a "parallel" and "perpendicular" Hall mobility:

$$\mu_{H\parallel} = \frac{ff}{R_{long.\parallel} e N_{H\parallel}}, \quad (6.5)$$

$$\mu_{H\perp} = \frac{ff}{R_{long.\perp} e N_{H\perp}}. \quad (6.6)$$

The mobilities μ_{\parallel} and μ_{\perp} are determined in the same manner as in the case of an unmodulated two - dimensional electron gas (via the Hall factor $r_{H\parallel}$ and $r_{H\perp}$). In Fig. 6.4 the Hall factor, calculated for the parallel ($r_{H\parallel}$) and perpendicular ($r_{H\perp}$) direction of a modulated electron gas is shown as a function of charge density N_s . In the here considered charge density range, which is the one, which were experimentally accessible, r_H differs from one, when the Fermi level is in the first minigap. The Hall factor, calculated for the perpendicular direction is greater than for the parallel direction, reflecting that the spread in the velocity distribution is greater in the perpendicular than in the parallel direction.

6.2.1 Parallel and Perpendicular Mobility as a Function of Temperature

The experimentally determined parallel and perpendicular mobilities of a modulated 2DEG as a function of temperature for different charge densities are discussed. The mobilities are deduced from the experimentally measured longitudinal and Hall resistances, as described above. These mobilities are then compared to numerical calculations. The agreement between the experimental results and fits allows to determine the amplitude of the lateral potential modulation. Once the amplitude of the lateral potential modulation is known, one can position the Fermi levels corresponding to the experimentally determined charge densities on the (calculated) mobility - Fermi energy curve. This allows to understand the physical reasons for the experimentally observed different temperature dependent behaviors of the mobilities.

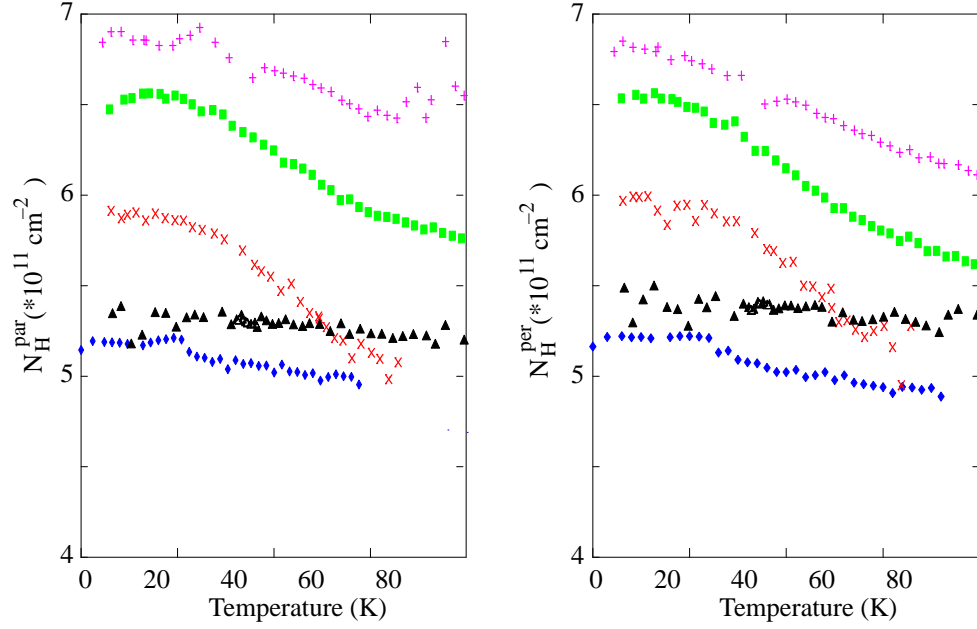


Figure 6.5: *Parallel (left) and perpendicular (right) Hall charge density as a function of temperature: the measured difference in the Hall voltage, leading to a difference value in the Hall charge density, between the two directions is smaller than 4 %.*

In Fig. 6.5 the Hall density $N_{H\parallel}$ and $N_{H\perp}$, obtained by measuring the

parallel and perpendicular Hall resistance is shown. As expected, the difference between the parallel and perpendicular Hall density is very small ($< 4\%$), reflecting the homogeneity of the sample and a well defined geometry of the sample layout. The curve corresponding to the lowest charge density is obtained by a different temperature cycle, without having illuminated the sample. The other charge densities have been obtained by illuminating the sample at low temperature until the desired charge density is obtained. The temperature dependent measurements were then started 30 min. later.

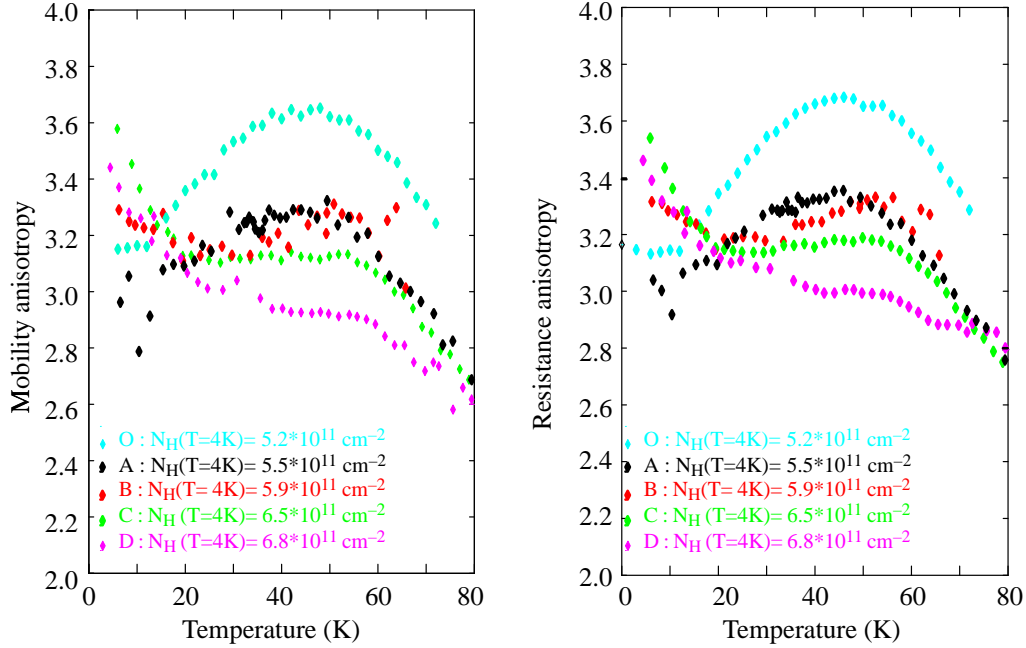


Figure 6.6: *Mobility (left) and resistance (right) anisotropy as a function of temperature: The parallel mobility is up to about a factor four stronger than the perpendicular one, resulting in a strong anisotropy.*

The difference of the parallel and perpendicular mobility, e.g. the anisotropy of the mobility $r_{mob}(T) = \mu_{||}(T)/\mu_{\perp}(T)$ is shown in Fig. 6.6 (left) for sample L206.1: At low temperature, $r_{mob}(T)$ assumes a value between 2.8 and 3.6, depending on the charge density. Additionally, for some charge densities an anisotropy maximum is seen at higher charge density. In order to understand the origin of the anisotropy, which is equally reflected in the resistance anisotropy (Fig. 6.6, right), one is led to look on the parallel and perpendicular mobility separately (Fig. 6.7). Different interesting features

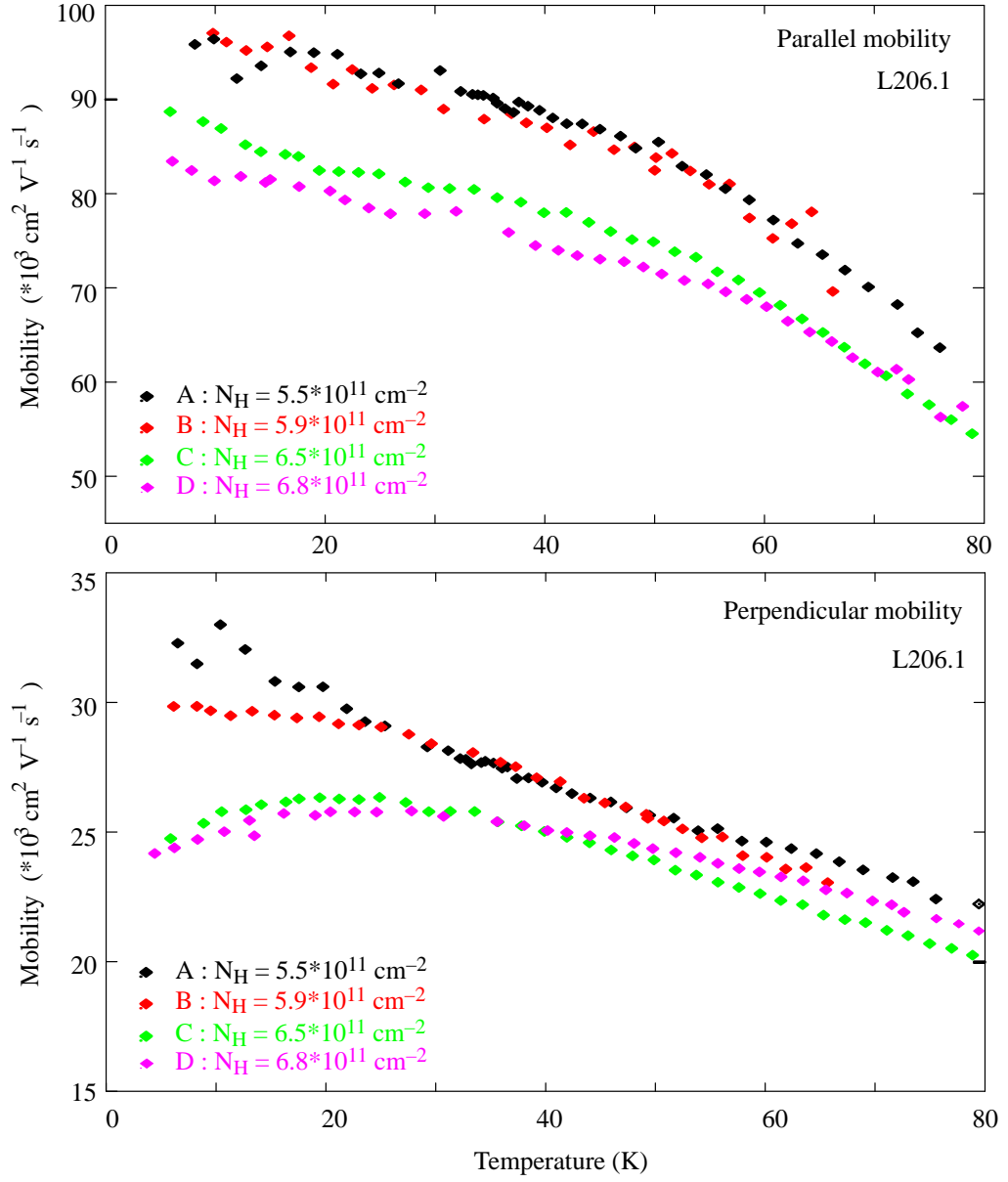


Figure 6.7: Parallel (upper figure) and perpendicular (lower figure) mobility as a function of temperature: the parallel mobility depicts a behavior, which is similar to the one, one would obtain, when calculating the temperature dependent mobility for an unmodulated two - dimensional electron gas with the same structure parameters. In contrast, the perpendicular mobility shows different temperature behaviors, depending on the charge density.

are observed:

- At low temperature the parallel and perpendicular mobilities increase basically with decreasing charge density. As one increases the temperature, the parallel mobility decreases, regardless of the considered charge density.

Remarkably, all parallel mobilities show the same temperature dependence at higher temperature.

- Considering the perpendicular direction, different temperature dependent behaviors are seen: depending on the charge density, the mobility either decreases (A), remains constant (B) or increases (C,D). This different temperature behavior even leads to the crossing of different mobility curves.

In order to understand the temperature dependence of the parallel and perpendicular mobility, numerical calculations are performed. This allows in particular to determine the position of the Fermi level with respect to the band structure, i.e. with respect to the minibands and minigaps.

The charge density is assumed the one which is experimentally determined within 5 %. The incertitude of 5% allows to change slightly the Fermi energy with respect to the lateral potential modulation in order to obtain better agreement between experimental results and fits. The fitting procedure is an iterative process including two steps:

- The 2D bandstructure is calculated for a given temperature. Hereby the amplitude of the lateral potential (e.g. the first and second Fourier coefficient) is adjusted (e.g. taken as fit parameters) within limits, given by optical measurements ([Mélin 98], for the first Fourier coefficient) and AFM - measurements ([Laruelle 99], for the coefficient $V_{sd}^{(2)}$).
- The from these band structure calculation obtained wavefunctions are then injected in the linearized Boltzmann transport equation. Remote ionized impurity scattering, residual impurity scattering, alloy scattering and acoustic phonon scattering are taken into account.

The number of ionized impurities is assumed to be equal to the charge density, e.g. $N_D^+ = N_s$. This assumption is justified because a) one has a second δ - doping plan which saturates the surface states and b) the charge density is changed by illumination. The exact ratio between the different scattering contributions, e.g. between remote ionized impurity scattering and alloy scattering, depends on the charge density: at

higher charge density the remote ionized impurity scattering becomes even more dominant, since $N_D^+ = N_s$, although μ_{alloy} diminishes with higher N_s and $\mu_{\text{imp.}}$ increases with higher N_s . For example at $T = 0\text{K}$, one finds an alloy scattering contribution to the total resistance of about 30% and a remote ionized scattering contribution of 70% for $N_s = 5.3 \cdot 10^{11} \text{ cm}^{-2}$. Considering a charge density of $N_s = 6.9 \cdot 10^{11} \text{ cm}^{-2}$, the contributions are given by 22 % (alloy scattering) and 78 % (remote ionized impurity scattering) at $T = 0\text{K}$. At $T = 70\text{K}$ the contribution of acoustic phonon scattering to the total resistivity is about 10 %. The screening is taken into account by the dielectric function, including the three lowest subbands in the calculation. The scattering angle is taken as the angle between the states $\vec{v}_{\vec{k}}$ and $\vec{v}'_{\vec{k}}$.

To obtain good agreement between the experimental curves and the numerical calculations, the lateral potential modulation is taken as $V_{pp} = 11 \text{ meV}$ (and $V_{sd}^{(2)}$ (see section 2.2.2) was found to be 0.15). This corresponds to a first minigap of approximately $E_{\text{gap}}^{(1)} = 4 \text{ meV}$ and a second one of $E_{\text{gap}}^{(2)} = 2 \text{ meV}$. (These values are deduced from a band structure calculation for a charge density of $N_s = 5.3 \cdot 10^{11} \text{ cm}^{-2}$. The gap size are slightly different for other charge densities due to screening effects, which depend on the charge density.) Accordingly, the lateral potential modulation is less pronounced than the one ($V_{pp} = 23 \text{ meV}$) considered for the calculations discussed in chapter 5.3. As a consequence, the transport features due to the lateral potential modulation are less accentuated. However, they still manifest themselves by the different temperature dependence of the parallel and perpendicular mobility. In Fig. 6.8. the experimental measurements (left) and corresponding numerical calculations (right) are juxtaposed. It shall be emphasized that all curves in Fig. 6.8 are calculated with the same set of parameters (e.g. amplitude of lateral potential modulation, structure parameters, etc.) It is only the charge density, which is changed between the different curves and which is given by the experimental data (see explanation above). This is in that aspect important that thus (experimentally and numerically) the ratio between remote ionized impurity scattering and alloy scattering changes: the at higher charge density remote ionized impurity scattering becomes more important ($N_D^+ = N_s$).

One numerically finds

- at low temperature
 - for the parallel and perpendicular mobilities the same charge den-

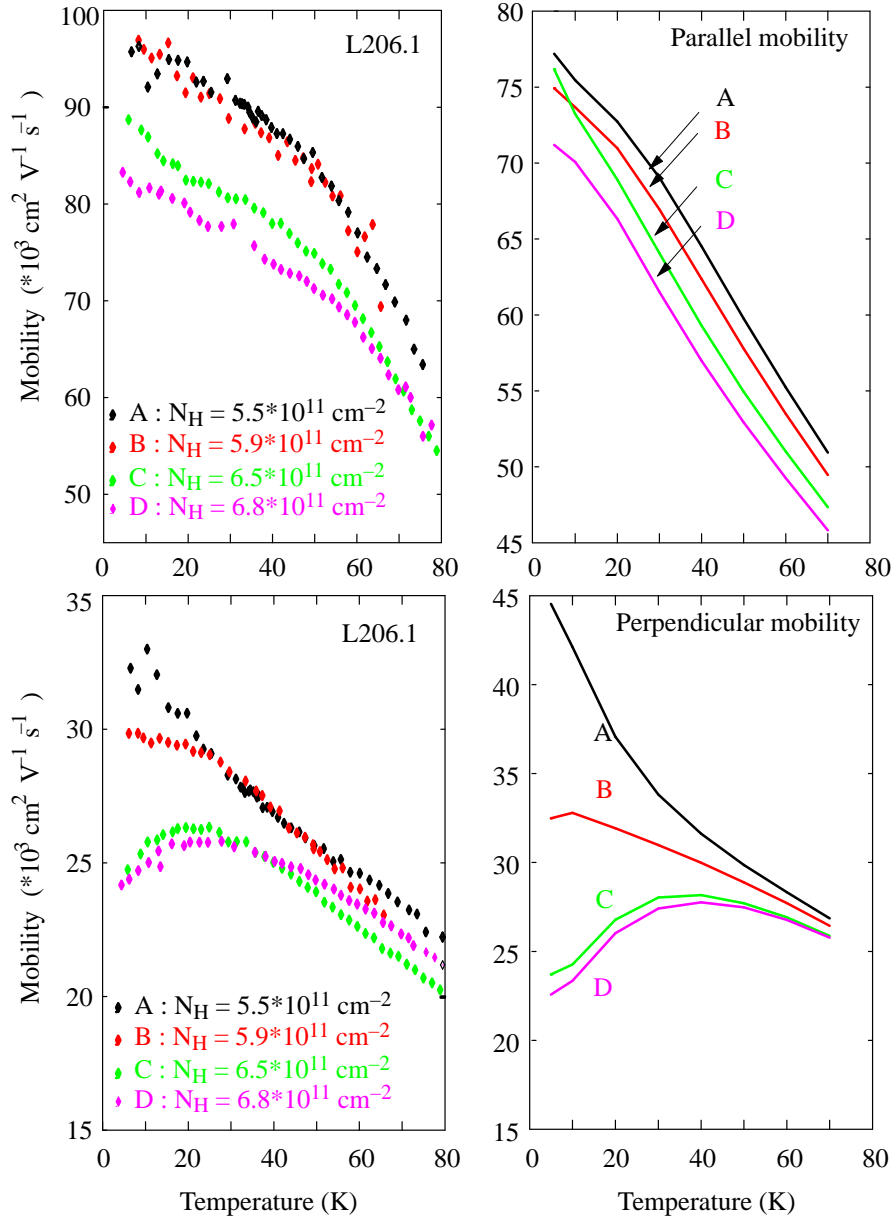


Figure 6.8: Experimentally (left) and calculated (right) parallel (upper graph) and perpendicular (lower graph) mobility as a function of temperature for different charge densities. The experimentally observed typical temperature behavior of the parallel and perpendicular mobility is refound in the numerical calculations.

sity dependency as experimentally: The mobilities basically decrease as a function of increasing charge density.

- as one increases the temperature
 - the decrease of the parallel mobilities, e.g. the first rather gentle decrease of the mobilities and from a certain temperature on the faster decrease as a function of temperature.
 - the anomalies of the perpendicular mobilities, e.g. the mobilities decrease as a function of temperature at lower charge density and the mobilities increase at higher charge density in the temperature range $T=4-25\text{K}$.

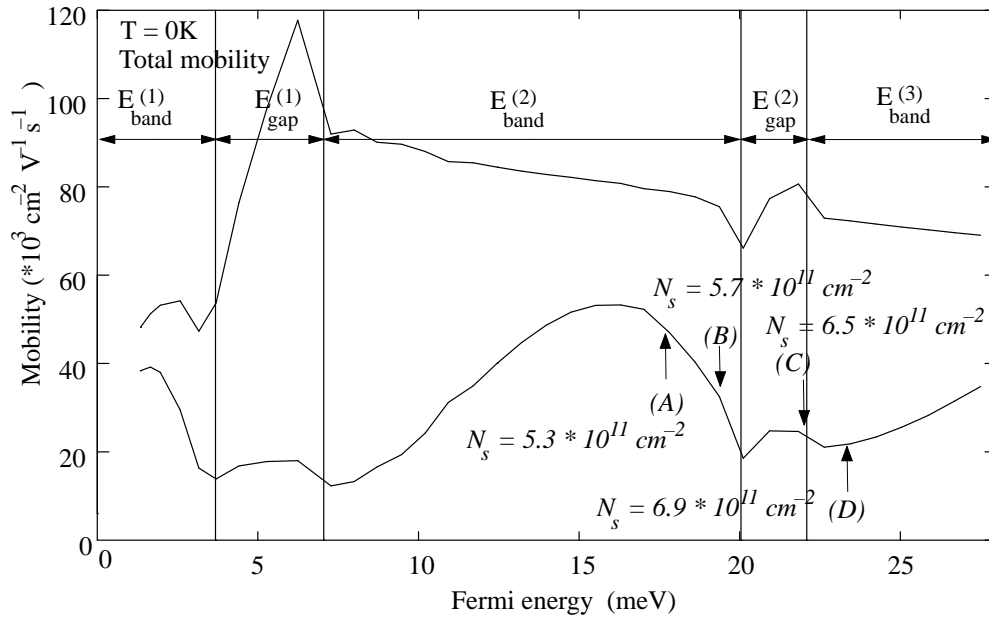


Figure 6.9: *Parallel and perpendicular mobility as a function of Fermi energy. The positions of the Fermi energy, which correspond to the in the calculations considered charge densities, are indicated by arrows: whereas one expects a mobility decrease for A and B as a function of temperature, $\mu(C)$ will remain constant in the beginning of increasing temperature and $\mu(D)$ will increase.*

One thus finds good qualitative agreement, demonstrating the existence of minigaps in the electronic bandstructure of the modulated 2DEG. Only by assuming the existence of the first and second minigap in the bandstructure,

one is able to fit the different behavior of the parallel and especially perpendicular mobility as a function of temperature. It is assumed that one could even find better quantitative agreement between experimental data and calculations by changing either slightly the amplitude of the lateral potential modulation or the ratio between the contributions of the different scattering processes. This has not been done, because the calculations are very time consuming.

To understand the physical reasons of these different temperature effects, one is once again led to regard the position of the Fermi level on the mobility - Fermi energy curve (Fig. 6.9). The charge densities for which the mobilities as a function of temperature have been calculated (Fig. 6.8, right) are indicated by arrows. As discussed in detail in Chapter 5.5, one expects the following temperature dependent mobility behavior for the different charge densities:

- Curve A
The position of the corresponding Fermi energy is close to a maximum. Hence, as one increases the temperature, the mobility decreases. This is experimentally observed.
- Curve B
The position of the corresponding Fermi level is close to an inflection point: In the beginning of temperature increase, the mobility varies little. This is experimentally observed.
- Curve C and D
The Fermi positions are close to a minimum in the mobilities curve. Hence, the mobilities increase, as one increases the temperature. This is experimentally observed.

In conclusion, the interplay of experiments and calculations have allowed to demonstrate the existence of minigaps. Only by the assumption of a lateral potential modulation, the different mobility - temperature curves for different charge densities have been explained.

6.2.2 Impact of the Second Fourier Coefficient

In Fig. 6.10 the experimentally measured parallel and perpendicular resistance as a function of temperature is shown for a modulated 2DEG, for sample K508. These measurements together with numerical calculations, equally shown in Fig. 6.10, allow to study the impact of the second Fourier

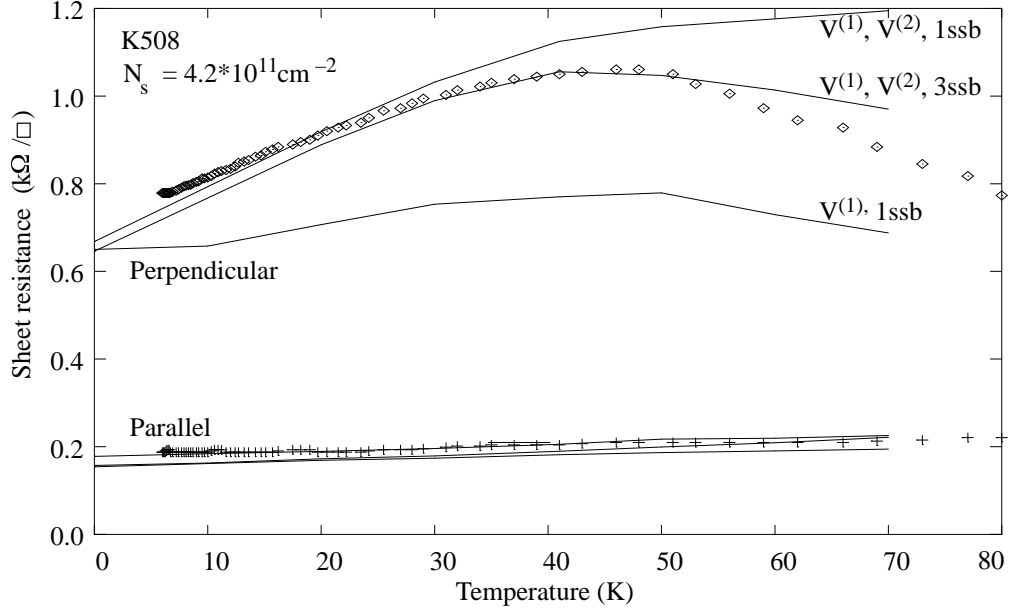


Figure 6.10: *Resistance as a function of temperature with different numerical fits: The experimental data are best reproduced when taking into account the second Fourier coefficient in the lateral bandstructure calculations as well as including three subbands in the dielectric constant.*

coefficient of the lateral potential modulation and the effect of the inclusion of higher subbands in the dielectric function. Experimentally, one observes at $T = 4.2\text{K}$ a ratio of a factor 3.4 between the perpendicular and parallel resistance. As one increases the temperature, the perpendicular resistance first raises strongly, saturates at about $T = 50\text{K}$ and then even decreases. The parallel resistance does not exhibit any spectacular effect: it increases slightly with increasing temperature.

If one tries to fit these experimental data, one obtains the following results: Taking only one Fourier coefficient ($V_{pp} = 18\text{ meV}$) into account, one reproduces well the measured resistance at low temperature. However, as one increases the temperature, the fit does no longer agree with the experimental data: the experimentally observed strong increase is not reproduced. To be able to reproduce the experimentally observed increase, the second Fourier coefficient of the lateral potential modulation has to be taken into account. The amplitude of the lateral potential modulation was hereby found to be $V_{pp} = 16\text{ meV}$, $V_{sd}^{(2)} = 0.32$, corresponding to a first minigap of size $E_{gap}^{(1)} =$

5 meV and a second minigap of size $E_{gap}^{(2)} = 3$ meV. This can be interpreted as the signature of enhanced ionized impurity scattering introduced by the second Fourier coefficient: As it was demonstrated in chapter 5.4.4, the main impact of the second Fourier coefficient is the increase of the perpendicular resistance as the Fermi energy approaches the second miniband, e.g. if one takes in the mobility calculations states into account, which are in the vicinity of the second minigap. Since at $T = 4.2\text{K}$, the Fermi level corresponding to the measured charged density ($N_s = 4.2 \cdot 10^{11} \text{ cm}^{-2}$) is in the middle of the second miniband, increasing the temperature has the consequence that one integrates the more and more over states being in the vicinity of the second minigap. Moreover, it is interesting to remark that even at low temperature the total resistance depends also on the second Fourier coefficient. This is the reason why the amplitude of the lateral potential modulation has to be differently chosen ($V_{pp} = 16$ meV, when taking a second Fourier coefficient into account, whereas $V_{pp} = 18$ meV, when considering a sinusoidal lateral potential modulation).

Up to now only the lower temperature anomaly (e.g. the strong raise of the perpendicular resistance as a function of temperature) has been discussed. Nothing has been said about the experimentally observed decrease of the resistance when one increases further the temperature.

Higher temperature implies the population of higher subbands. One thus has to take higher subbands in the dielectric function into account. This has been already demonstrate for the case of an unmodulated 2DEG.

In Fig. 6.10 the numerical calculations, taking one subband in the dielectric function into account are shown in comparison with calculations, including three subbands in the dielectric function. Both curves fit rather well the experimentally observed increase of the perpendicular resistance. However, the measured decrease of the perpendicular resistance with increasing temperature can only be reproduced, by the inclusion of higher subbands (here three) in the dielectric constant. This demonstrates again the importance of the inclusion of higher subbands in the dielectric constant at higher temperature.

6.2.3 Effect of the Tilt of the Lateral Potential Modulation

Further support for the importance of taking the second Fourier coefficient of the lateral potential modulation into account is given by regarding the effect of the tilt (see also section 2.2.2) of the lateral potential modulation

on the resistance anisotropy $r_{res} = R_{long.\perp} / R_{long.\parallel}$. For this purpose, the resistance as a function of temperature is measured for sample L206.1 and L206.2 (without the application of a bias voltage), e.g. for two samples, differing in their lateral potential modulation amplitude. (L206.1 has maximal lateral modulation amplitude, whereas L206.2 is taken from a tilted region, e.g. where the lateral potential modulation is weakened.) The resistance anisotropy r_{res} is shown as a function of the inverse of temperature in Fig. 6.11. L206.1 exhibits an anisotropy of about 2.8 at lower temperature and

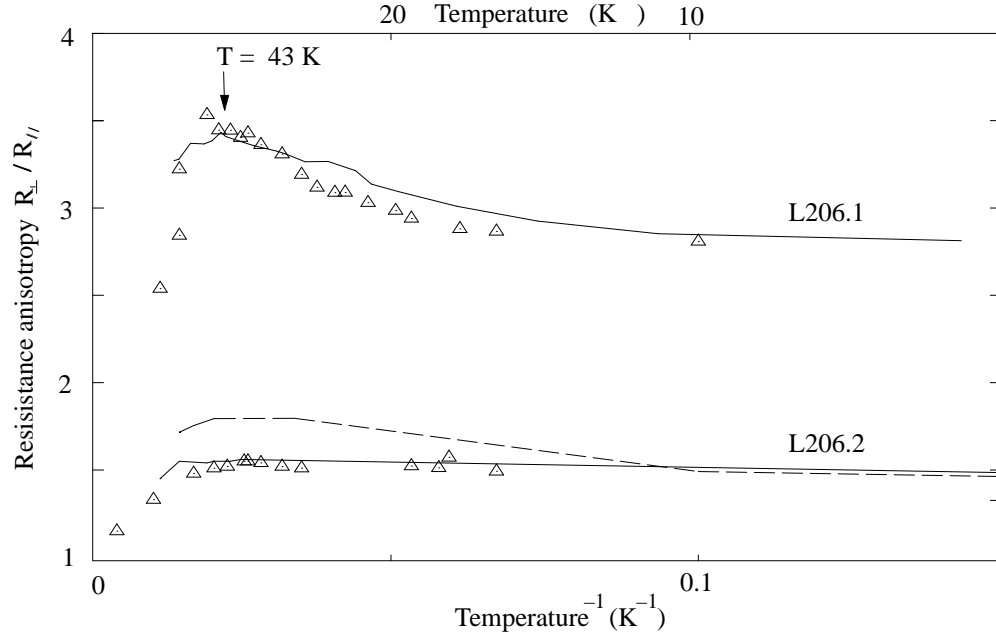


Figure 6.11: *Resistance anisotropy as a function of the inverse of temperature for an untilted sample (L206.1) and a tilted sample (L206.2). The corresponding fits are explained in the text.*

a pronounced maximum at finite temperature. As it is now understood, the anomaly arises from an anomaly in the perpendicular direction. Oppositely, L206.2 has only a small anisotropy at low temperature and does not show any anomaly as a function of temperature.

The interest of this measurement is revealed by the corresponding numerical calculations: The solid lines, fitting L206.1 and L206.2, corresponds to the calculations, where the **same** lateral potential modulation ($V_{pp} = 11$ meV) has been assumed and the tilt parameter ϵ (see chapter 2.2.2, here found to be 1.3) has been taken as fit parameter for sample L206.2. The ex-

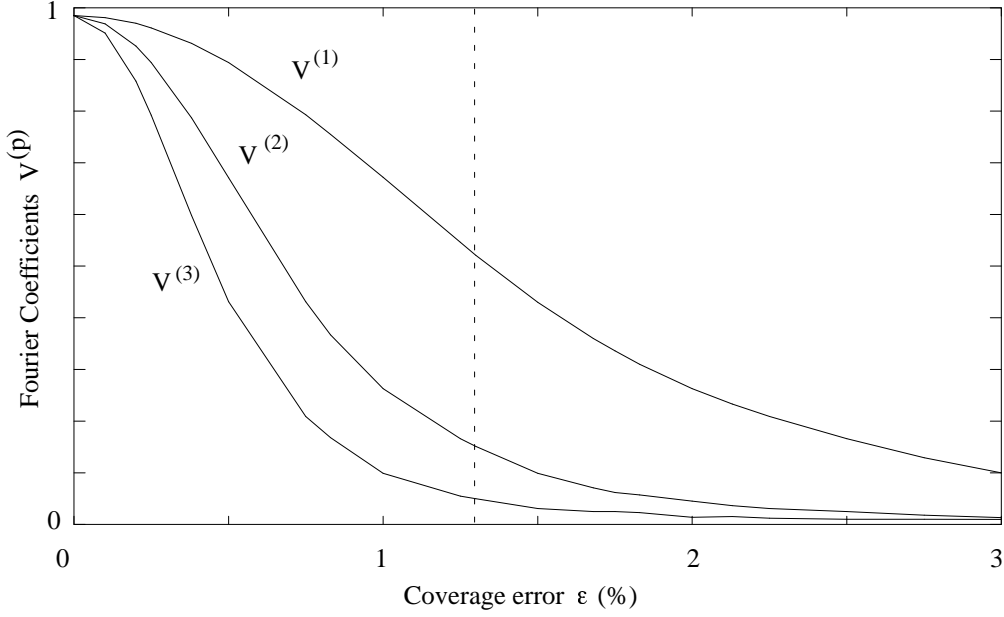


Figure 6.12: *Relative variation $V^{(p)}(\epsilon)$ as a function of the coverage error ϵ in tilted lateral superlattices: Each Fourier coefficient diminishes as a special function of ϵ . Dashed line: Indication of the tilt value, used to fit L206.2.*

perimental data are fairly well reproduced. In contrast, if one tries to fit the experimental data of L206.2 by assuming a weakening of the lateral potential modulation (e.g. each Fourier coefficient is divided by the same factor), one does not find good agreement with the experiment (fit in dashed line) for L206.2.

The explanation is found by regarding Fig. 6.12, where the first three Fourier coefficients, being averaged by the fundamental subband $V^{(p)}(r_{\perp}, \epsilon) = \langle V^{(p)}(r_{\perp} + \frac{\epsilon r_z}{a}) \rangle_{\xi_0(r_z)}$ [Etienne 96.1] are shown as a function of the coverage error ϵ . Higher Fourier coefficients decrease faster as a function of the tilt than the first one. This is well taken into account by using the tilt parameter as fit parameter. In contrast, assuming a weakening of the lateral potential modulation, results in an overestimation of the second Fourier coefficient, resulting in a resistance anisotropy for L206.2, not observed experimentally.

In summary, this experiment gives further support to the importance of taking the second Fourier coefficient of the lateral potential modulation into account. Or, otherwise said, this result implies that assuming only a sinusoidal lateral potential is not justified.

6.2.4 Which Scattering Angle: $\theta_{\vec{v}_k}$ against $\theta_{\vec{k}}$?

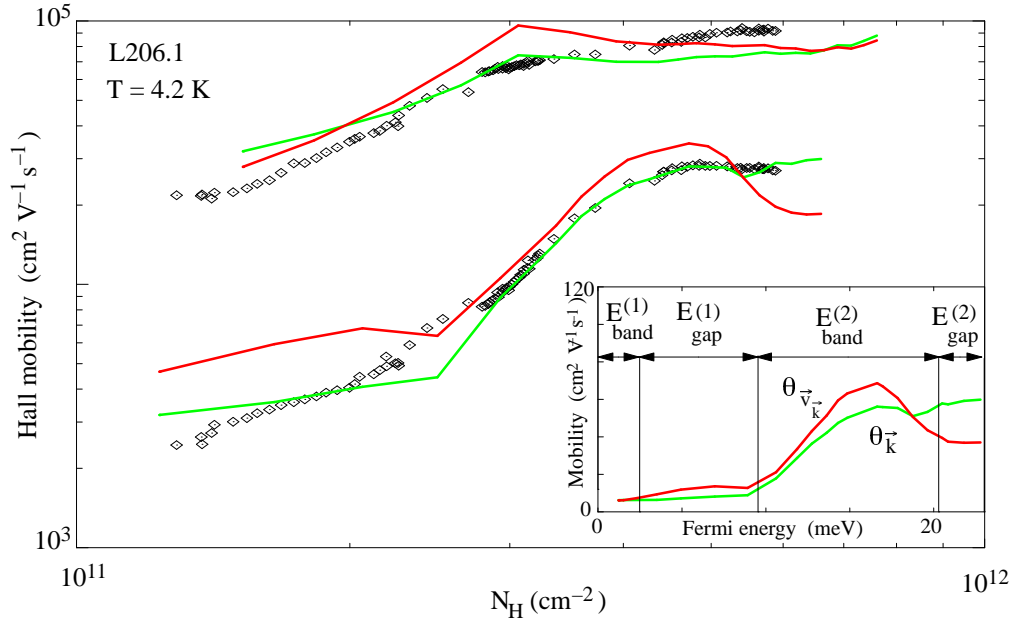


Figure 6.13: *Parallel and perpendicular Hall mobility obtained from experimental data as a function of Hall charge density at $T = 4.2$ K (points) with the corresponding calculations, once having taken the angle $\theta_{\vec{k}}$ (green line) and once the angle $\theta_{\vec{v}_k}$ (red line). Better agreement for the perpendicular mobility is found, when taking the angle $\theta_{\vec{k}}$. The inset shows the (total) perpendicular mobilities $\mu(\theta_{\vec{v}_k})$ and $\mu(\theta_{\vec{k}})$ as a function of Fermi energy.*

In section 5.3 the mobility as a function of Fermi energy has been analyzed. Special features in the mobility curves are attributed to the existence of a periodic lateral potential modulation. One characteristic, which is experimentally easy to determine, is the anisotropy of the mobilities, i.e. $r_{mob} = \mu_{\parallel}/\mu_{\perp}$ as a function of charge density at low temperature. However, it shall be again emphasized that the reason for the mobility anisotropy is not necessarily due to a periodic lateral potential modulation [Bloch 94]. In order to understand the origin of the anisotropy and especially in order to explain the from experimental data deduced parallel and perpendicular mobility behaviors, numerical calculations are necessary.

In order to demonstrate the existence of minigaps by measuring the parallel and perpendicular mobility as a function of charge density at low temperature, the (parallel and perpendicular) longitudinal and Hall resistance of

sample L206.2 is measured at $T = 4.2\text{K}$. A gate was deposited (after having done the measurements, presented in section 6.2.1) on this sample, which allows to change the charge density at low temperature. The experimental data are shown in Fig. 6.13 (points). The parallel Hall mobility exhibits two different slopes. For $N_s < 3 \cdot 10^{11} \text{ cm}^{-2}$, the mobility increases faster as a function of charge density than for $N_s > 3 \cdot 10^{11} \text{ cm}^{-2}$. The perpendicular Hall mobility can even be divided into three different "regimes": At low charge density ($N_s < 2.5 \cdot 10^{11} \text{ cm}^{-2}$), the mobility increases gently with increasing charge density. At $N_s = 2.5 \cdot 10^{11} \text{ cm}^{-2}$, the mobility changes its slope and increases faster with increasing charge density up to $N_s \sim 4.5 \cdot 10^{11} \text{ cm}^{-2}$. For $N_s > 4.5 \cdot 10^{11} \text{ cm}^{-2}$, one remarks a saturation in the mobility curve. However, no typical "w"-structure is seen as it was seen by T. Evelbauer in metal - oxide - semiconductor structures prepared on high index surfaces of p-InSb at $T = 4.2\text{K}$ [Evelbauer 86]. This might be due to the relatively high temperature. For instance, Cole et al. [Cole 77] observed the "w"-structure in inversion layers on (119)Si at $T = 1.7\text{K}$, whereas no sign of the "w"-structure was seen at $T = 4.2\text{K}$. Moreover, in Fig. 6.13, the perpendicular Hall mobility does not exhibit a pronounced maximum, when the Fermi level is close to the second minigap. At first glance a rather disappointing result! However, at a second glance, the experiment is quite important since it seems to give a hint for the choice of angle which has to be chosen in the numerical calculations.

At this point, it shall be reminded that the most remarkable effect between taking the scattering angle $\theta_{\vec{v}_k}$ and taking the scattering angle $\theta_{\vec{k}}$ when solving the linearized Boltzmann transport equation (section 5.4.3) is seen, when the Fermi energy is in the second miniband: taking the scattering angle $\theta_{\vec{v}_k}$, a pronounced maximum is seen, whereas it is less accentuated, when taking the angle $\theta_{\vec{k}}$ (see Fig. 5.16 and inset of Fig. 6.13). Mathematically, the question which scattering angle has to be taken when solving the linearized Boltzmann transport equation for a modulated 2DEG has not been resolved yet [Ziman 61].

Performing the calculations in order to understand the experimental data, while assuming the **same** strength of lateral potential modulation with respect to the temperature dependent calculations, once taking the angle $\theta_{\vec{v}_k}$ and once taking the angle $\theta_{\vec{k}}$, one obtains the following curves, shown in Fig. 6.13. The calculations are performed assuming a temperature of $T = 4.2\text{K}$. Since one changes the charge density by the application of a gate voltage V_g between the gate and the 2DEG, it is assumed, that the number of remote ionized donors remains constant, $N_D^+ = N_s(V_g = 0\text{mV}) = 4.5 \cdot 10^{11} \text{ cm}^{-2}$.

This is a different assumption with respect to the measurements as a function of temperature. As a consequence, the alloy scattering becomes more important at higher charge density (at $N_s = 6 \cdot 10^{11} \text{ cm}^{-2}$, the contribution of alloy scattering to the total resistance is 40% with respect to 60% of remote ionized impurity scattering ($T = 4.2\text{K}$).

Taking the angle $\theta_{\vec{k}}$, one finds in the perpendicular direction a good agreement between the experimental data and numerical calculations. The experimental data are especially (also quantitatively!) well reproduced, when the Fermi energy is in the second miniband. In contrast, taking the angle $\theta_{\vec{v}_{\vec{k}}}$ (dashed line) leads to an overestimation of the perpendicular mobility when the Fermi energy is in the second miniband, e.g. the characteristic maximum of the second miniband is not seen experimentally. This might indicate that the angle $\theta_{\vec{k}}$ should be considered as scattering angle when solving the linearized Boltzmann transport equation.

Regarding the parallel direction, one does not find such good quantitative agreement. The numerical calculations have been shifted in mobility ($+2 \cdot 10^4 \text{ cm}^2 \text{ V}^{-1} \text{ s}^{-1}$) and in charge density ($+0.5 \cdot 10^{11} \text{ cm}^{-2}$). This might be due to the fact that one has not yet found the optimal estimation of the lateral potential modulation. This experiment demonstrates again, independently of the question of scattering angle, the existence of the first and second minigap. Only with the help of the lateral potential modulation, the parallel and perpendicular mobility behavior as a function of charge density can be understood.

As a conclusion, in this chapter it was shown by the interplay of experimental and theoretical results:

- The importance of including three subbands in the dielectric function when trying to understand both the mobility of a modulated and unmodulated 2DEG at higher charge density or at higher temperature.
- The existence of minigaps in the bandstructure of a modulated 2DEG, manifesting themselves in both temperature dependent and charge density dependent mobility measurements.
- The importance of taking the second Fourier coefficient of the lateral potential modulation into account, i.e. the modulation potential cannot be considered in a sinusoidal approximation.
- The scattering angle $\theta_{\vec{k}}$ seems to be the more reliable approach (in comparison to $\theta_{\vec{v}_{\vec{k}}}$) for the scattering angle in the linearized Boltzmann transport equation for a modulated 2DEG.

Chapter 7

Conclusion

Lateral AlAs/GaAs superlattices on vicinal surfaces are grown and their electronic properties are investigated by transport measurements. Numerical calculations are developed to understand the experimental measurements comprehensively. For the first time, the existence of minigaps and minibands in these kind of structures are convincingly demonstrated by temperature and charge density dependent resistivity measurements.

Organized molecular beam epitaxy on vicinal surfaces allows to create two - dimensional electron systems, which are periodically modulated on a nanometric scale in one direction. Due to the periodical lateral potential modulation, which is generated by the alternate deposition of Al and Ga atoms (under low Arsenic background pressure) on vicinal surfaces, minigaps and minibands arise in one direction of the bandstructure of the lateral modulated electron system.

The minigaps and -bands are demonstrated by temperature dependent mobility measurements. For this purpose, the anisotropy ratio of the mobility $r(T) = \mu_{||}/\mu_{\perp}$ is measured for different charge densities. Depending on the charge density, they exhibit pronounced maxima at finite temperature which arise from an anomaly in the mobility perpendicular to the lateral potential modulation.

This is shown by calculating the bandstructure in a self - consistent Hartree approximation. The resulting wave functions are used to solve the semiclassical linearized Boltzmann transport equation in a relaxation time approximation, considering ionized impurity, alloy and acoustic phonon scattering. Equally, the strong anisotropy of the collision time due to the anisotropy of the band structure is taken into account. The impact of the second Fourier coefficient of the lateral potential modulation as well as the

effect of including higher subbands (up to three) in the dielectric function is studied systematically for a small angle scattering (remote ionized impurity) and a large angle scattering (alloy) potential. Due to this detailed analysis, it is possible to obtain a thorough explanation of the experimental data, and especially to understand the anomaly in the perpendicular direction which arises, if the Fermi energy is close to the second miniband:

- At low temperatures ($T < 30\text{K}$), the perpendicular resistance increases much faster than in the parallel direction. This initial increase as a function of temperature is due to the second Fourier coefficient of the lateral potential modulation. It does not only cause the opening of a second minigap of similar size to the first one, it also couples states, uncoupled before, enhancing thus the scattering probability. Hereby the umklapp processes proved to be of special importance for the perpendicular direction.
- The perpendicular resistivity decreases at higher temperature. This is due to enhanced screening at higher temperature. Numerically, it has to be taken into account by including higher subbands in the dielectric function.

Measuring the perpendicular and parallel mobility as a function of charge density at low temperature, seems to indicate the answer to the theoretical open question, which scattering angle ($\theta_{\vec{v}_k}$ or $\theta_{\vec{k}}$) has to be taken when solving the linearized Boltzmann transport equation for a modulated electron system in a relaxation time approximation: taking the angle $\theta_{\vec{k}}$, one finds better agreement between the experimental data and the calculations than when taking $\theta_{\vec{v}_k}$.

The importance of including higher subbands in the dielectric function at higher temperature or charge density is equally demonstrated for an unmodulated 2DEG. It is pointed out that the inclusion of higher subbands is more important if the average scattering vector is small, e.g. the effect is more pronounced for remote ionized impurity scattering than for alloy scattering.

In spite of these achievements, modulated two dimensional electron systems are just in the beginning of being systematically studied by transport measurements. There are still many exciting experiments to do:

It would be very interesting to perform capacity voltage measurements, because the capacity of a 2DEG is directly proportional to the density of states of the system. Since the density of states becomes one dimensional as soon as the Fermi energy enters a minigap, the minigaps should be equally

easy to observe. Up to now far - infrared measurements in lateral superlattices fabricated by the growth on vicinal surfaces did not show evidence of the existence of minigaps. It would be worth to try these measurements again with the samples studied in this work. Due to the here presented results, the experimental data should be easier to analyze. Additionally, one is now capable to adjust the position of the Fermi level, which was not possible in former experiments.

It would be also desirable to be capable to create stronger lateral potential modulations. Lateral superlattices based on InAs/GaAs seem to be promising. However, additional difficulties in the growth will arise due to the lattice constant mismatch of InAs and GaAs (7 %).

From a more theoretical point of view, it is interesting to compare the experimental results and theoretical analysis presented in this work with the recently performed experiments in quasi 1D organic conductors [Moser 98]. One finds in these structures similar anomalous behavior (as discussed in this work) on the c - axis conductivity at temperatures above 100 K, which was interpreted as Luttinger Liquid phase. Although the anomaly is much stronger in these systems and shifted in temperature, it is worth to question, under which conditions one could expect a precursor of Luttinger liquid in the structures studied in this work.

Bibliography

- [Albrecht 99] C. Albrecht, J. H. Smet, D. Weiss, K. von Klitzing, R. Henning, M. Langenbuch, M. Suhrke, U. Rössler, V. Umansky, and H. Schweizer, Phys. Rev. Lett **83** 2234 (1999).
- [Ando 76] T. Ando, Phys. Rev. B **13** 3468 (1976).
- [Ando 79] T. Ando, J. Phys. Soc. Japan **47**, 1595 (1979).
- [Ando 82] T. Ando, Rev. Mod. Physics **54**, 463 (1982).
- [Ando 82] T. Ando, A.B. Fowler, and F. Stern, Rev. Mod. Phys. **54**, 468 (1982).
- [Ando 82] T. Ando, J. Phys. Soc. Japan **51**, 3893 (1982).
- [Andrei 88] E.Y. Andrei, G. Deville, D.C. Glatthli, F.I.B. Williams, E. Paris and B. Etienne, Phys. Rev. Lett. **60**, 2765 (1988).
- [Ashcroft 76] see e.g. N.W. Ashcroft and N.D. Mermin, *Solid State Physics*, Holt - Saunders International Edition (1976).
- [Bar - Joseph 89] I. Bar - Joseph, K.W. Goossen, J.N. Kuo, R.F. Kopf, D.A.B. Miller and D.S. Chemla, Appl. Phys. Lett. **55**, 340 (1989).
- [Bastard 88] G. Bastard, *Wave Mechanics Applied to Semiconductor Heterostructures*, Les Editions de Physique, Les Ulis, France, p. 63, 1988.
- [Bloch 94] J. Bloch, U. Bockelmann and F. Laruelle, Europhys. Lett. **28**, 501 (1994).
- [Brum 85] J.A. Brum and G. Bastard, Solid St. Commun. **53**, 727 (1985).

- [Calecki 69] see e.g. D. Calecki and J. Tavernier, *Reflection High - Energy Electron Diffraction and Reflection Electron Imaging of Surfaces*, NATO ASI Series, Vol. **188**, 541 pages (Plenum Press) (1987).
- [Capasso 87] F. Capasso, *Semiconductors and Semimetals*, Vol. **24** Academic, New York, 319 (1987).
- [Chalmers 89] S.A. Chalmers, A.C. Gossard, P.M. Petroff, J.M. Gaines, and H. Kromer, J. Vac. Sci. Technol. **B7** 1357 (1989).
- [Cole 77] T. Cole, A.A. Lakhani, and P.J. Stiles, Phys. Rev. Lett. **28**, 722 (1977).
- [Danan 87] G.Danan, B.Etienne, F. Molloy, R. Planel, A.M. Jean - Louis, F. Alexandre, B. Jusserand, G. Le Roux, J.Y. Marzin, H. Savary, and B. Sermage, Phys. Rev. B **35**, 6207 (1987).
- [Delagebeaudeuf 80] D. Delagebeaudeuf, P. Delescluse, P. Etienne, M. Laviro, J. Chaplar and N. T. Linh, Electron Lett. **16**, 667, (1980).
- [Dingle 78] R. Dingle, H.L. Störmer, A.C. Gossard and W. Wiegmann, Appl. Phys. Lett. **33**, 665 (1978).
- [Elleuch 99] S. Elleuch, *Transport électronique en regime de mobilité: application aux systèmes bidimensionnels contraints InAlAs/InAlAs* Dissertation Paris (1996).
- [Esaki 70] L. Esaki and R. Tsu, IBM J. Res. and Dev. **14**, 61 (1970).
- [Etienne 95] B. Etienne, F. Laruelle, J. Bloch, L. Sfaxi, and F. Lelarge, J. Cryst. Growth **150**, 336 (1995).
- [Etienne 96.1] B. Etienne, F. Laruelle, Z. Wang, L. Sfaxi, F. Lelarge, F. Petit, T. Mélin, and A. Cavanna, Semicond. Sci. Technol. **11**, 1534 (1996).
- [Etienne 96.2] B. Etienne, F. Laruelle, and Z. Wang, Semicond. Sci. Technol. **11**, 1 (1996).
- [Evelbauer 86] T. Evelbauer, A. Wixforth, and J.P. Kotthaus, Z. Phys. B **64**, 69 (1986).
- [Fowler 66] A.B. Fowler, F.F.Fang, W.E. Howard, and P.J. Stiles, J. Phys. Soc. Jpn. **21**, 333 (1966).

- [Gaines 88] J. M. Gaines, P.M. Petroff, H. Kroemer, R.J. Simes, R.S. Geels, and J.H. English, J. Vac. Sci. Technol. **B6**, 1378 (1988).
- [Hai 95] G.-Q. Hai and N. Studart, Phys. Rev. B **52**, 8363 (1995).
- [Heiblum 82] M. Heiblum, M.I. Nathan, and C.A. Chang, Solid State Electronics Vol. **25**, 185 - 195 (1982).
- [Henzler 74] M. Henzler and J. Clabes, Jpn. J. Appl. Phys., Suppl. 2, Pt. 2, 389 (1974).
- [Hirakawa 86] K. Hirakawa and H. Sakaki, Physical Review. B **33**, 8291 (1986).
- [Horikoshi 86] V. Horikoshi, M. Kawashima, H. Yamaguchi, Jpn. J. Appl. Phys. **25**, L 868 (1986).
- [Kapon 89] E. Kapon, D.M. Hwang and R. Bhat, Phys. Rev. Lett. **63**, 430 (1989).
- [Kim 96] D.S.Kim and H.S. Ko, Phys. Rev. B **54**, 14580 (1996).
- [Klitzing 80] K. v. Klitzing, G. Dorda, and M. Pepper, Phys. Rev. Lett. **45** 494 (1980).
- [Krishnamurthy 94] M. Krishnamurthy, A. Lorke, and P. Petroff, Surf. Sci. Lett. **304**, L493 (1994).
- [Larsen 87] see e.g. P.K. Larsen and P.J. Dobson eds., *Introduction aux phénomènes de transport lineaires dans les semiconducteurs*, Masson Paris (1969).
- [Laruelle 97] F. Laruelle, F. Lelarge, Z.Z. Wang, T. Mélin, A. Cavanna, and B. Etienne, Journ. of Cryst. Growth **175/176**, 1087 (1997).
- [Laruelle 99] F. Laruelle, A. Cavanna, F. Lelarge, Z.Z. Wang, and B. Etienne, Journ. of Cryst. Growth **201/202**, 819 (1999).
- [Lee 97] S. - C. Lee and I. Galbraith, Phys. Rev. B **55**, R16025 (1997).
- [Lelarge 96] F. Lelarge, *Croissance par épitaxie par jets moléculaires et études structurales de structures semiconductrices de basse dimensionnalité*, Dissertation Paris VI (1996).

- [Lelarge 97] F. Lelarge, F. Laruelle, and B. Etienne,
Europhys. Lett. **40**, 213 (1997).
- [Maldague 78] P.F. Maldague, Surf. Sci. **73**, 296 (1978).
- [Matheson 82] T. G. Matheson and R. J. Higgins,
Phys. Rev. B **25**, 2633 (1982).
- [Mélin 96] T. Mélin and F. Laruelle, Phys. Rev. Lett. **76**, 4219 (1996).
- [Mélin 98] T. Mélin, *Spectroscopie optique de réseau de fils quantiques GaAs/AlAs épitaxiés sur surfaces vicinals: confinement quantique et interaction coulombienne entre 2D et 1D*, Dissertation, Ecole Polytechnique (1998).
- [Menne 98] R. Menne and R.R. Gerhardt, Phys. Rev. B **57**, 1707 (1998).
- [Messiah 59] see e.g. A. Messiah, *Mécanique Quantique*, Dunod paris (1959).
- [Miller 85] D. A. B. Miller, D.S. Chemla, T.C. Damen, a.C. Gossard, W.Wiegmann, T.H. Wood, and C.A. Burrus, Phys. Rev. B **32**, 1043 (1985).
- [Miller 91] M.S. Miller, C.E. Pryor, H. Weman, L.A. Samoska, H. Kroemer, and P.M. Petroff, J. of Cryst. Growth **111**, 323 (1991).
- [Miller 92] M.S. Miller, H. Weman, C.E. Pryor, M. Krishnamurthy, P.M. Petroff, H. Kroemer, and J.L. Merz, Phys. Rev. Lett **68**, 3464 (1992).
- [Mori 80] S. Mori and T. Ando, J. Phys. Soc. Japan **48**, 865 (1980).
- [Moser 98] J. Moser, M. Gabay, P. Auban - Senzier, D. Jérôme, K. Bechgaard, and J. M. Fabre, Eur. Phys. J. B **1**, 39 (1998).
- [Motohisa 89] J. Motohisa, M. Tanaka, and H. Sakaki, Appl. Phys. Lett. **55**, 1214, (1989).
- [Nelson 74] A. R. Nelson and E. Brown, Phys. Rev. B **9**, 1664, (1974).
- [Pardo 00] F. Pardo and J. L. Pelouard, to be published.
- [Perez 90] F. Perez, B. Jussierand, C. Dahl, M. Filoche, L. Ferlazzo - Manin, and B. Etienne, Phys. Rev. B **54**, 11098 (1990).

- [Petroff 84] P.M. Petroff, A.C. Gossard, and W. Wiegmann,
Appl. Phys. Lett. **45**, 620 (1984).
- [Pfeiffer 90] L. Pfeiffer, K. W. West, H.L. Stormer, J.P. Eisenstein, K. W.
Baldwin, D. Gershoni, and J. Spector, Appl. Phys. Lett. **56**, 967 (1990).
- [Ploog 87] K. Ploog, J. Cryst. Growth **81**, 304 (1987).
- [Pukite 84] P. R. Pukite, J. M. Van Hove, and P. I. Cohen,
Appl. Phys. Lett. **44**, 456 (1984).
- [Sakaki 76] H. Sakaki, K. Wagatsuma, J. Hamasaki, and S. Saito,
Thin Solid Films **36**, 497 (1976).
- [Sakaki 80] H. Sakaki, Jpn. J. Appl. Phys. **19**, L735 (1980).
- [Sakaki 89] H. Sakaki, Jpn. J. Appl. Phys. **28**, L314 (1989).
- [Schulenburg 95] M. Schulenburg, *Nanotechnologie - Die letzte industrielle
Revolution*, Insel Verlag, (1995).
- [Sibille 90] A. Sibille, J. F. Palmier, H. Wand and F. Mollot,
Phys. Rev. Lett. **64**, 52 (1990).
- [Siggia 70] E.D. Siggia and P.C. Kwok, Phys. Rev. B **2**, 1024 (1970).
- [Sham 78] L.J. Sham, S. J. Allen, Jr., A. Kamgar, and D.C. Tsui,
Phys. Rev. Lett. **40**, 472 (1978).
- [Stern 67] F. Stern, Phys. Rev. Lett. **21**, 1687 (1967).
- [Stern 78] F. Stern, Surf. Sci. **73**, 197 (1978).
- [Störmer 82] H.L. Störmer, A.C. Gossard, and W. Wiegmann, Solid St. Com-
mun. **41**, 707 (1982).
- [Sotirelis 93] P. Sotirelis and P. von Allmen, Phys. Rev. B **47**, 12744 (1993).
- [Szmulowics 86] F. Szmulowics, Physical Review. B **34**, 4031-4047 (1986).
- [Tang 89] D.S. Tang, Phys. Rev. B **37**, 8319 (1989).
- [Tsang 82] W.T. Tsang, Appl. Phys. Lett **40**, 217 (1982).

- [Tsui 82] D.C. Tsui, H.L. Störmer and A.C. Gossard,
Phys. Rev. Lett. **48**, 1559 (1982).
- [Vinter 83] B. Vinter, Solid State Communic. **48**, 151 (1983).
- [Voisin 88] P. Voisin, J. Vleuse, C. Bouche, S. Gaillard, C. Alibert, and A.
Regreny, Phys. Rev. Lett. **61**, 1639 (1988).
- [Gerhardts 89] R.R. Gerhardts, D. Weiss, and K. Klitzing,
Phys. Rev. Lett. **62**, 1173 (1989).
- [Weiss 89] D. Weiss, K. v. Klitzing, K. Ploog and G. Weimann,
Europhys. Lett **8**, 179 (1989).
- [Winkler 89] R. W. Winkler and J. P. Kotthaus,
Phys. Rev. Lett. **62**, 1177 (1989).
- [Wood 80] C.E.C. Wood, G. Metze, J. Berry, and L.F. Eastman,
J. App. Phys. **51**, 383 (1980).
- [Yamaguchi 89] H. Yamaguchi and Y. Horikoshi,
Jpn. J. Appl. Phys. **28**, L 1456 (1989).
- [Ziman 61] J. M. Ziman, Phys. Rev. **121**, 1320 (1961).

Every time you go ...

you leave a little piece of you ...

Thanks a lot to ...

- Dr. Bernard Etienne and Dr. François Laruelle. I learnt a lot from them during the three years.
- Dr. Jean - Luc Pelouard - thanks for all.
- Prof. Dr. Jörg - Peter Kotthaus for having accepted to be my "Doktorvater" (although I was not in his lab!) and for all his support during the three years.
- Dr. Jean - Yves Marzin for his interest in the progress of my Ph. D..
- Antonella Cavanna - without her many days would have been harder.
- Thierry Mélin, Pascale Senellart, Bruno Gayral, Cecile Naud, Florent Petit, Sylvain Demichel, Alexandre Nedelcu and to all the Ph. D. students which contributed to the joy of my stay in the lab.
- Dr. Gian Carlo Faini, Dr. Fabrice Pardo, Dr. Dominique Mailly, Dr. Jacqueline Bloch and Dr. Véronique Thierry - Mieg - for all your helpfulness and for some smile and words, which were encouraging.
- Christophe Dupuis (and all the other members of the clean - room), Yvon Lagadec, Edmond Cambril, Laurent Merzeau and Gilbert Chanconie - whenever I was in a hurry, they were willing to help me (and not only then!). They worked fast and nevertheless precise. Thanks for all your cooperation.
- all the persons who contribute to the good atmosphere - so that one likes to come daily in the lab, even if things do not work like one wishes ...
- my family and Mark.

Curriculum Vitae:

Petra Denk, born April 4th, 1972 at Düsseldorf

1978 - 1982	Volksschule München / Steinfurt
1982 - 1991	Gymnasium, Steinfurt
08/1988 - 08/1989	Fort P. Central High School, Florida, U.S.A.
11/1991 - 12/1996	Diploma studies in Physics, Ludwig - Maximilians - University Munich
09/1995 - 06/1996	Diploma Thesis "Tunneling experiments with parabolic quantum wells" in the group of Prof. J. Kotthaus, supervisor: Priv. - Doz. A. Wixforth
since 03/1997	Ph. D. Thesis Joint supervision of Prof. J. Kotthaus Dr. B. Etienne (Paris), and Dr. J. - L. Pelouard (Paris)